Investigations of Host-Guest Systems Based on Mesoporous Materials

by

Haiquan Guo

A dissertation submitted to the Graduate Faculty in Chemistry in partial fulfillment of the requirements for the degree of Doctor of Philosophy, The City University of New York

2004

INFORMATION TO USERS

The quality of this reproduction is dependent upon the quality of the copy submitted. Broken or indistinct print, colored or poor quality illustrations and photographs, print bleed-through, substandard margins, and improper alignment can adversely affect reproduction.

In the unlikely event that the author did not send a complete manuscript and there are missing pages, these will be noted. Also, if unauthorized copyright material had to be removed, a note will indicate the deletion.

ProQuest Information and Learning Company
300 North Zeeb Road
P.O. Box 1346
Ann Arbor, MI 48106-1346

This manuscript has been read and accepted for the graduate faculty in Chemistry in satisfaction of the dissertation requirement for the degree of Doctor of Philosophy.

April 22, 2004 — Daniel L. Akins
Date — Chair of Examining Committee

4-29-04 — Gerald Koppel
Date — Executive Officer

Supervisory committee

THE CITY UNIVERSITY OF NEW YORK

Abstract

Investigations of Host-Guest Systems Based on Mesoporous Materials

By

Haiquan Guo

Adviser: Professor Daniel L. Akins

The work presented here is a compilation of different molecules encapsulated within ordered mesoporous materials, especially MCM-41. Due to their ordered pore structures and highly specific surface areas, mesoporous materials have been regarded as "molecule factories" to manufacture aligned, well-dispersed molecules within their pore structures. The objective of this dissertation is to introduce guest molecules (organic and inorganic compounds) to the pore channels of the mesoporous material for the purpose of creating new nanocomposites with unique properties or properties of the guest molecules that are improvement of these of the isolated component.

For these reasons, several molecules were successfully encapsulated as the guests, such as aggregate dyes, a laser dye molecule with twisted intramolecular charge transfer (TICT) property, and magnetic nanoparticles. Upon encapsulation, many properties of these compounds are found to be modified as a result of confinement within the mesoporous materials.

In particular, we formed the J-aggregated Tetrakis (p-sulfonatophenyl) porphyrin (TSPP) and 1,1', 3,3'-tetraethyl-5, 5', 6,6'-tetrachloro-benzimidazolo-carbocyanine

(TTBC) within aluminosilicate mesostructures. The composite structures represent new "ship-in-a-bottle" type nanomaterials whose properties derive from energy states and dynamics that result from quantum confinement. This quantum confinement is associated both with the restricted growth region available to the spontaneously self-assembled molecular aggregates as well as the inherent confinement of the exciton's movement among a subset of coherently responding molecules within the physical aggregate.

We also have been able to observe dual emission from DCM, a laser dye, by encapsulation of dye molecules within an alumino-MCM-41. The interaction between DCM and the internal surface of MCM–41 was found to modify the optical properties of the confined DCM molecules. The dynamics of DCM in MCM-41 was found to correspond to a biexponential relaxation with one component of 0.6 ns (57%) and a very long component of 1.9 ns (43%).

Lastly, we report the development of a new functional nanocomposite material, MCM-41 loaded at a high level with Fe_2O_3, whose functionality involves an enhanced absorption of microwave energy, even in the absence of an applied magnetic field. Different factors, such as Fe_2O_3 loading level and the opening size of the mesopourous materials, have significant influence on the microwave absorption ability.

Preface

Since the discovery of the M41S family of mesoporous materials in 1992, we have witnessed the rapid development of nanocomposite materials from ordered mesoporous materials. Mesoporous materials have a uniform pore diameter and a hexagonal pore structure, which make them ideally suited as templates for preparing various nanostructures. As described in the literature involving an occluded species, the mesoporous material MCM-41 is exploited as a host to organize guest atoms, dyes, polymers and organic and inorganic compounds, with the aims of creating composite materials with catalytic, environmentally remunerative, and optoelectronic properties.

In this dissertation, three kinds of guests: aggregated dyes, a laser dye with TICT property and metal oxide have been studied. Different function agents have been used to modify the surface of MCM-41 in order to successfully incorporate the guests.

In Chapters 2 and 3, we report on the encapsulation of two aggregated dyes — tetrakis (p-sulfonatophenyl) porphyrin (TSPP) and 1,1', 3,3'-tetraethyl-5, 5', 6,6'-tetrachlorobenzimidazolocarbocyanine (TTBC) — within an aluminumsilicate mesostructure under different pH conditions in order to constrain orientation and aggregate length. UV-vis, XRD and fluorescence measurements were used as spectroscopic tools to characterize the aggregated composites. The composite structures represent new "ship-in-a-bottle-type" nanomaterials whose properties

derive from exciton energies and dynamics that result from quantum confinement within the mesoporous materials.

To stabilize the synthesized MCM-41 and allow formation of composites, we found it necessary to modify the interior structure of the mesoporous silica using a silylation reagent, aminopropyl triethoxysilane (APTES) to satisfy guest-host intermolecular or electrostatic interactions and to link oxygens at the interface, thus rigidifying the MCM-41 structure.

In Chapter 4, the laser dye 4-(dicyanomethylene)-2-methyl-6-(p-dimethylaminostyryl)-4H-pyan (DCM) was introduced into MCM-41. DCM is a laser dye with a high fluorescence efficiency and stable photochemistry. In its first electronically excited state, an electron is transferred intramolecularly from the donor to the acceptor group, through a process known as intramolecular charge transfer (ICT). In addition to the ICT process, DCM can also undergo a twist about the ethylenic double bond or about the bond joining the dimethylamino group and the aromatic ring, resulting in a twisted intramolecular charge-transfer (TICT) state. The photo-induced charge separation is maximized when the donor and acceptor groups are mutually perpendicular to minimize the electronic coupling between the two groups. Until our study, no dual emission was observed in any pure solvent, as a result of ultra fast charge transfer. In recent years, the optical properties of DCM in many organized assemblies such as protein, DNA, cyclodextrin, microemulsions, micelles, lipid vesicles, sol-gel matrix and polymer cavities were studied mainly because the media slowed the TICT process, and no dual emission was observed. We, to our knowledge, are the first to report the dual emission of DCM

encapsulated within AlMCM-41. We found that DCM in AlMCM-41 displays biexponential relaxation with one component of 0.6±0.1 ns (57%) and a slower one of 1.9±0.1 ns (43%).

In Chapter 5, nanostructural ferric oxide was synthesized within three one-dimensional (1-D) silicate mesoporous molecular materials with different pore sizes, resulting in the formation of nanocomposites. These resulting nanocomposites were characterized by UV-vis, Infrared spectroscopy (IR), Transmission electron microscopy (TEM), Electron paramagnetic resonance (EPR) and X-ray diffraction. The occluded Fe_2O_3 nanostructures were found to evince optical spectra and magnetic properties that were significantly different from those of bulk Fe_2O_3. As expected, the UV-vis absorption spectra of the nanocomposites were blue-shifted relative to that of bulk Fe_2O_3, and the shifts vary monotonically with respect to the load level of Fe_2O_3 and the pore dimensions of the mesoporous materials.

Furthermore, EPR measurements indicate that the various nanocomposites (whose dimensions were controllable by the pore sizes of the silicate materials), when sufficiently loaded with Fe_2O_3, possess nonzero absorptions at zero applied magnetic field, as well as significant microwave absorption capacities as a function of applied magnetic field strength. This material may be useful in microwave devices for home-use, automotive and radar systems. UV-vis, XRD, IR, EPR and TEM are the tools that were use to characterize the properties of the composites.

Acknowledgments

First, I wish to express sincere appreciation to my mentor, Professor Daniel L. Akins. He provided me with inspiration, advice, guidance and encouragement in course of the research. He is a professor strict in research but considerate in living. Professor Akins provided me many opportunities and encouraged me to do what I really like. He is also a quite understanding professor. Since my daughter arrived in my life, Prof. Akins continued to believe in me and he gave me freedom to be mother and continue with my research. I was often pleasantly surprised when I sent him files in the late night, he responded to me quickly. It is really fortune for me to choose him as my mentor. From him, I know a person should have his own objective and should be persistent to fulfill it.

I would like to extend my gratefulness to my committee members, Professor George Flynn, Professor Maria C. Tamargo, and Professor Nan-loh Yang. They gave me a bundle of valuable suggestions during my pursuit of my Ph. D. I am grateful to them for their insights, knowledge, and experience. From them, I realize that to be a scientist, you have to be creative, diligent and honest.

I want to thank Hanru Zhu, who helped me greatly with use of the instrument operation. I also thank Sandra Smith, the administrative assistant of Center for Analysis of Structures and Interfaces (CASI), for her assistance in my study and campus life. Also, Dr. Guo helped me in my first year to become familiar with the lab and taught me many spectroscopy theories. From Dr. Wei Xu, an unselfish co-worker and intelligent chemist, I learned the area of MCM-41. Dr Brown picked

me up when I first arrived in America and helped me settle down. From him, I learned we should always care for other people.

Many thanks go to all my labmates, Dr. Hui Yang, Dr. Metin Adyin, Yanting Liao, Nathan Stevens, Fleumingue Jean-Mary, Philippe Mercier, Shiunchin C. Wang and Dionne Miller. We had a lot of fun together. And I now know how to cooperate with other people.

Finally, I want to thank my family: my dear husband, Xiaoming Zhang, for always standing beside me. He constantly discussed my research with me and found useful literature. We shared all of my happiness and sadness together. I thank my lovely daughter, Michelle Zhang for bringing me joy. I know tomorrow is always hopeful because of her presence in my life.

Table of Contents

List of Tables

List of Figures

Chapter 1: Introduction to Mesoporous Materials

The design and synthesis of porous materials is a current challenge in solid-state chemistry. For many applications, the precise control of pore dimensions is the limiting factor. A porous material of good quality should provide the following properties:

- A narrow pore size distribution,
- A readily tunable pore size in a wide range.

In addition, high chemical, thermal, hydrothermal and mechanical stabilities, as well as appropriate particle size, high surface area and pore volume are also required.

According to IUPAC nomenclature, porous solids are widely classified into three categories based on pore size of the materials: microporous (<2 nm), mesoporous (2-50 nm), and macroporous (>50 nm). At present time, applications for macroporous compound are relatively limited due to their low surface area and large non-uniform pores. In contrast, there has been a dramatic increasing research activity on the synthesis and characterization of both periodic and non-periodic mesoporous solids, for their size-specific applications in catalysis and separation. What followed is the introduction of each kind of mesoporous materials.

1.1 Zeolites Containing Mesoporous Materials[1-3]

Zeolites are the most famous crystalline microporous materials that are widely used in industry. Zeolites are naturally occurring or synthetic, highly crystalline aluminosilicates with the general chemical fomula $[M_{x/n}(AlO_2)]_x[SiO_2]_y \cdot mH_2O$. These materials show the following specific features: high surface area and controllable adsorption capacity, properties varied from hydrophobic to hydrophilic, resistance to heat, steam and chemical attacks. The strength and amount of active sites, such as acid sites generated in the framework as well as their strength and concentration can be tailored for a particular application. The sizes of the holes of the matrices are smaller than 10 Å, which is in the range typical for many molecules of interest. Electronic confinement attributed to the restricted space together with the strong electric fields existing in those micropores is responsible for a pre-activation of the reactants. The intricate channel structure makes the zeolites present various types of shape selectivity, so that a given catalytic reaction can be directed toward the desired product avoiding undesired side reactions.

Because of the properties above, zeolites are used successfully as catalysts in industries, such as oil refining, petrochemistry, and organic synthesis in the production of fine and speciality chemicals, especially for molecules with kinetic diameters smaller than 10 Å. However, despite their catalytically desirable properties, zeolites become inadequate if reactants with sizes lager than the diameters of the pores have to be processed. In this case, in order to overcome such a limitation, the rational approach would be to maintain the porous structure but to increase their diameter, so that the zeolites are brought into the mesoporous region

and also the benefits described above are kept. So numerous attempts were tried to create larger pore zeotype materials based on the fact that most of the organic templates used to synthesize zeolites affect the gel chemistry and act as void fillers in the growing of porous solids. However, the results were not as expected. Fig. 1-1 is the structure of zeolite Y. Formed by steam treating, mesopores of sizes in the range of 10-20 nm were found in the Y-zeolite, which would basically increase the external surface of the Y-zeolite, and so increase the accessibility of large molecules to the external opening of the pores. The mesopores could be characterized by different techniques including nitrogen adsorption, high-resolution electron microscopy, and analytical electron microscopy.

1.2 Silica Based M41S Molecular Sieves Materials[3-7]

In the early 1990s, Mobil scientists as well as Japanese researchers reported the first successful synthesis of a novel family of periodic mesostructured materials denoted as M41S. The synthesis of these porous composite materials was based on a new concept that a self-assembled molecular aggregate or supramolecular assembly of surfactant molecules such as cetyltrimethylammonium (CTA) cation rather than the conventional single- (amine-) molecule(templated for microporous (zeolites) structures as the agent to direct the one dimensional, hexagonal, and uniform pore opening structure. MCM-41 possesses highly regular arrays with diameters in the range of 15-100 Å depending on the templates used, the addition of auxiliary organic compounds, and the reaction parameters. This discovery of the mesoporous material M41S family has drawn interest in many areas of physical, chemical, and engineering sciences. In this family, MCM-41 and MCM-48 have

been identified as thermally stable. MCM-41 has a hexagonal structure with one-dimensional pore structure and MCM-48 displays a cubic structure with a three-dimensional pore system. MCM-41 is widely investigated because other family members are either thermally unstable or difficult to obtain. And it has a large BET surface area and pore volume, and an acidity and hydrophobic/hydrophilic property that can be varied by changing Si/Al ratios.

The X-ray diffraction (XRD) pattern of MCM-41 is shown in Fig. 1-2. The small angled XRD patterns of MCM-41 has no reflection over 6 degree (2θ). The main index peak (100) appears at around 2 degree (2θ), and the other index peaks (110) and (200) are at around 4-5 degree (2θ). By using the main index peak position, the pore size of MCM-41 can be calculated by the following equations:

$$d_{100}=0.154/2(\mathrm{Sin}\theta_{100}) \quad (1)$$

$$a=2(3^{-1/2})d_{100}-1 \text{ (nm)} \quad (2)$$

where d_{100} is the d-spacing at (100) index, a is the pore size of MCM-41 with unit nm.

The originally proposed mechanic pathways of the formation of the MCM-41 structure are illustrated in Fig. 1-3. First, the surfactant aggregates and forms rodlike micelle, followed by the migration and polymerization of silicate anions, then the presence of the liquid-crystal mesophase results in the formation of the MCM-41 structure. Secondly, as a result of the mutual interactions between the silicate anion and the surfactant cations in the solution, the liquid-crystal-like

structures self-assemble. In this process, the silicate species generated in the reaction mixture influence the ordering of the surfactant micelles to the desired liquid-crystal phase. Further, hexagonal, cubic, and lamellar structures form through tuning the silica concentration at constant surfactant concentration.

In a typical MCM-41 synthesis, an aqueous solution containing silica with various silica sources such as fumed silica, sodium silicate, or tetraethyl orthosilicate, is added to a clear alkaline aqueous solution of a micelle-forming surfactant (e.g., long-chain quaternary ammonium halides) under constant stirring. For instance, low-molecular-weight amphiphiles, e.g., $C_nH_{2n+1}(CH_3)_3N^+$ (n=8-22) or $C_nH_{2n+1}C_5H_5N^+$ (n = 12 or 16), which have a hydrophilic (water-soluble) headgroup and a hydrophobic (water-insoluble) tail group, were applied as structure-directing agents. The silica source is hydrolyzed and condensed to form multidentate, multicharged anions so that it can coordinate with the surfactant headgroups. The silica species and the surfactants assemble into a silica-surfactant phase, and form a gel mixture. It is crucial in the synthesis to control the pH value. Normally, it is adjusted in the range of pH 8-11 by using a mineral acid or base such as sodium hydroxide/tetramethylammonium hydroxide. Over an extended period of time, the silica condenses to form a siloxane framework. Alternatively, the gel is transferred into a Teflon-lined autoclave and then heated (under autogenous pressure) in an air oven at 373 K for 1-3 days. After crystallization, the final solid product is filtered from the mother liquid, washed with deionized water, and air-dried at room temperature or higher. This sample is designated as-synthesized uncalcined MCM-41. By calcination around 177-327K or being washed by organic solvents such as

methanol, the template in the channel of the as-synthesized uncalcined MCM-41 was removed for future functionalization or encapsulation purposes.

By covalently anchoring a number of functional groups to the channel walls, the internal surface reactivity of the mesoporous hosts can be modified. The attachment of ligands can also be used to induce the molecules inside the channel or even to form the bulky metal complexes. The scheme is illustrated in Fig. 1-4

No doubt, those mesoporous materials bring definitively new possibilities for preparing catalysts with uniform pores in the mesoporous region, which should allow the reaction of relatively large molecules present in crude oils and in the production of fine chemicals. The uniform pore structures of molecular sieves can act as solid solvents to control the particle size and topology. Various metals, metal oxides, semiconductor clusters and nanowires, organic and organometallic compounds have been studied by being encapsulated within MCM-41.

1.3 Mesoporous Material SBA-15[8-9]

However, the poor hydrothermal stability of the MCM-41-related materials has restricted their potential applications. Thus, titanosilicate mesoporous materials with better hydrothermal stability are highly desirable. Fortunately, in 1998, a remarkable advance in the synthesis of ordered mesoporous materials was made by Zhao et al.. By using triblock copolymer surfactants as a template, the ordered large-pore mesoporous silica (SBA-15) with different structures was formed under highly acidic conditions. This methodology was soon extended to the synthesis of ordered continuous mesoporous silica films, fibers, rods, membranes, spheres, and

monoliths. SBA-15 has thicker pore walls (3.1-6.4 nm) and a much larger pore size (in the range of 4.6-10.0 nm) than that of MCM-41, which may facilitate the diffusion of relative bulky molecules and the mobility of nanostructured metals. The XRD pattern of SBA-15 is shown in Fig. 1-5. Three diffraction peaks can be indexed as the (100), (110), (200) reflections, thus proving that the SBA-15 has hexagonal structure similar to MCM-41. Due to its advanced features: easy synthesis, adjustable pore size, hexagonally uniformed, thick pore wall, and remarkable hydrothermal stability, SBA-15 is currently the most outstanding member of the family of triblock copolymer-templated materials. Many applications of SBA-15 materials can be envisioned in the fields of catalysis, sorption, and advanced material design. SBA-15 solids have been used as matrices to template the formation of metal or semiconductor nanoparticles or nanowires and mesoporous carbon molecule sieves. SBA-15 materials functionalized by organosilanes were found to be useful in sequestrating and releasing protein, removing heavy metals in pollutant solutions, chiral heterogeneous catalysts and solid acids. After patterning with soft lithography, SBA-15 may be used as waveguides and mirrorless lasers. In this study, the formation of highly dispersed metal nanoparticles in functionalized mesoporous silica SBA-15 has been characterized.

1.4 Host-Guest Investigation

Interest in mesoporous materials as host-guest systems has risen dramatically over the past few years, such that this fascinating class of substances now play an important role not only in numerous disciplines, such as material sciences, such as

organic or supramolecular chemistry. The mesoporous template acts as a structure-directing agent favoring the connection of the decisive bond. As a guest, the metal ion or the molecule coordinates ligands bonded to the matrix or host itself, which is thereby brought into alignment of a specific product.

For the mesoporous media, the large cavities and uniform hexagonal structure make the mesoporous materials act as "nano-bottles" to encapsulate the molecules inside the porous structures. Several kinds of guest compounds have received much attention for formation of advanced composites, including metal and semiconductor nanoparticles and nanowires, oxide and sulfide clusters, metal complexes, Carbon 60, organic molecules and polymer. The mesoporous materials can act as a template to direct the growth of the guest within the channel to get either nanoparticles or nanowires, thus forming novel composites with unique properties. The morphology of the guest species can be controlled by tuning the pore opening size of the host mesoporous silica as well as the guest loaded amount. The restricted space of the cavity and the interaction between the guests and host modify the properties of the molecule, which is significantly different from that of the bulk sample. The novel properties of the composites may promote applications in catalyst, separation, optical device and so on.

Many methods have been used to include the molecules: wet impregnate method, ion exchange, and using covalent grafting and functional groups. Mesoporous materials present hydroxyl-covered surfaces, which are reactive to the silane coupling agents that can tailor the surface properties for further attachment. By covalently anchoring functional groups APTES or AEPTES to the channel wall,

the surfaces of mesoporous materials are modified. The headgroup of the functional agents can be varied as either negative or positive charge by adjusting the pH for different encapsulation purpose. In this dissertation, three dyes and Fe_2O_3 were encaged inside mesoporous materials, especially MCM-41. It was discovered that the interaction of MCM-41 and those molecules modify the optical and spectral properties of the composite, which may be utilized in designing optical devices, molecular switches or microwave absorbing materials.

1.5 Bibliography

1. Cundy, C. S.; Cox, P. A. *Chem. Rev.; (Review)* **2003,** *103*; 663.
2. Kaduk, J. A.; Faber, J. *The Rigaku Journal* **1995**, *12*, 14.
3. Crorma, A. *Chem. Rev.* **1997,** *97*, 2373.
4. Selvam, P.; Bhatia, S. K.; Sonwane, C. G. *Ind. Eng. Chem. Res.* **2001**, *40*, 3237.
5. Scott, B. J.; Wirnsberger, G.; Stucky, G. D. *Chem. Mater.* **2001**, *13*, 3140.
6. Zhao, X. S.; Lu, G. Q.; Millar, G. J. *Ind. Eng. Chem. Res.* **1996**, *35*, 2075.
7. Moller, K.; Bein, T. *Chem. Mater.* **1998**, *10*, 2950.
8. Zhang, W. H.; Lu, J. Q.; Han, B.; Li, M. J.; Xiu, J. H.; Ying, P. L.; Li, C. *Chem. Mater.* **2002**, *14*, 3413.
9. Zhao, D.; Feng, J.; Huo, Q.; Melosh, N.; Fredrichson, G. H.; Chmelka, B. F.; Stucky, G. D. *Science* **1998**, *279*, 548.

1.6 Figure Captions

Fig. 1-1 Structure of Y zeolite.

Fig. 1-2 XRD patterns of MCM-41.

Fig. 1-3 Possible mechanistic pathways for the formation of MCM-41: (1) liquid-crystal-phase-initiated and (2) silicate-anion-initiated.

Fig. 1-4 Scheme of functionalization of MCM-41.

Fig. 1-5 XRD patterns of SBA-15.

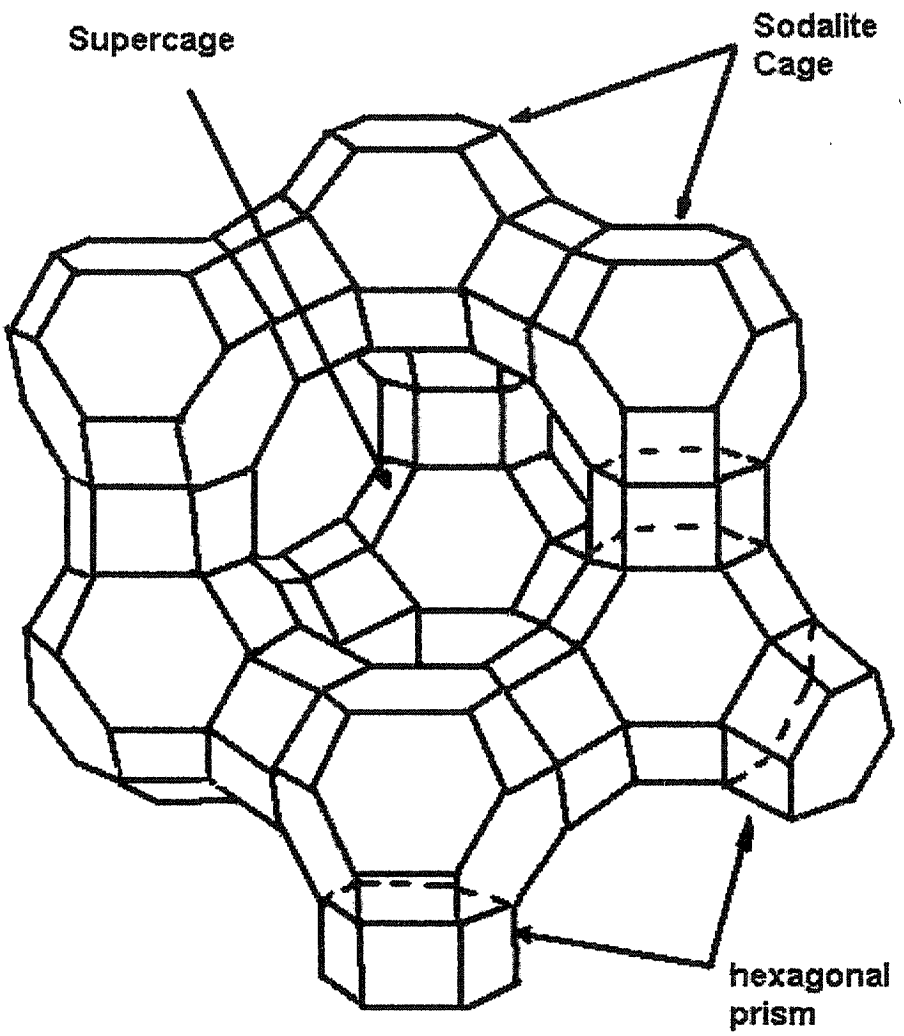

Fig. 1-1

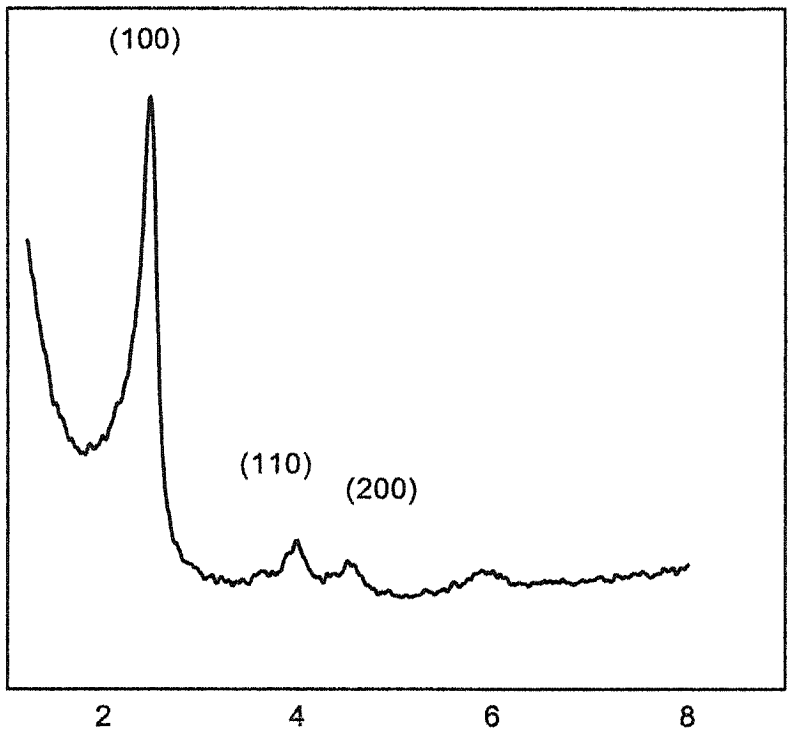

Fig. 1-2

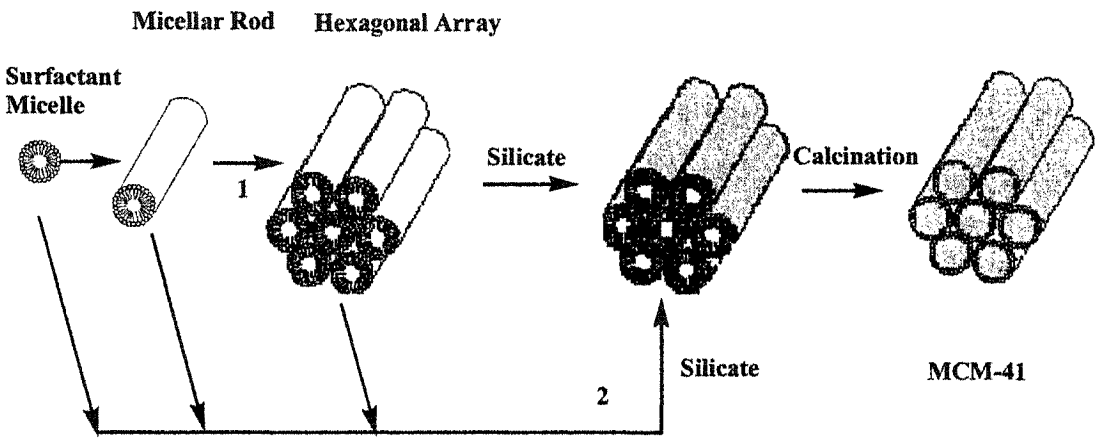

Fig. 1-3

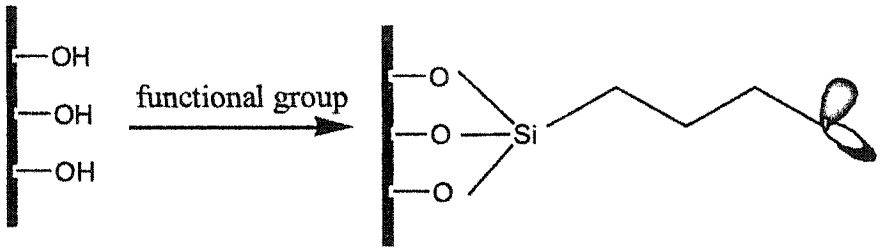

Fig. 1-4

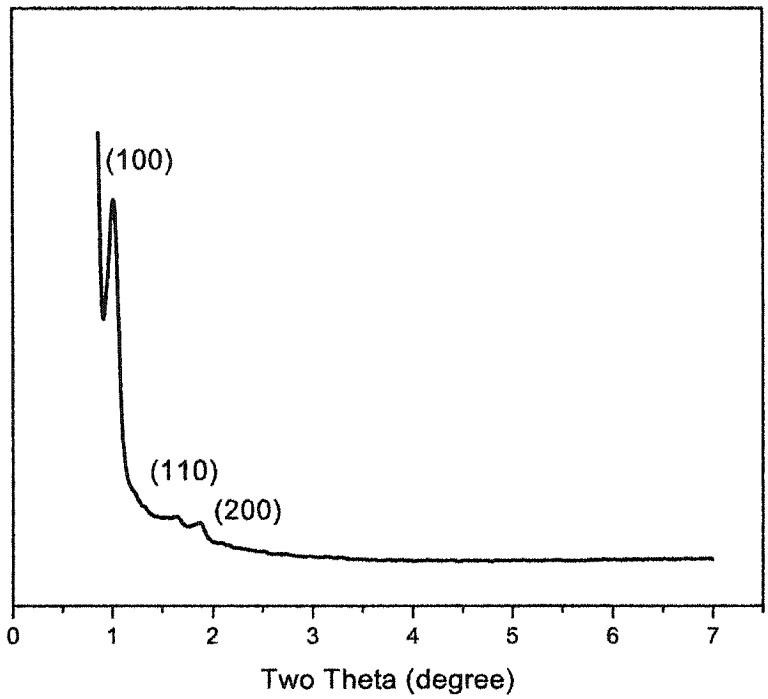

Fig. 1-5

Chapter 2: Aggregation of Tetrakis(p-sulfonatophenyl) porphyrin within Modified Mesoporous MCM-41

2.1 Introduction to Aggregation

Molecular aggregates are self-assembled molecules due to strong molecular Van der Waals-like attractive force. Molecular aggregates are a subject of intense interest because of their significant technological applications in molecular opto-electronic devices, such as spectral sensitizers, organic photoconductors, optical probes, to name a few.

Molecular aggregates in which the individual molecules (monomers) are arranged in a regular fashion can be classified as J-aggregates and H-aggregates, defined by the relative orientations of induced transition dipoles of the constituent molecules. The J-aggregate is a one-dimensional molecular structure stacked in such a way that the transition moments of individual monomers are parallel to the line joining their centers (head to tail arrangement). The H-aggregate is also a one-dimensional array of molecules in which the transition moments of individual monomers are aligned parallel to each other but perpendicular to the line joining their centers (head to head arrangement). The most characteristic feature of J-aggregates is that they exhibit a narrow red-shifted peak (J-band) in the absorption spectrum with respect to the monomer absorption. The absorption spectrum of the H-aggregate consists of a blue-shifted band (generally broader than the J-band) compared to the monomer absorption. The J aggregate dye is most technologically important for photographically sensitization. The energy shift of the absorption bands of the aggregates has been explained by molecular exciton coupling theory.

The dye molecule can be considered as a point dipole. The energy of the excitonic state of the aggregated dye splits into two levels though the interaction of the transition dipoles, shown in Fig. 2-1.[1] Assuming side by side one dimensional arrangement of monomers in the J-aggregate, the coherence length is (N+1) times of the monomer radius. The energy difference of the excited and ground state of the molecule can be written as:

$$\Delta E=\Delta E_N+D+\varepsilon \quad (1)$$

where ΔE_N is excitation energy in molecule N of the aggregate; D is an exchange energy, which corresponds to the interaction of excited and ground state molecules with the remaining molecules of aggregate, ε is associated energy with the molecule being in the aggregate. Depending on the atomic oscillator strength, for an array of Nc molecules, the energy splitting ($\Delta\varepsilon$) is given by one equation:

$$\Delta\varepsilon=\Delta\varepsilon_0 \operatorname{Cos}\{\pi/(Nc+1)\} \quad (2)$$

where $\Delta\varepsilon_0$ is the splitting energy as $N\rightarrow\infty$.[2, 3]

Two well known classes of molecules, which form spontaneous molecular aggregates, are symmetrically substituted porphyrins and cyaines (typical dye structures consist of two heteroaromatic fragments linked by a polymethine chain). The dye aggregates rely on the structure of the dye itself and also on the environment parameters, such as pH, ionic strength, concentration, solvent polarity and temperature. For instance, the porphyrin, meso-tetrakis (4-sulphonatophenyl) porphyrin (TSPP) forms J-aggregate spontaneously at very low pH or at very high

ionic strength. While 1,1',3,3'-tetraethyl-5,5',6,6'-tetrachlorobenzimidazolocarbocyanine (TTBC) forms J-aggregate at a high pH value.

2.2 Background

Porphyrin aggregates are formed from monomers that are initially distributed in a medium and self- assembed without the formation of covalent linkages. They are attracting increased experimental and theoretical attention. Such aggregates are important as model composite structures in understanding the roles that optically induced transient structural changes and photon dynamics play in photosynthesis.[4,5] In addition, through the study of the spectral properties and photodynamic behaviors of aggregated porphyrin structures, an important possible outcome one sought is the translation of the electron transfer specificities and rates often found for biological reactions to the realm of molecular photonic devices (i.e., biomimetics) or photonic materials; numerous interest in the applications area has been evidenced.[6,7] Thus, studies of structures and optical dynamics of porphyrin aggregates have both scientific and technological importance.

Examples of research efforts in this laboratory involving porphyrin aggregates include homogeneous solution entities as well as adsorbates on electrode surfaces. We have, specifically, conducted solution studies dealing with aggregate formation by porphyrins with negatively charged aryl substituents at meso positions (for instance, TSPP, see Fig. 2-2 for structure.[8-10]) Our heterogeneous electrode studies have dealt with TSPP[11] as well as selected metallo-TSPP complexes.[12] In this chapter, we expand our interest and develop a method to form the aggregated TSPP encapsulated within an aluminosilicate mesostructure, in particular, MCM-41. The

porphyrin aggregate formed within the pores of the MCM-41 is verified to be the so-called J-aggregate by the spectrum studies. The composite structure (aggregated TSPP within the pores of MCM-41) represents a new "ship-in-a-bottle-type" nanomaterial whose properties derive from exciton energies and dynamics that are attributable to quantum confinement. This quantum confinement results from both the restricted growth region available to the spontaneously self-assembled molecular aggregate, which forms when TSPP monomers are protonated (and form the dianion) under strongly acidic conditions, and the inherent confinement (characterized in terms of a coherence length)[13-15] of the exciton's movement among a subset of coherently responding molecules within the physical aggregate.

To stabilize the synthesized MCM-41 and allow the formation of aggregated TSPP from the occluded monomers, we found it necessary to modify the interior structure of the mesoporous silica through use of an alkoxysilane silylation reagent. Specifically, we used (aminopropyl) triethoxysilane (APTES; $NH_2(CH_2)_3Si(C_2H_5O)_3$), which satisfies guest-host intermolecular and/or electrostatic interactions and links oxygens at the interface, thus rigidifying it. The positive electrostatic interaction arises from modification of the surface with NH_2, which under pH control can be converted to NH_3^+, thus providing a strong attractive interaction with the sulfonate groups of the porphyrin to capture the monomer TSPP within the channel. Various MCM-41/TSPP assemblies were obtained through simple ion exchange reactions between the positively charge functional agent and the TSPP monomer in different ratios. This method makes possible the uniform loading within the silicate matrix with a high amount TSPP monomer without

collapsing the architecture of MCM-41. Upon acidifying filtered residues containing various assemblies in a programmed way, thereby changing the pH of the microenvironment within the cavity of the mesoporous material, conditions were attained where first the occluded protonated monomer (i.e., the dianion) and then the J-aggregated TSPP were formed.

2.3 Experimental

Synthesis of MCM-41 Polycrystalline powders of the mesostructural aluminosilicate MCM-41 were prepared by using cetyltrimethylammonium bromide (CTAB) as the template.[16,17] A Na_2SiO_3 (Aldrich, ~27% SiO_2) solution and a calculated amount of $NaAlO_2$ (Alfa) solution (Si/Al = 20) were added to CTAB (Aldrich) solution according to the molar composition ratio $5SiO_2$:$0.125Al_2O_3$:CTAB:$610H_2O$. The pH was lowered to 11 with 2 M H_2SO_4 and the mixture was stirred for more than 3 h at about 318 K. Then the temperature was raised to 373 K and the reaction allowed for 72 h in a Teflon-lined autoclave. The resultant precipitate was filtered, washed thoroughly with distilled water, and calcined in air at 773 K to obtain the final product MCM-41 (see below for XRD patterns and their interpretations).

Modification of MCM-41 Several detailed reports have been recently published describing MCM-41 surface modifications using alkoxysilane-coupling agents.[18-25] For our studies, the modified MCM-41 was prepared according to a procedure detailed in ref 18. Approximately, 1.5 g of the calcined MCM-41 was mixed with a chloroform solution of APTES (100 mL, 0.2 M) and stirred overnight

at room temperature. The precipitate was filtered and washed with chloroform and dichloromethane.

Formation of TSPP/MCM-41 composites A typical ion-exchange preparation of a TSPP/MCM-41 composite involved stirring a mixture of 300 mg of modified MCM-41, 5 mg of TSPP, and 25 mL of distilled water for over 24 h at room temperature with the pH held at about 5.0 using 2 M H_2SO_4. The solution was then centrifuged and the supernatant aqueous solution decanted. The filtrate was washed several times with pH 5 water to remove TSPP monomers at the external surface, and then dried in air; no conversion of occluded monomer to surface monomer occurred with time, as evidenced by the absence of TSPP in subsequent wash solutions. The resultant residue is here designated as TSPP-M/MCM-41, where TSPP-M indicates that monomeric TSPP is encapsulated within the modified MCM-41: absorption and emission studies (see section IV) have confirmed the presence of monomer under the above conditions. The final step in forming occluded, aggregated TSPP involved adding 2 M H_2SO_4 to the solid residue. An immediate color change occurred, the residue changed color from dark yellow to olive. The powdered residue was then spectroscopically investigated (see section IV) and identified as the occluded J-aggregated form of TSPP, designated here as TSPP-A/MCM-41.

Instrumentation Absorption spectra were recorded using a Perkin-Elmer, Lambda 18, UV-vis-NIR spectrometer. Steady-state fluorescence spectra were acquired using a SPEX, Fluorolog-τ2 spectrofluorometer. The XRD instrument was a Rigaku diffractometer using Cu $K\alpha_1$ (0.154 nm) X-ray: typically run at a voltage

of 40 kV and current of 30 mA. Raman spectra was gotten by SPEX 1877, 06m triple spectrometer, coupled with a Spex Spectrum-1 CCD camera maintained at 140K by liquid nitrogen. The laser radiation was supplied by a coherent innova 200 argon-ion laser. Raman spectra of the aggregate composites were resonantly excited with laser radiation of wavelength 488nm in order to enhance scattering signals for the corresponding species. The monomeric composites were excited with laser radiation of wavelength 457 nm. Cross-polarization MAS was done with ^{29}Si in the low power mode with frequency of 63 MHz and a 90° pulse of 5μs and ^{1}H in high power mode with power of 59 MHz and a 90° pulse of 5μs. The contact time used in this study was 8 ms, which has been proven to be long enough to permit full cross polarization for different silicons.

2.4 Results and Discussion

XRD patterns of pristine calcined MCM-41, modified MCM-41, the monomer-incorporated composite (TSPP-M/MCM-41), and the aggregate-incorporated composite (TSPP-A/MCM-41) are shown in Fig. 2-3. It was found that, after the silylation reaction and likely formation of a monolayer of silyation product on the surface walls, the XRD pattern of the modified MCM-41 was essentially identical to that of the original calcined MCM-41. Using Bragg's equation and comparison with reference studies (Equation (2) mentioned in chapter 1),[19,26,27] the pore size of calcined MCM-41 was calculated to be ca. 33 Å. Additionally, upon attachment of the (putative) monolayer of silylation product to the internal channels of the calcined MCM-41, the pore size was estimated to be narrowed to ca. 24 Å, again through the use of the Bragg equation and the equation mentioned above. An

opening of 24 Å was sufficiently large to allow TSPP, of approximate dimensions (14 ×14) $Å^2$, to be incorporated into the modified MCM-41.

The XRD patterns of TSPP-M/MCM-41 and TSPP-A/MCM-41 showed strong (100) peaks and proportional (110) and (200) peak intensities, suggesting that a high framework stability was maintained for the modified MCM-41 regardless whether monomeric or aggregated TSPP was incorporated. The differences in relative intensities that occurred are likely due to electrostatic interaction between sulfonato groups of TSPP and the interior walls of the cage, as well as with the aggregate's transverse dimension as it grows along the channel length of MCM-41.

Solid-state NMR was used to study the structure and the chemical bonding of the functionalized MCM-41 and TSPP/MCM-41 composite.[28] The ^1H and ^{29}Si cross-polarization experiment restricted detection of an NMR signal to silicon nuclei that became protons, i.e, at or near the surface. Therefore, ^{29}Si CP/MAS NMR is a sensitive and reliable technique for qualitative and quantitative characterization of SiOH group on solid surfaces. Fig. 2-4 shows the ^{29}Si CP/MAS NMR spectra for calcined MCM-41(A), modified MCM-41(B) and monomeric TSPP-5-M/MCM-41(C) samples. For the calcined sample without silylation, three peaks could be observed near ~100ppm by multipeak fitting. The fitting result is illustrated in Fig. 2-5. Compared with reference 28, the low-intensity peak at ~92 ppm corresponded to surface silicon atoms with two siloxane bonds and two silanol groups, i.e., geminal silanol sites, $(SiO)_2*Si(OH)_2(Q^2)$, which may be either single or hydrogen-bonded, and the resonance at –100 ppm was attributed to surface silicon atoms with three siloxane bonds and one silanol group, i.e., isolated silanol

sites, $(SiO)_3$*SiOH(Q^3), while the resonance at -110 ppm was caused by surface silicon atoms with four siloxane bonds, i.e., $(SiO)_4$*Si(Q^4)[29]. For two silated samples, modified MCM-41 and monomeric TSPP-5-M/MCM-41, one observed intensity changes of Q^3 and Q^4 silicon resonance peaks. The relative intensity of Q^3 underwent a dramatically decrement but the Q^4 silicon resonance was substantially increased. This relative intensity difference of these silicon sites was thought to be attributable to the reactions of surface SiOH groups with APTES, forming more SiO bonds. For TSPP-5-M/MCM-41 sample, the relative intensity of Q^3 resonance slightly increased compared with modified MCM-41, which suggested that during the incorporation of TSPP within MCM-41 in aqueous solution, some new isolated silanol sites were brought up on the surfaces.

In part B and C of Fig. 2-4, three additional peaks from –50 to –80 ppm correspond to three different environments for the siloxane groups in the functionalized monlayers. Similar to monolayers formed by using (methoxyl) mercaptopropylsilane (TMMPS) as the silylation agent[30], these three peaks stands for different environments, whose schematic representation of monolayer with different conformation is shown in Fig. 2-6: (a) -50 ppm comes from isolated groups that are not bound to any neighboring siloxanes, (b) -58ppm arises from terminal groups that are only bound to one neighboring siloxane, and (c) -66 ppm is resonance of cross-linked groups that are bound to two neighboring siloxanes. After modification, it should be noted that among the three, the most dominant peak comes from cross-linked siloxane group. Comparing this with the reference 30, we deduced that the surface coverage of functionalized monolayers on mesoporous

MCM-41 was larger than 50%. As illustrated, there were almost no changes in the relative intensities for modified MCM-41 and TSPP-5-M/TSPP, indicating that the monolayers formed by silylation were very stable.

We discovered it is necessary to modify the interface with APTES and adjust the pH value to a weak acid around 5. Only in an acidic condition, where the surface attached amino groups of APTES are protonated and positively charged, TSPP with its negatively charged sulfonato groups was capable of fixing in the channel of MCM-41. In order to prove this, we did experiments to intercalate TSPP into either the calcined or modified forms of MCM-41 under basic conditions, but all attempts were unsuccessful. We ascertain that the unfavorable surface electrostatics force prevents ion exchange in the cavity.

Diffuse reflectance (DR) UV-vis spectra of the composites designated TSPP-M/MCM-41 and TSPP-A/MCM-41 are shown in Fig. 2-7. Also included in this figure, for comparison purposes, are transmission UV-vis spectra of TSPP in solution under different pH conditions that have been shown to create either free-base or aggregated TSPP solution species.

The existence of aggregates of TSPP (i.e., the so-called J-aggregate) in homogeneous solution is indicated by the presence of a sharp J-type absorption band at 490 nm (B-band or Soret band, $S_0 \rightarrow S_2$) accompanied by a weak band at 705 nm (Q-band, $S_0 \rightarrow S_1$).[8-10,31,32] The J-aggregate has been shown to be composed of protonated TSPP (i.e., dianionic $H_4^{2+}TSPP^{4-}$) as the monomeric unit, as indicated by spectral titration-type studies that revealed the growth of the aggregate band

intensity at the expense of intensity of the dianion 432-nm band.[8] Additionally, aggregation was also indicated by the remarkable enhancement of low-frequency Raman bands at 241 and 317 cm^{-1} when resonance excitation (e.g., radiation in resonance with the 490 nm absorption) is used to excite the Raman spectrum, see Fig. 2-8.[33,34] In this regard, Raman spectra for the composite materials were also acquired and clearly showed the existence of either occluded monomer or aggregate. The Raman spectra suggested that the formation of TSPP aggregate resulted from the detachment of most of monomeric TSPP molecules at the MCM-41 surface wall.

Returning to Fig. 2-7, it is observed that the encapsulated free-base monomer exhibits a blue shift for its Soret-region band (396 nm) if compared to the Soret band (413 nm) of the solution monomeric species. A blue shift for the absorption for the encapsulated aggregate is observed when compared to the solution aggregate: 487 vs 490 nm, respectively. Such shifts can be explained in terms of intramolecular charge transfer attributable to host-guest interaction, which is connected to steric effects associated with the pore structure within modified MCM-41.

Additionally, the broad structure for the Soret-type band for TSPP-M/MCM-41 (in Fig. 2-7) could be interpreted as site-specific absorptions for encapsulated TSPP, suggesting that the monomeric species is distributed at various positions within the cage and experiences, as a result, a range of perturbations. However, we found out the spectrum of TSPP-A/MCM-41 and solution phase aggregate were similar, in terms of both band positions and widths. It could be interpreted as indicating that upon formation of the aggregate, the molecules were coupled and realigned such

that site-specific perturbations to the exciton absorption energy, line width, and possibly other properties were diminished.

The composites with different ratios of TSPP over modified MCM-41 were prepared. Their monomeric and aggregated diffusion reflectance UV-vis spectra are illustrated in Fig. 2-9 and Fig. 2-10, separately. For all monomeric composites with the loading amount of TSPP decreased from 30 mg to 2.5 mg, more significant blue shifts from 402nm to 392nm were observed because of more active sites provided by $-NH_3^+$(Fig. 2-9), thus stronger interaction happens between the sulfonato groups of TSPP and the modified AlMCM-41. The soret bands for the monomeric composites were broadened with an increase of the amount of TSPP loaded, which can be explained by the site specific effect, i.e., a wider range of perturbations for more TSPP occluded. The J-aggregate absorptions for all aggregated composites occurred from 486 to 488nm (Fig. 2-10), and compared with monomeric composites, less blue shifts are observed, indicating that the J-aggregated TSPP formed within the core of modified MCM-41 was more integrated.

Fluorescence spectra for solution phase and composite systems were also acquired. As shown in Fig. 2-11A and B, which were acquired with excitation at 410 nm, the Q-band emission from monomeric TSPP in solution and the composite TSPP-M/MCM-41 is essentially identical, except for the small shift between emission peaks, indicating that the monomer TSPP chromophore was the emitting species in the composite. In this case, two emission peaks, Q(0,0) and Q(0,1), are absolutely the mirror images of their corresponding absorption bands (see Fig.2-7) at Q(0,0) and Q(1,0).[6]

In the case of aggregated TSPP in solution and the composite TSPP-A/MCM-41, the fluorescence spectra excited at 490 nm are shown in parts C and D of Fig. 2-11, respectively. One finds that emission band at ca. 715 nm was observed for each sample, which is exactly what is to be expected for mirror emission associated with the corresponding absorption shown in Fig. 2-7.

The combination of studies above no doubt indicates that we have successfully incorporated aggregated TSPP within the cavities of the modified MCM-41. It is also of note that we were able to load as much as 10 wt % TSPP into the mesoporous material, because of the large internal surface area of the mesoporous material, which was one of its intrinsic properties.

As shown earlier, through a conflation of electronic absorption, fluorescence, fluorescence-excitation, and vibrational Raman spectra of selected homogeneous solution phase tetraaryl-substituted porphyrins (free-base and protonated), N-protonation induced structural changes that promoted aggregation.[9] It was deduced that a basic requirement for aggregation is that the protonated species should be zwitterionic.[9] We have gone further and suggested that the molecular subunits in the tetraaryl-substituted porphyrin aggregates were arranged in a cofacial fashion with a displacement between nearest neighbors such that oppositely charged sites (positively charged central nitrogens and negatively charged sulfonato groups) were positioned close to one another, giving rise to J-aggregate type arrangements (e.g., a spread "deck of cards" and/or "zigzag," both corresponding to head-to-tail alignments of the transition dipole moments).[35] These two possible TSPP J-aggregates are shown in Fig. 2-12. Such aggregates, presumably, would

form along the one-dimensional cylindrical channels of the modified MCM-41 aluminosilicate, with electrostatic interaction between the sulfonato groups and ammonium ions of the silylation reagent contributing to the stability of the structure. Moreover, such structures would be impacted by the electrostatic interaction between negative sulfonatophenyl groups and positive macrocycle groups within the aligned molecules.

2.5 Bibliography

1. Mishra, A.; Behera, R. K.; Behera, P. K.; Mishra B. K.; Behera G. B. *Chem. Rev.* **2000**, *100*, 1973.
2. Akins, D. L. *J. Phys. Chem.* **1986**, *90*, 1530.
3. Koti, A. S. R.; Taneja, J.; Periasamy, N. *Chem. Phys. Lett.* **2003**, *375*, 171.
4. Okamura, M. Y.; Feher, G.; Nelson, N. In *Photosynthesis*; Govindjee, Ed.; Academic Press: New York, **1982**; pp 195-272.
5. Pearlstein, R. M. In *Photosynthesis*; Amesz, J., Ed.; Elsevier: Amsterdam, **1987**; pp 299-317.
6. O'Neil, M. P.; Niemcyzk, M. P.; Svec, W. A.; Gosztola, D.; Gaines, G. L., III; Wasielewski, M. R. *Science* **1992**, *257*, 63.
7. Wagner, R. W.; Lindsey, J. S.; Seth, J.; Palaniappan, V.; Bocian, D. F. *J. Am. Chem. Soc.* **1996**, *118*, 3996.
8. Akins, D. L.; Zhu, H.-R.; Guo, C. *J. Phys. Chem.* **1994**, *98*, 3612.
9. Akins, D. L.; Zhu, H.-R.; Guo, C. *J. Phys. Chem.* **1996**, *100*, 5420.
10. Akins, D. L. In *J-Aggregate*; Kobayashi, T., Ed.; World Scientific: Singapore, **1996**; pp 67-94.
11. Guo, C.; Ren, B.; Akins, D. L. *J. Phys. Chem. B* **1998**, *102*, 8751.
12. Guo, C.; Ren, B.; Akins, D. L. *J. Phys. Chem.* In revision.
13. Grad, J.; Hernandez, G.; Mukamel, S. *Phys. Rev. A* **1988**, *37*, 3835.
14. Spano, F. C.; Mukamel, S. *J. Chem. Phys.* **1989**, *91*, 683.
15. Spano, F. C.; Kuklinski, J. R.; Mukamel, S. *J. Chem. Phys.* **1991**, *94*, 7534.

16. Kresge, C. T.; Leonowicz, M. E.; Roth, W. J.; Vartuli, J. C.; Beck, J. S. *Nature* **1992**, *359*, 710.

17. Beck, J. S.; Vartuli, J. C.; Roth, W. J.; Leonowicz, M. E.; Kresge, C. T.; Schmitt, K. D.; Chu, C. T.-W.; Olsen, D. H.; Sheppard, E. W.; McCullen, B.; Higgins, J. B.; Schlenker, J. L. *J. Am. Chem. Soc.* **1992**, *114*, 10834.

18. Liu, C.-J.; Li, S.-G.; Pang, W.-Q.; Che, C.-M. *Chem. Commun.* **1997**, *65*, 78.

19. Mercier, L.; Pinnavaia, T. J. *Adv. Mater.* **1997**, *9*, 500.

20. (a) Feng, X.; Fryxell, G. E.; Wang, L. Q.; Kim, A. Y.; Liu, J.; Kemner, K. M. *Science* **1997**, *276*, 923. (b) Liu, J.; Feng, X.; Fryxell, G. E.; Wang, L. Q.; Kim, A. Y.; Gong, M. *Adv. Mater.* **1998**, *10*, 161.

21. (a) Cauvel, A.; Renard, G.; Brunel, D. *J. Org. Chem.* **1997**, *62*, 749. (b) Brunel, D.; Cauvel, A.; Fajula, F.; DiRenzo, F. *Stud. Surf. Sci. Catal.* **1995**, *97*, 173.

22. Sutra, P.; Brunel, D. *Chem. Commun.* **1996**, 2485.

23. Bellocq, N.; Brunel, D.; Lasperas, M.; Moreau, P. *Stud. Surf. Sci. Catal.* **1997**, *108*, 485.

24. Subba Rao, Y. V.; De Vos, D. E.; Bein, T.; Jacobs, P. A. *Chem. Commun.* **1997**, 355. (b) Subba Rao, Y. V.; De Vos, D. E.; Jacobs, P. A. *Angew. Chem., Int. Ed. Engl.* **1997**, *36*, 2661.

25. Diaz, J. F.; Balkus, K. J., Jr.; Bedioui, F.; Kurshev, V.; Kevan, L. *Chem. Mater.* **1997**, *9*, 61.

26. Sung-Suh, Hyung Mi; Luan, Z.; Kevan, L. *J. Phys. Chem. B* **1997**, *101*, 10455.

27. Stucky, G. D.; Monnier, A.; Schuth, F.; Huo, Q.; Margolese, D.; Kumar, D.; Kridhnamurty, M.; Petroff, P.; Firouzi, A.; Janicke, M.; Chmelka, B. F. *Mol. Cryst. Liq. Cryst.* **1994**, *240*, 187.

28. Sindorf, D. W.; Macier, G. E. *J Am. Chem.Soc.* **1983**, *105*, 3769.

29. Subba Rao, Y. V.; De Vos, D. E.; Jacobs, P. A. *Angew. Chem., Int. Ed. Engl.* **1997**, *36*, 2661.

30. Feng, X.; Fryxell, G. E.; Wang, L. Q.; Kim, A. Y.; Liu, J.; Kemner, K. M. *Science* **1997**, *276*, 923.

31. Akins, D. L.; Özcelik, S.; Zhu, H.-R.; Guo, C. *J. Phys. Chem.* **1996**, *100*, 14396.

32. Ohno, O.; Kaizu, Y.; Kobayashi, H. *J. Chem. Phys.* **1993**, *99*, 4128.

33. Akins, D. L. *J. Phys. Chem.* **1986**, *90*, 1530.

34. Akins, D. L.; Akpabli, C. K.; Li, X. *J. Phys. Chem.* **1989**, *93*, 1977.

35. Kasha, M. *Radiat. Res.* **1963**, *20*, 55.

36. Kubelka, P. *J. Opt. Soc. Am.* **1948**, *38*, 448.

2.6 Figure Captions

Fig. 2-1 Schematic representation of the relationship between chromophore arrangement and spectral shift based on molecular exciton theory.

Fig. 2-2 Structure of tetrakis(*p*-sulfonatophenyl)porphyrin (TSPP).

Fig. 2-3 XRD patterns of (A) calcined MCM-41, (B) modified MCM-41, (C) TSPP-M/MCM-41 and (D) TSPP-A/MCM-41.

Fig. 2-4 CP/MAS ^{29}Si NMR spectra of (A) calcined MCM-41, (B) modified MCM-41 and (C) monomeric TSPP-5-M/MCM-41.

Fig. 2-5 Multipeaking fitting of CP/MAS ^{29}Si NMR spectrum for monomeric TSPP-5-M/MCM-41.

Fig. 2-6 Schematic conformations of functionalized monolayers on the surface under different conditions.

Fig. 2-7 UV-vis spectra of TSPP in various environments: (A) Homogeneous solution phase monomeric TSPP at 5×10^{-5} M and pH 11 (dashed line), (B) Monomeric TSPP encapsulated in MCM-41 that was modified by surface silylation using (aminopropyl)triethoxysilane (APTES), designation TSPP-M/MCM-41 (dot-dashed line), (C) Solution phase aggregated TSPP formed from monomeric concentration of 5×10^{-5} M and pH 1.5 (dotted line) and (D) Aggregated TSPP encapsulated in MCM-41 that was modified by surface silylation using (aminopropyl)triethoxysilane (APTES), designation TSPP-A/MCM-41 (solid line). *FI*, the label on the right-hand side, refers to the so-called remission function (a linear function of the concentration of

homogeneous absorbers) for diffuse reflection measurements and is calculated from $F\mathrm{I} = (1 - R)^2/2R$. In this expression R is the diffuse reflectance, given by $R = J_0/I_0$, where I_0 is the incident intensity at the surface and J_0 is the intensity of the reflected light.

Fig. 2-8 Raman spectra of aggregated and monomeric TSPP in various environments: (A)TSPP-5-A/MCM-41, excitation wavelength λex=488 nm, integrating time 0.3 second, repeating time 100, (B) solution phase aggregated TSPP formed from monomeric concentration of 5×10^{-5} M and pH=1.5, excitation wavelength λex=488nm, integrating time 10 second, repeating time 100, (C) TSPP-5-M/MCM-41, excitation wavelength λex=457 nm, integrating time 3 second, repeating time 1 and (D) solution phase protonated TSPP with concentration of 5×10^{-5} M and pH=4.0, excitation wavelength λex=457nm, integrating time 10 second, repeating time 1.

Fig. 2-9 DR UV-vis spectra of monomeric composites with different ratios of TSPP over modified MCM-41: (A) 2.5 mg of TSPP and 300 mg of modified MCM-41, designation TSPP-2.5-M/MCM-41 (solid line), (B) 5 mg of TSPP and 300 mg of modified MCM-41, designation TSPP-5-M/MCM-41 (dashed line), (C) 10 mg of TSPP and 300 mg of modified MCM-41, designation TSPP-10-M/MCM-41 (dotted line), (D) 15 mg of TSPP and 300 mg of modified MCM-41, designation TSPP-15-M/MCM-41 (dashe-dotted line) and (E) 30 mg of TSPP and

300 mg of modified MCM-41, designation TSPP-30-M/MCM-41 (dashe-dot-dotted line).

Fig. 2-10 DR UV-vis spectra of aggregated composites with different ratios of TSPP over modified MCM-41: (A) 2.5 mg of TSPP and 300 mg of modified MCM-41, designation TSPP-2.5-A/MCM-41 (solid line), (B) 5 mg of TSPP and 300 mg of modified MCM-41, designation TSPP-5-A/MCM-41 (dashed line), (C) 10 mg of TSPP and 300 mg of modified MCM-41, designation TSPP-10-A/MCM-41 (dotted line), (D) 15 mg of TSPP and 300 mg of modified MCM-41, designation TSPP-15-A/MCM-41 (dashe-dotted line) and (E) 30 mg of TSPP and 300 mg of modified MCM-41, designation TSPP-30-A/MCM-41 (dashe-dot-dotted line).

Fig. 2-11 Fluorescence spectra of (A) (dashed line) monomeric TSPP, 5×10^{-5} M and pH 11, excited at 410 nm, (B) (dot-dashed line) TSPP-M/MCM-41, excited at 410 nm, (C) (dotted line) aggregated TSPP, 5×10^{-5} M and pH 11.5, excited at 490 nm and (D) (solid line) TSPP-A/MCM-41, excited at 490 nm.

Fig. 2-12 Two possible linear J-aggregates (A and B, relating to the zigzag and spread deck of cards, respectively) resulting upon protonation of the macrocycle, which leads to a coplanar alignment of the sulfonatophenyl groups and the macrocycle. It is anticipated that extended structures would exist within the modified MCM-41 cavity.

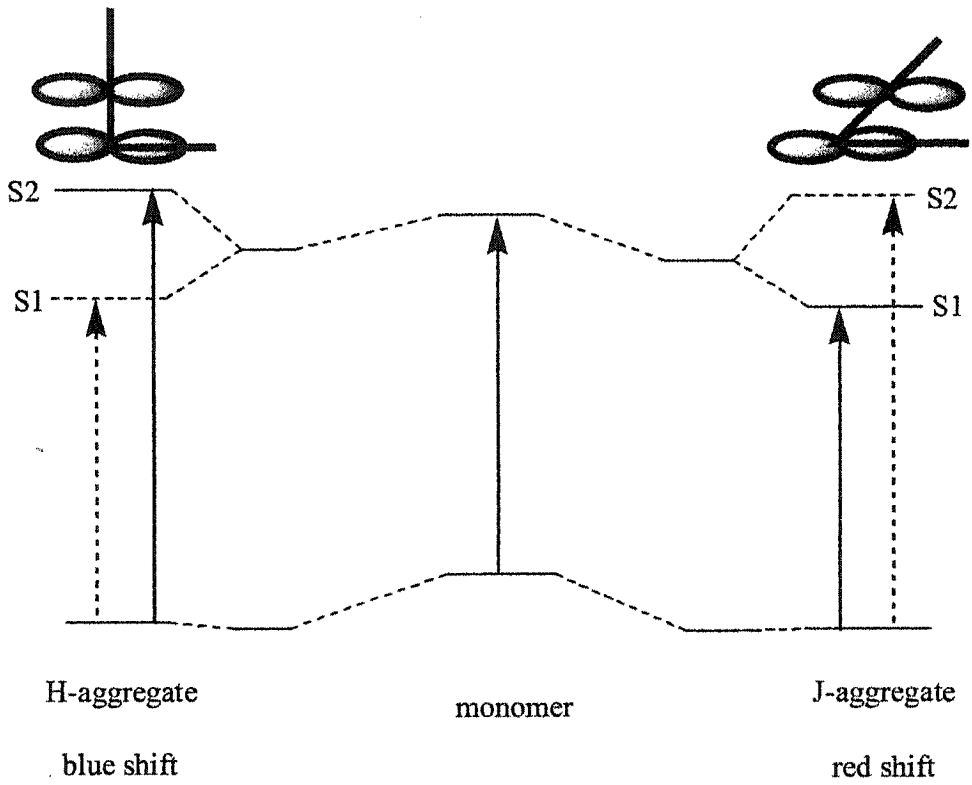

Fig. 2-1

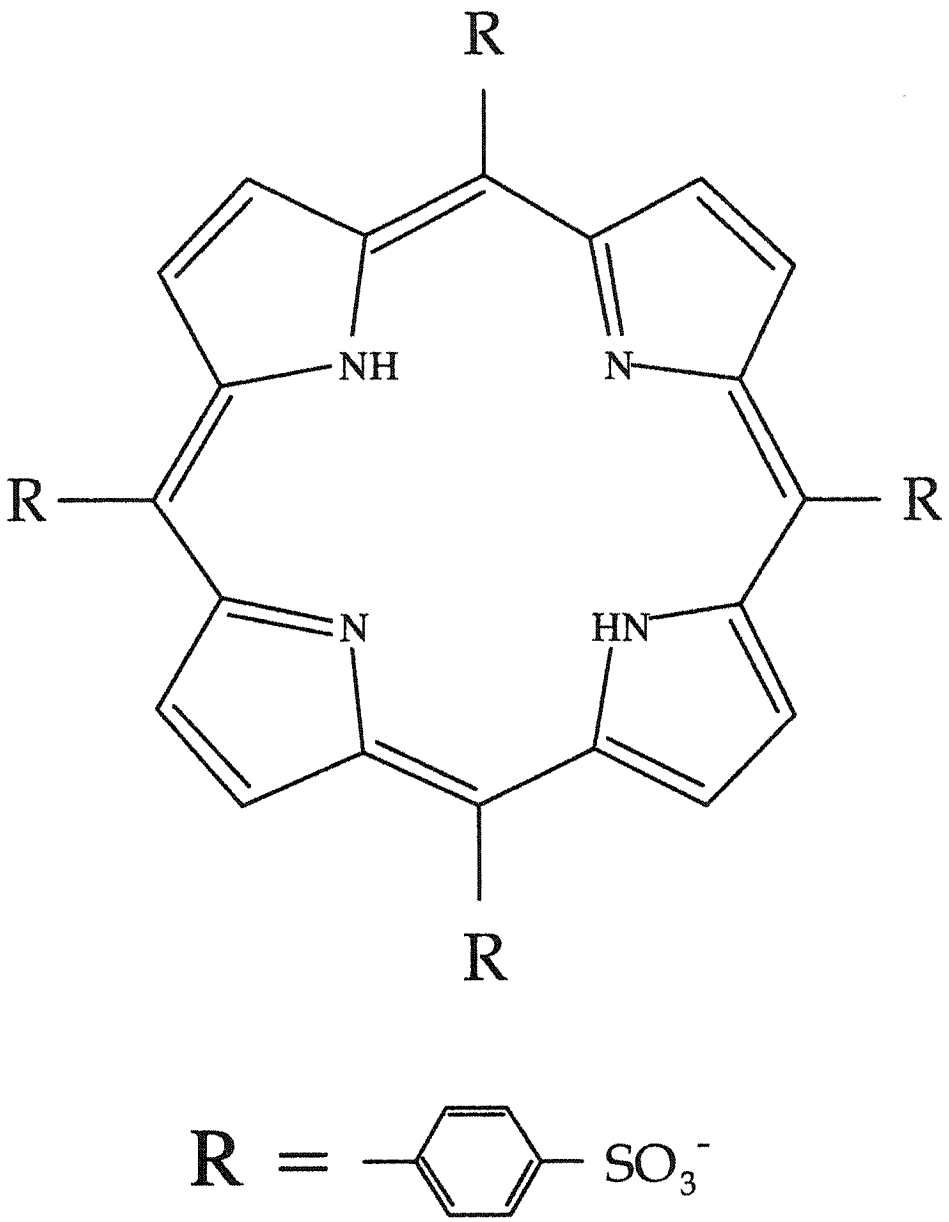

Fig. 2-2

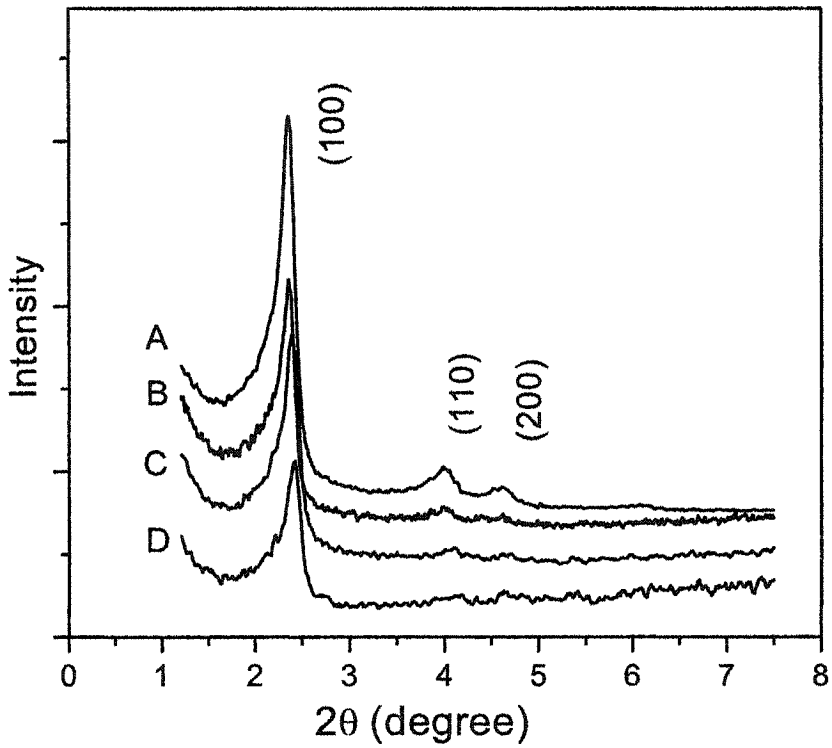

Fig. 2-3

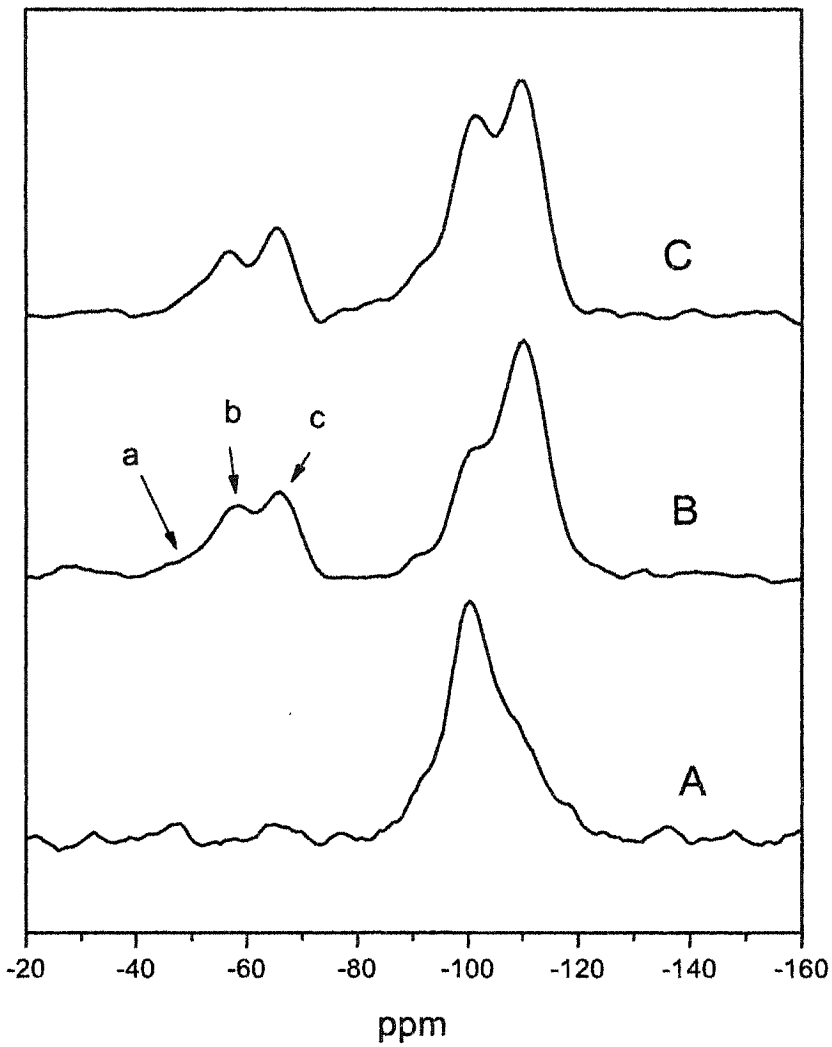

Fig. 2-4

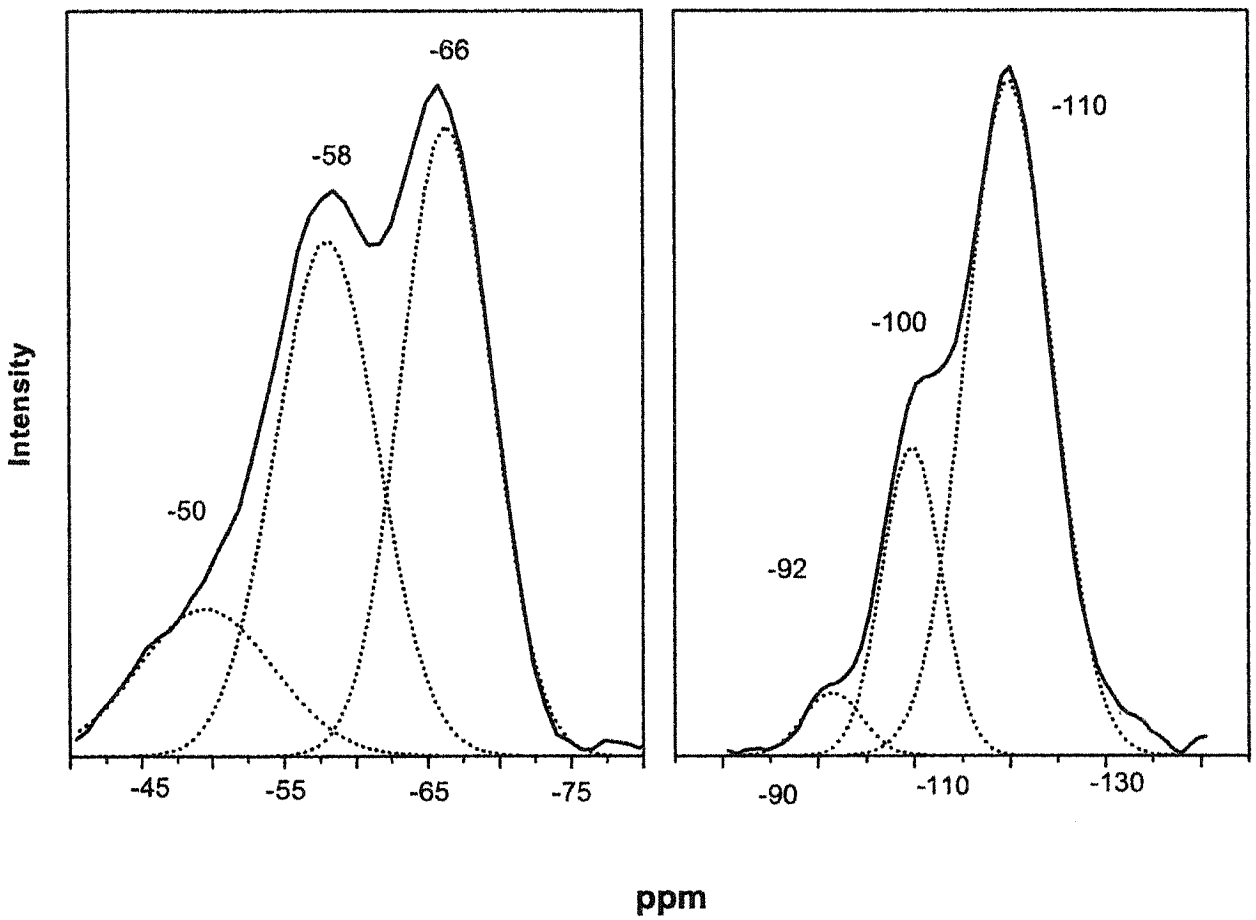

Fig. 2-5

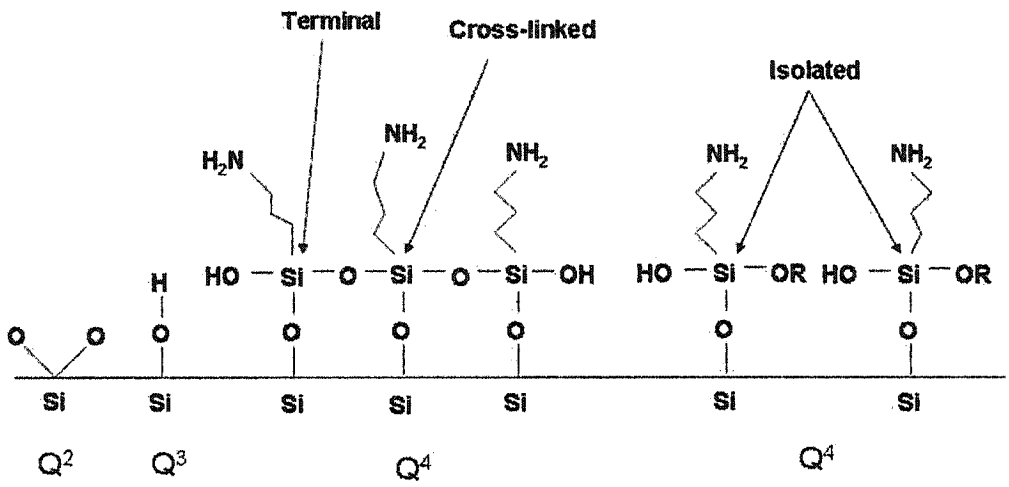

Fig. 2-6

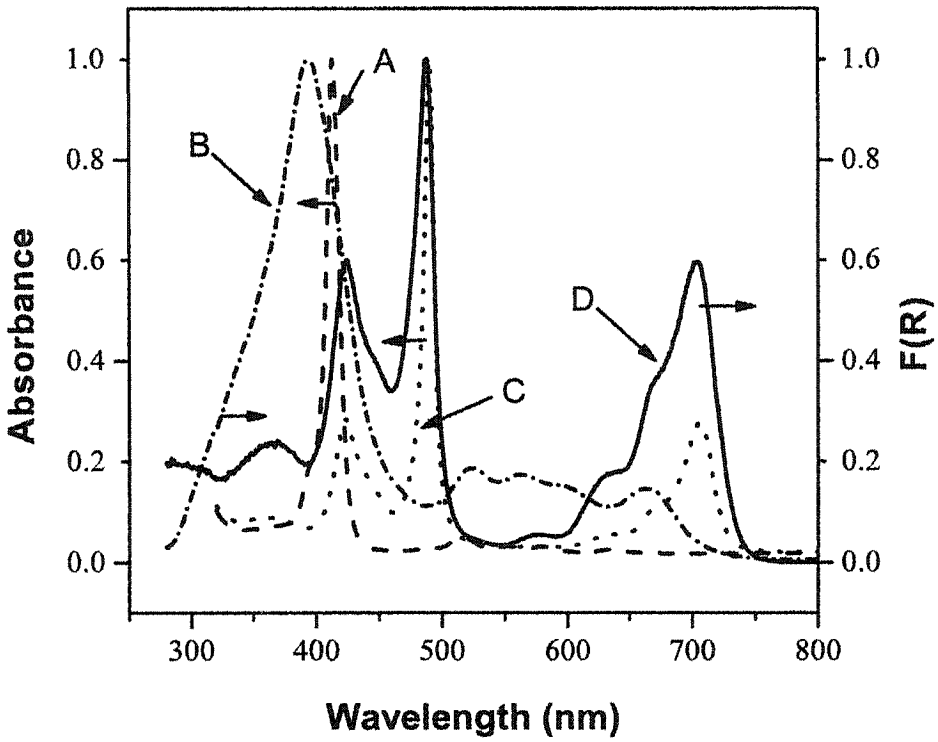

Fig. 2-7

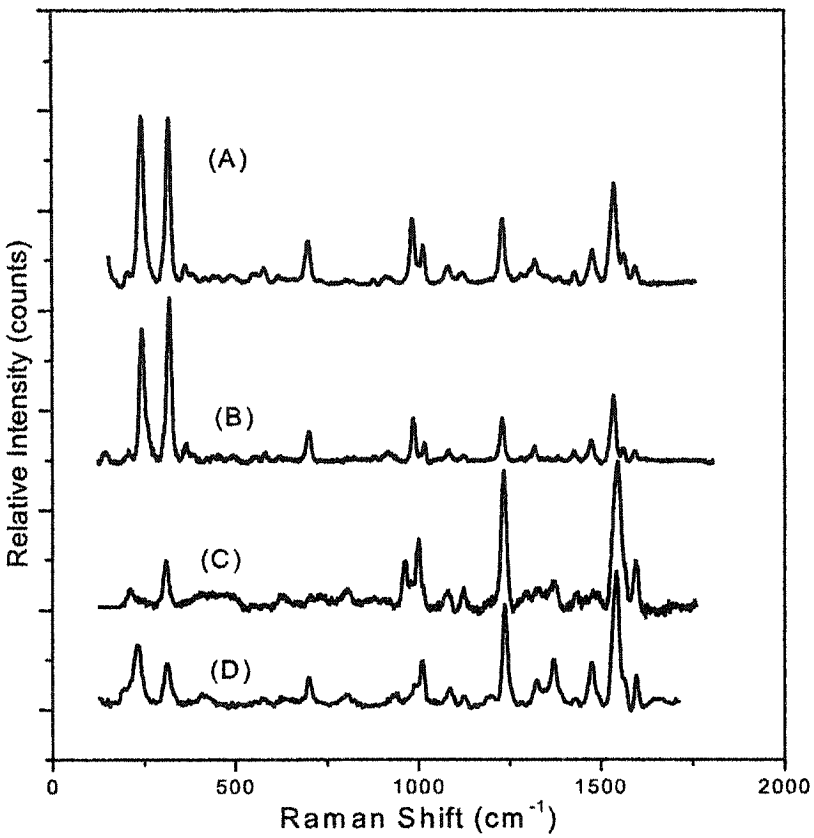

Fig. 2-8

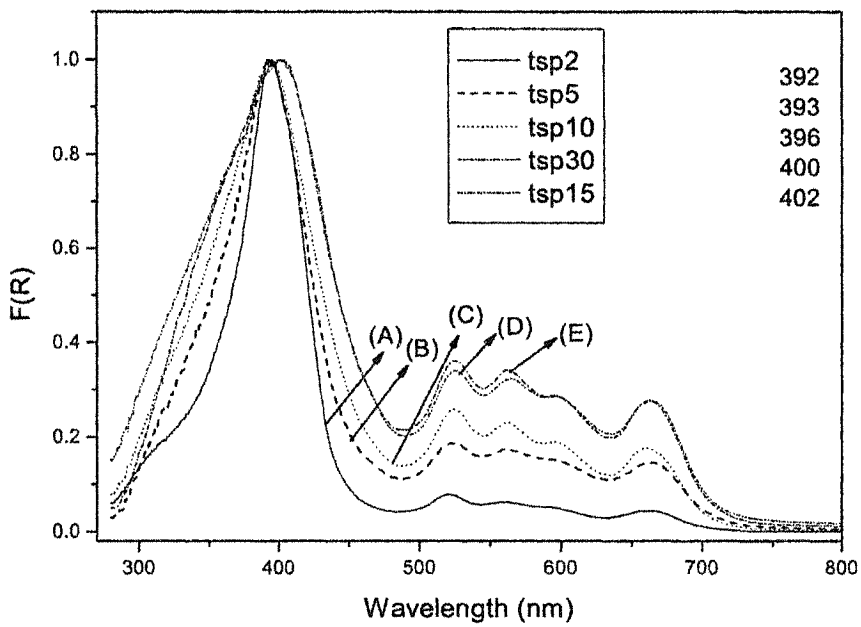

Fig. 2-9

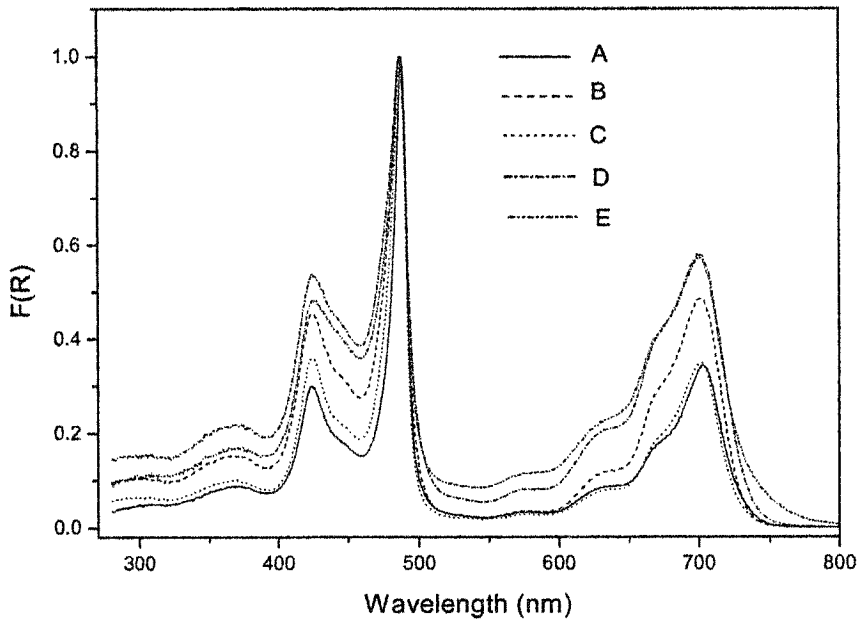

Fig. 2-10

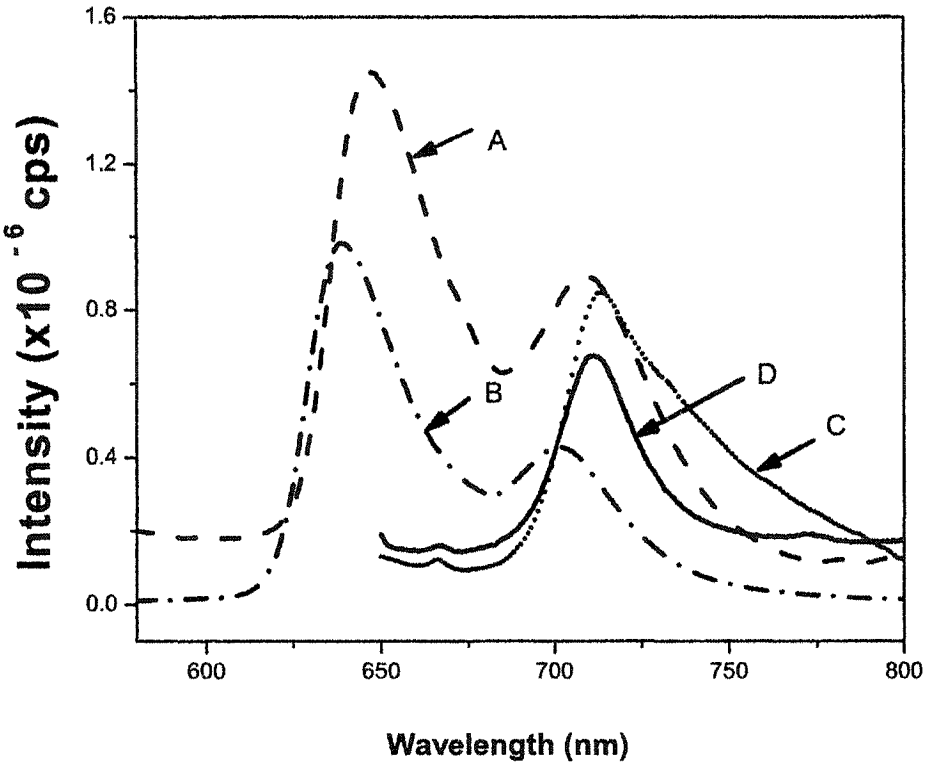

Fig. 2-11

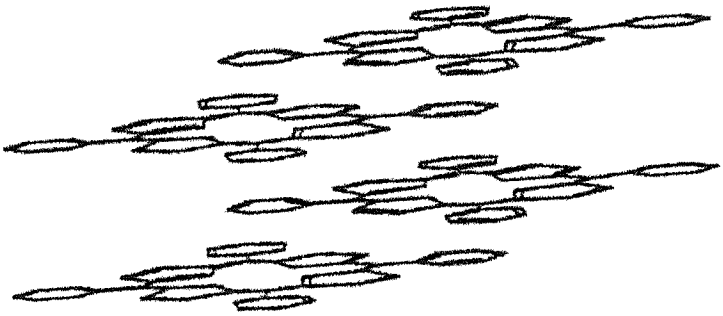

A

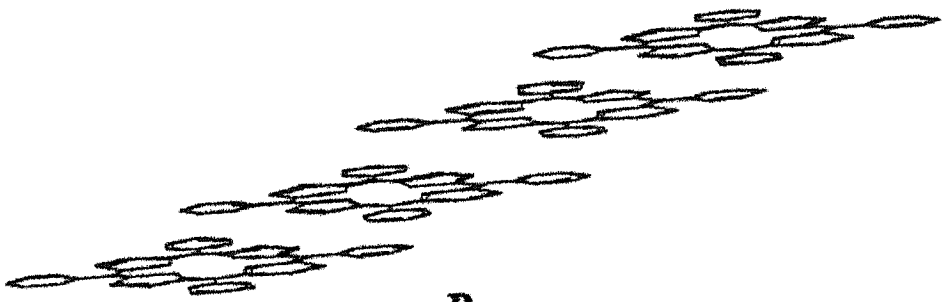

B

Fig. 2-12

Chapter 3: Aggregation and Excitation of Cyanine dye Encapsulated within Modified Mesoporous MCM-41

3.1 Introduction

Spectroscopic and optical dynamics properties of aggregated cyanine dyes in homogeneous systems[1,2] and as adsorbates in heterogeneous systems[3-14] are of considerable scientific interest. In terms of research activities described in the literature involving an occluded species, most efforts exploit the one-dimensional uniform pore sizes and thermal stability of mesoporous siliceous materials as hosts to organize either guest atoms,[15] polymers,[16-18] or organic and inorganic compounds,[19-21] with the aims of creating composite materials with catalytic,[22] environmentally remunerative,[23] or optoelectronic properties.[24] Also, recently, specific types of new efforts in this section include the formation of microlasers from agregated molecules encapsulated in aluminosilicate micron length rods.[25]

The focus of my research with the occluded aggregated cyanine dye was quite distinct from that of the other investigators referenced above. Looking back upon prior studies in our laboratory, we investigated several aggregated cyanine dyes in heterogeneous systems; in particular, with aggregation of cyanine dyes on electrode surfaces[3-14] as well as on the surfaces of different colloidal particles.[26,27] In the latter case, we studied 1,1',3,3'-tetraethyl-5,5',6,6'-tetrachlorobenzimidazolocarbocyanine (referred to as TTBC) adsorbed onto colloidal silica[26] as well as 1,1'-diethyl-3,3'-di(3-sulfopropyl)-5,5',6,6'-tetrachlorobenzimidazolocarbocyanine (referred to as BIC) adsorbed onto colloidal silver.[27] It was found, for both

systems, that a form of lasing occurs, defined by us as superradiant lasing, at phenomenally low optical pumping thresholds.

Interest in molecular aggregates, at the most fundamental level, derives from the opportunity such structures present to study intermolecular interactions that have a decidedly directional character and a resulting reduced degree of freedom for both electronic and nuclear motions. A natural extension of our effort is to examine the formation of cyanine aggregates within a mesoporous silicate, especially aluminum mesoporous silicate. The motivation in this case would be to create an encapsulated species where constraints in aggregate length and orientation, associated with the spatially constricted and directional character of the channel, as well as controls available in the synthesis procedure, result in a new more robust and manipulable nanocomposite, possessing the unique spectroscopic and other optical properties generally associated with cyanine dye aggregates. Our ultimate goal is to employ this novel functional materials for optical and optoelectronic applications.

Moreover, in chapter 2 of this dissertation,[28] I described how we recently developed a technique for encapsulating tetrakis(*p*-sulfonatophenyl)porphyrin, which is referred to as TSPP, within an aluminosilicate, specifically, an aluminum-incorporated MCM-41, and the spectroscopic evidence confirming the encapsulation; in particular, the dramatic changes in absorption and emission spectra upon formation of the occluded aggregate. This composite system has much value as regards proof-of-concept and possibly in regards to its unique absorption property. However, because exciton emission from aggregated

porphyrin B-state (i.e., S_2) molecules to their ground state is dipolar forbidden, the weak emission to the ground S_0 state arises from individual Q-state (i.e., S_1) molecules that are formed through internal conversion of B-state molecules. Such weak emission greatly diminishes the prospect of exploiting the composite for materials or device applications. Aggregated cyanine dyes, on the other hand, typically exhibit intense fluorescence, and when incorporated within the pores of mesoporous materials, might represent systems with wide utility, given their robust character and high processibility in different dispersing media.

In recognition of the aforementioned prospect, our focus in this chapter is on optically excited luminescence of a composite system consisting of an aggregated cyanine dye, specifically TTBC, (see Fig. 3-1) occluded within mesoporous aluminosiliceous MCM-41. The luminescence results from coherent emission from the excitonic state derived from coupled, aligned monomeric species. Such a composite evinces enhanced emission with a shortened radiative lifetime and may have specific utility in such applications as the active element in a flat-panel display device, as the secondary emitter at a near-field optical microscope (NSOM) fiber tip, and as a monochromatic emitting component in coatings for identification of objects in robotic vision and search-and-rescue endeavors.

3.2 Experimental

Synthesis of modified Al containing MCM-41 Polycrystalline powders of the mesostructural aluminosilicate MCM-41 were prepared by using cetyltrimethylammonium bromide (CTAB) as the template.[29,30] Briefly, Na_2SiO_3 (Aldrich, ~27% SiO_2) solution and a calculated amount of $NaAlO_2$ (Alfa) solution

(Si/Al = 20) were added to CTAB (Aldrich) solution according to the molar composition ratio $5SiO_2$:$0.125Al_2O_3$:CTAB:$610H_2O$. The pH was lowered to 11 with 2 M H_2SO_4 and the mixture was stirred for more than 3 h at about 318 K. Then the temperature was raised to 373 K, and the reaction allowed for 72 h in a Teflon-lined autoclave. The resulting precipitate was filtered, washed thoroughly with distilled water, and calcined in air at 773 K to obtain the final product, MCM-41 (see discussions below of XRD patterns).

To stabilize the synthesized MCM-41 and allow monomeric TTBC incorporation as well as formation of aggregated TTBC from the occluded monomers, we found it necessary to modify its interior structure through use of a silylation reagent, (aminopropyl)triethoxysilane (APTES; $NH_2(CH_2)_3Si(C_2H_5O)_3$), thus linking oxygen atoms on the aluminosilicate surface and rigidifying the mesoporous framework, and satisfying guest-host intermolecular and/or electrostatic interactions as well. For our studies, the modified MCM-41 was prepared according to ref 31. Briefly, about 1.5 g of the calcined MCM-41 was mixed with a chloroform solution of APTES (100 ml, 0.2 M) and stirred overnight at room temperature. The precipitate was filtered and washed with chloroform and dichloromethane.

Various MCM-41/TTBC assemblies were obtained through mixing of the modified MCM-41 with TTBC monomer in different ratios. Upon basifying filtered residues containing various assemblies in a programmed way, thereby changing the pH of the microenvironment within the cavity of the aluminosilicate, conditions were attained where the J-aggregated TTBC were formed from occluded

monomers. Specifics of the chemical and spectroscopic techniques are provided below.

Formation of TTBC/MCM-41 composites A typical preparation of a TTBC/MCM-41 composite involved stirring a mixture of 300 mg of modified MCM-41, 4.5 mg TTBC, and 15 mL of distilled water for over 24 h at room temperature with the pH held at ca. 7.0 using 2 M NaOH. The solution was then centrifuged, and the transparent aqueous solution decanted. The residue was washed approximately three times with distilled water to remove TTBC monomers from the external surface, and then dried in air. The product was designated TTBC-M/MCM-41, where TTBC-M indicates that monomeric TTBC was encapsulated within the modified MCM-41; absorption and emission studies (see below, section III) have confirmed the presence of monomer under the above conditions.

The formation of occluded, aggregated TTBC involves adding 2 M NaOH to the solid residue above. An immediate color change of the residue occurred from light red to dark pink. Absorption spectra of the powdered residue (see below, section III) indicated the presence of occluded J-aggregated TTBC, here designated TTBC-A/MCM-41.

Instrumentation Absorption spectra were recorded using a Perkin-Elmer, Lambda 18, UV-vis-NIR spectrometer. Steady-state fluorescence spectra were acquired using a SPEX, Fluorolog-τ2 spectrofluorometer. The X-ray diffraction (XRD) instrument used was a Rigaku diffractometer using Cu $K_{\alpha 1}$ (0.154 nm) X-rays: typically run at a voltage of 40 kV and current of 30 mA.

3.3 Results and Discussion

XRD patterns of pristine calcined MCM-41, modified MCM-41, the monomer-incorporated composite (TTBC-M/MCM-41), and the aggregate-incorporated composite (TTBC-A/MCM-41) are shown in Fig. 3-2. Using Bragg's equation and comparison with reference studies,[32-34] the pore size of calcined MCM-41 was estimated to be ca. 33 Å. Additionally, we find, upon attachment of the (putative) monolayer of silylation product to the internal channels of the calcined MCM-41, that the pore size is narrowed to ca. 24 Å, which is sufficiently large to allow TTBC, of approximate dimensions ca. (8 ×17) $Å^2$, to be incorporated into the modified MCM-41.

The XRD patterns of TTBC-M/MCM-41 and TTBC-A/MCM-41 show strong (100) peaks, suggesting that framework stability is still maintained for the modified MCM-41 when either monomeric or aggregated TTBC is incorporated. What difference in relative intensities that occur is likely attributable to electrostatic interaction between positive-charged TTBC and the interior walls of the cage as well as with the aggregate's transverse dimension as it grows along the channel length of the aluminosilicate.

We found that monomeric TTBC could be occluded into either calcined or modified MCM-41. For this kind of aluminosilicate, because of the doping of Al, the cage surface is more likely negatively charged, which favors the interaction with the monomeric TTBC with a positive charge on the chromophore. However, upon formation of aggregated TTBC from monomers, the (100) peak intensity for the calcined MCM-41 loses significant intensity (not shown), indicating that the

framework was not sufficiently strong to allow aggregation, thus resulting in disintegration of the structure. Rigidification of the calcined MCM-41 was a prerequirement to allowing occluded aggregate formation. It was noted that direct encapsulation of aggregated TTBC into the modified MCM-41 channels was not possible, and the "ship-in-bottle" approach, as used in our study dealing with encapsulation of TSPP into MCM-41,[28] was used here also.

Diffuse reflectance (DR) UV-vis spectra of the samples designated TTBC-M/MCM-41 and TTBC-A/MCM-41 are shown in Fig. 3-3. Also included in this figure, for comparison purposes, are transmission UV-vis spectra of TTBC in methanol solution (where monomer exists) and in aqueous solution (at a pH concentration where aggregated TTBC forms). The prominent absorption band at 590 nm in part C of this figure is termed the J-band and is indicative of a "spread-deck-of-cards" alignment of the aggregate within the cylindrical channels of modified MCM-41, which gives the "head-to-tail" arrangement of transition dipole moments of the constituent monomers. We found that resonance excitation of Raman scattering at 590 nm results in resonantly enhanced low-frequency bands (below ca. 300 cm^{-1}) that we have shown to also be diagnostic for aggregate formation as well.[3,34]

Continuing with Fig. 3-3, it is observed that the occluded monomer exhibits a red shift for its absorption band (520 nm) if compared to the band of the solution monomeric species (514 nm). A blue shift is found for the encapsulated J-aggregate when compared to the solution aggregate, 580 and 592 nm, respectively. Such shifts can be rationalized in terms of intramolecular charge-transfer caused by

host-guest interaction, which is connected to steric effects associated with the pore structure within modified MCM-41. The formation of the occluded monomer is rationalized by the fact that at pH = 7, the surface amino groups are not protonated, which makes it possible for positively charged TTBC to experience a favorable interaction with the lone pair electrons, thus facilitating monomer incorporation. Compared to the solution monomer (part C), a broaden structure for the monomeric band (part D) is observed, which can be attributed to site specific adsorption of encapsulated TTBC; suggesting that the monomer is dispersed at various positions within the matrix and experience, as a result, a range of perturbations.

Fluorescence spectra for solution phase and composite systems were also acquired (see Fig. 3-4). Fluorescence measurements entailed front-surface illumination of the samples, using the aforementioned spectrofluorometer. Both solid samples and solution samples were excited with essentially the same cross section of radiation, however the granularity of the composite likely leads to fewer absorbing entities in the excitation region. Acquired with excitation at 490 nm as shown in parts A and B of Fig. 3-4, the emissions from monomeric TTBC in solution and the composite TTBC-M/MCM-41 possess almost identical Stokes shifts to their respective absorption bands, shown in Fig. 3-3. However, the width of the composite's emission band suggests a greater dephasing of excitonic energy than for the aggregate formed in homogeneous solution. By the same argument, the similarity between the fluorescence spectra of the aggregate in solution and in the composite (parts C and D, respectively; excited at 550 nm with peak positions at ca. 594 nm), both in terms of band positions and widths, can be interpreted as

indicating that upon formation of the aggregate, the molecules are coupled and realigned such that site-specific perturbations to the exciton absorption energy, line width, and possibly other properties are diminished. It is worthy to note that the actual intensity at the fluorescence peak for the encapsulated aggregate is, on an absolute scale, about a factor of 2 greater than that for the solution species. Also, for TTBC-A/MCM-41, upon excitation at 490 nm (part E of Fig. 3-4), the emission at ca. 590 nm is found to be significantly larger than monomer at ca. 537 nm, suggesting that a substantial fraction of the available monomers has been incorporated into the aggregated species.

3.4 Conclusion

The combination of XRD, UV-vis absorption and fluorescence measurements of TTBC in solution and post-formation addition to a MCM-41 aluminosilicate indicates that we are able to form both monomeric and aggregated TTBC occluded in the core. To facilitate formation of incorporated J-aggregated TTBC, surface silylation, using an alkoxysilane reagent, was performed to rigidify and functionalize the walls of the aluminosilicate. The composite consisting of J-aggregated TTBC and the modified MCM-41 represents a new nanomaterial which has new properties arise from exciton energies and dynamics that result from quantum confinement. On the basis of this and other studies from this laboratory, we conclude that the quantum confinement is associated with both the restricted growth region available to the spontaneously self-assembled molecular aggregate, which forms when TTBC monomers are exposed to a sufficiently basic microenvironment, and the intrinsic confinement (characterized in terms of a

coherence length[36,37]) of the exciton's movement among a subset of coherently responding molecules within the physical aggregate.

3.5 Bibliography

1. Akins, D. L.; Özcelik, S.; Zhu, H.-R.; Guo, C. *J. Phys. Chem. A* **1997**, *101*, 3251.
2. Özcelik, S.; Akins, D. L. *J. Phys. Chem. B* **1999**, *103*, 8926.
3. Akins, D. L. *J. Phys. Chem.* **1986**, *90*, 1530.
4. Akins, D. L. *J. Colloid Interface Sci.* **1982**, *90*, 373.
5. Li, X.; Gu, B.; Akins, D. L. *Chem. Phys. Lett.* **1984**, *105*, 263.
6. Gu, B.; Akins, D. L. *Chem. Phys. Lett.* **1985**, *113*, 558.
7. Akins, D. L.; Akpabli, C.; Li, X. *J. Phys. Chem.* **1989**, *93*, 1977.
8. Akins, D. L.; Macklin, J. W. *J. Phys. Chem.* **1989**, *93*, 5999.
9. Akins, D. L.; Macklin, J. W.; Parker, L.; Zhu, H.-R. *Chem. Phys. Lett.* **1990**, *169*, 564.
10. Akins, D. L.; Macklin, J. W.; Zhu, H.-R. *J. Phys. Chem.* **1990**, *95*, 793.
11. Akins, D. L.; Zhu, H.-R. *Langmuir* **1992**, *8*, 546.
12. Akins, D. L.; Macklin, J. W.; Zhu, H.-R. *J. Phys. Chem.* **1992**, *96*, 4515.
13. Akins, D. L.; Zhuang, Y. H.; Zhu, H.-R.; Li, J. Q. *J. Phys. Chem.* **1993**, *98*, 1068.
14. Akins, D. L. In *J-Aggregate*; Kobayashi, T., Ed.; World Scientific: Singapore, **1996**; pp 67-94.
15. Plyuto, Y.; Berquier, J.; Jacquiod, C.; Ricolleau, C. *Chem. Commun.* **1999**, 1653.
16. Wu, C.; Bein, T. *Science* **1994**, *264*, 1757.
17. Kageyama, K.; J. Tamazawa, J.; Aida, T. *Science* **1999**, *285*, 2113.

18. Moller, K.; Bein, T. *Chem. Mater.* **1998**, *10*, 2950.

19. Holland, B. T.; Walkup, C.; Stein, A. *J. Phys. Chem. B* **1998**, *102*, 4301.

20. Sung-Suh, H,; Luan, Z.; Kevan, L. *J. Phys. Chem. B* **1997**, *101*, 10455.

21. Stucky, G. D.; MacDougall, J. E. *Science* **1990**, *247*, 669.

22. Moller, K.; Bein, T. *Chem. Mater.* **1998**, *10*, 2950.

23. Feng, X.; Fryxell, G. E.; Wang, L. Q.; Kim, A. Y.; Liu, J.; Kemner, K. M. *Science* **1997**, *276*, 923.

24. Chakraborty, P. *J. Mater. Sci.* **1998**, *33*, 2235.

25. Yang, P.; Wirnsberger, G.; Huang, H. C.; Cordero, S. R.; McGehee, M. D.; Scott, B.; Deng, T.; Whitesides, G. M.; Chmelka, B. F.; Buratto, S. K.; Stucky, G. D. *Science* **2000**, *287*, 465.

26. Özcelik, S.; Akins, D. L. *Appl. Phys. Lett.* **1997**, *71*, 1.

27. Özcelik, S.; Akins, D. L. *Appl. Phys. Lett.* **1998**, *73*, 1949.

28. Xu, W.; Guo, H.; Akins, D. L. *J. Phys. Chem. B*, **2001**, *105*, 1543.

29. Kresge, C. T.; Leonowicz, M. E.; Roth, W. J.; Vartuli, J. C.; Beck, J. S. *Nature* **1992**, *359,* 710.

30. Beck, J. S.; Vartuli, J. C.; Roth, W. J.; Leonowicz, M. E.; Kresge, C. T.; Schmitt, K. D.; Chu, C. T.-W.; Olson, D. H.; Sheppard, E. W.; McCullen, B.; Higgins, J. B.; Schlenker, J. L. *J. Am. Chem. Soc.* **1992**, *114*, 10 834.

31. Liu, C.-J.; Li, S.-G.; Pang, W.-Q.; Che, C.-M. *Chem. Commun.*, **1997**, *65*, 78.

32. Mercier, L.; Pinnavaia, T. J. *Adv. Mater.* **1997**, *9,* 500.

33. Stucky, G. D.; Monnier, A.; Schuth, F.; Huo, Q.; Margolese, D.; Kumar, D.; Kridhnamurty, M.; Petroff, P.; Firouzi, A.; Janicke, M.; Chmelka, B. F. *Mol. Cryst. Liq. Cryst.* **1994**, *240*, 187.

34. Akins, D. L.; Zhu, H.-R.; Guo, C. *J. Phys. Chem.* **1996**, *100*, 5420.

35. Grad, J.; Hernandez, G.; Mukamel, S. *Phys. Rev. A* **1988**, *37*, 3835.

36. Spano, F. C.; Mukamel, S. *J. Chem. Phys.* **1989**, *91*, 683.

37. Spano, F. C.; Kuklinski, J. R.; Mukamel, S. *J. Chem. Phys.* **1991**, *94*, 7534.

38. Kubelka, P. *J. Opt. Soc. Am.* **1948**, *38*, 448.

3.6 Figure Captions

Fig. 3-1 Structure of 1,1',3,3'-tetraethyl-5,5',6,6'-tetrachlorobenzimidazolo-carbo -cyanine (TTBC) iodide.

Fig. 3-2 XRD patterns of (A) calcined MCM-41, (B) modified MCM-41, (C) TTBC-M/MCM-41 and (D) TTBC-A/MCM-41.

Fig. 3-3 UV-vis spectra of TTBC in various environments. (A) Homogeneous solution phase monomeric TTBC at 5 $\times 10^{-5}$ M and pH = 8.0 in methanol solvent (dashed line), (B) Monomeric TTBC encapsulated in MCM-41 that was modified by surface silylation using (aminopropyl)triethoxysilane (APTES). The composite is designated TTBC-M/MCM-41 (dot-dot-dashed line) and was formed from a aqueous suspension of the aluminosilicate and TTBC at a pH of ca. 7, (C) Solution phase aggregated TTBC formed from monomer concentration of 5 $\times 10^{-5}$ M at pH = 11.5 in aqueous solvent (dotted line) and (D) Aggregated TTBC encapsulated in MCM-41 that was modified by surface silylation using (aminopropyl)triethoxysilane, designation TTBC-A/MCM-41 (solid line). $F(R)$, the right-hand side label, refers to the so-called remission function (a linear function of the concentration of homogeneous absorbers) for diffuse reflection measurements and is calculated from $F(R) = (1 - R)^2/2R$. In this expression R is the diffuse reflectance, given by $R = J_0/I_0$; where I_0 is the incident intensity at the surface and J_0 is the intensity of the reflected light.

Fig. 3-4 Fluorescence spectra of TTBC: (A) 5×10^{-5} M monomeric TTBC at pH = 8.0 in methanol, excited at 490 nm (dashed line), (B) TTBC-M/MCM-41, excited at 490 nm (dot-dot-dashed line), (C) aggregated TTBC at 5×10^{-5} M and pH = 11.0 using water as solvent, excited at 550 nm (dotted line), (D) TTBC-A/MCM-41, excited at 550 nm (solid line) and (E) TTBC-A/MCM-41, excited at 490 nm (dash-dotted line).

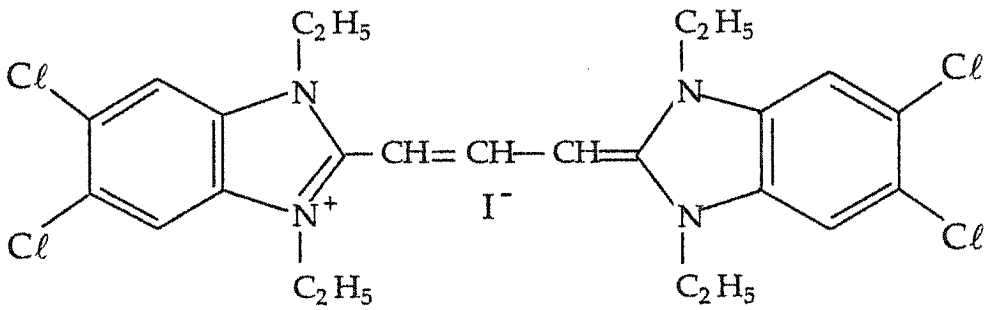

Fig. 3-1

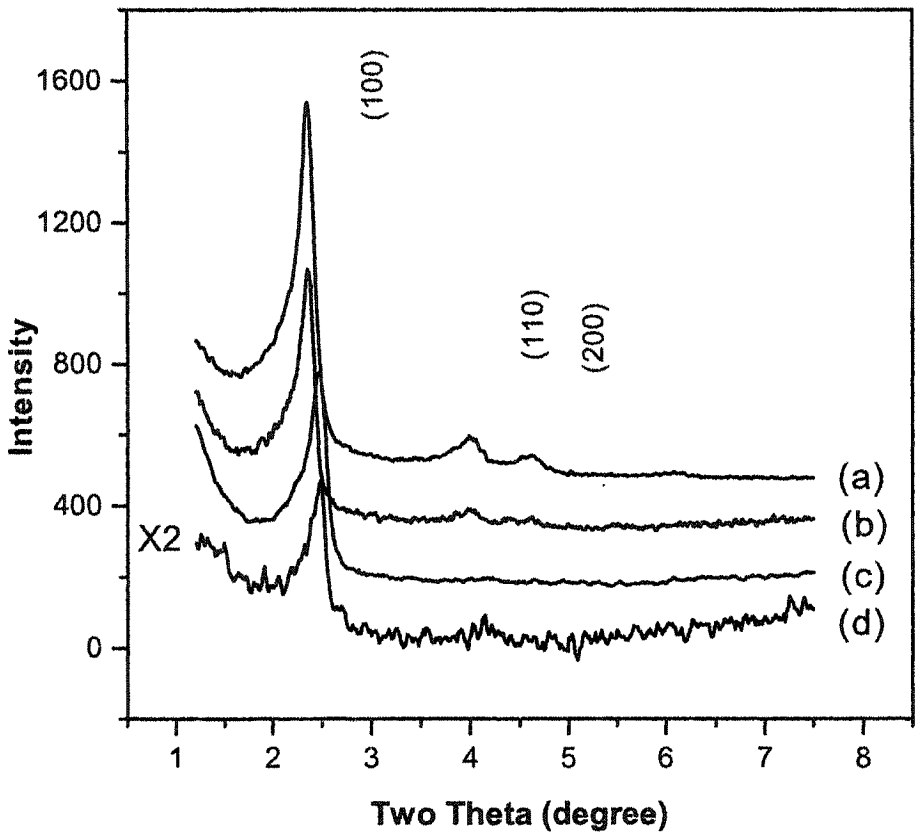

Fig. 3-2

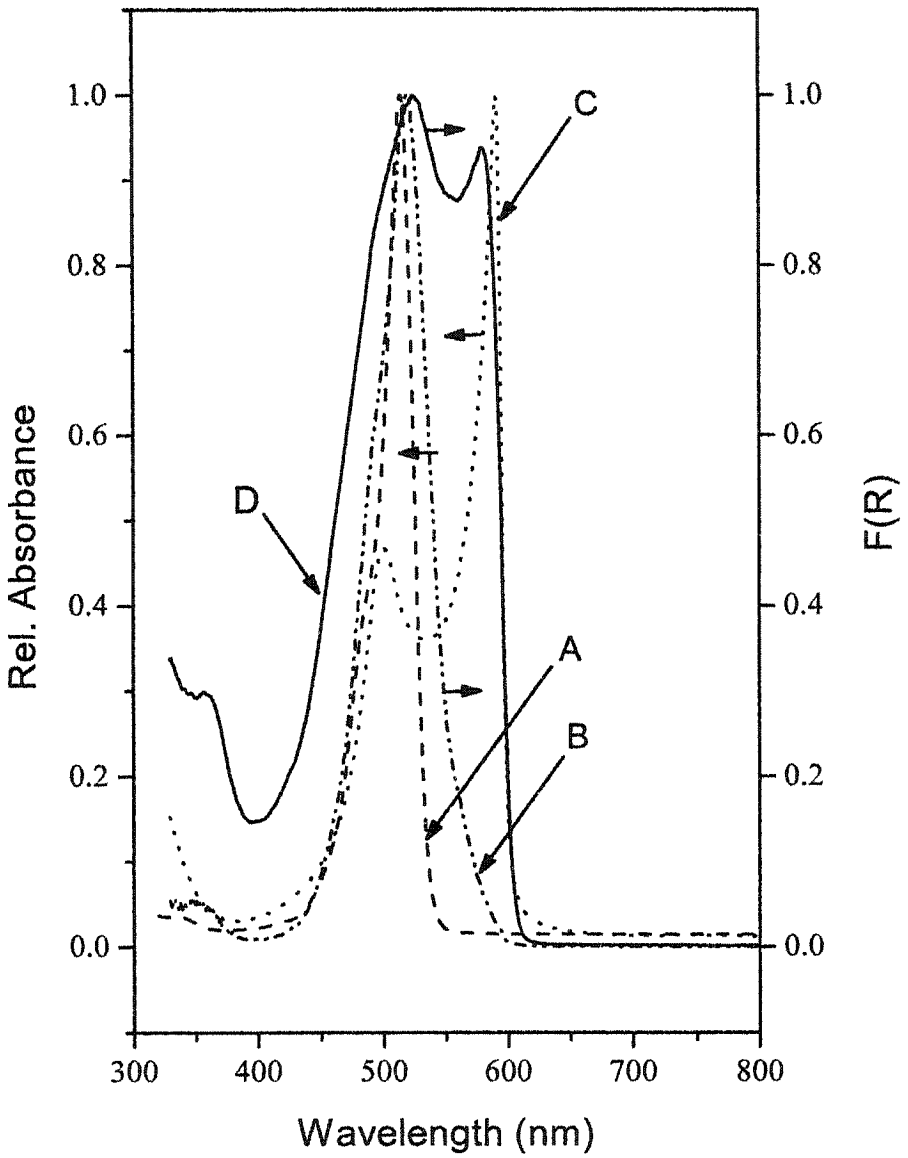

Fig. 3-3

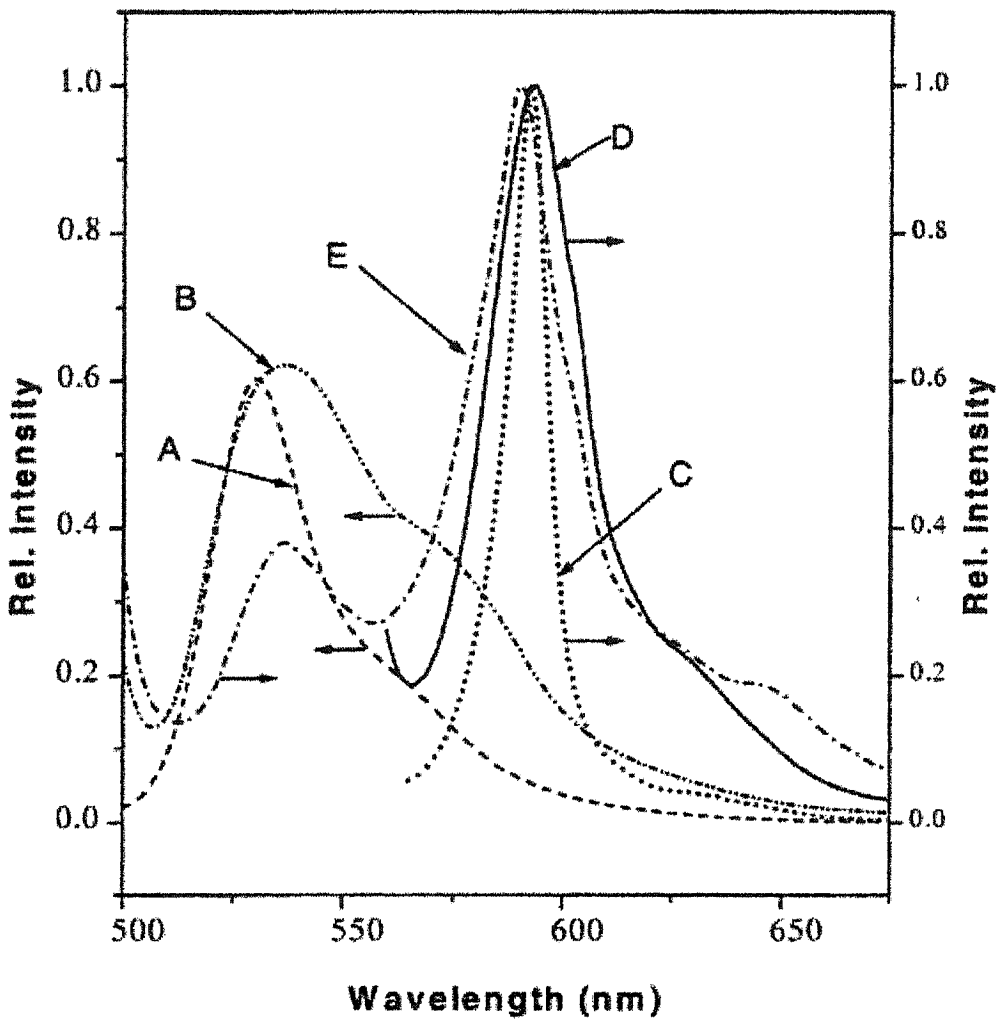

Fig. 3-4

Chapter 4: Spectroscopy and Dynamics of DCM Encapsulated in MCM-41 and Y zeolite Mesoporous Materials

4.1 Introduction

Photoinduced intramolecular charge transfer (ICT) is a fundamental mechanistic step in biological and chemical energy conversion processes [1-3], and is a phenomenon that might be exploited in photoelectronic devices.[4] Photoinduced charge separation is generally enhanced when the donor and acceptor groups are spatially positioned in such a fashion that the overlap of their orbital wavefunctions is limited, thus reducing the electronic coupling between the two groups. The resulting state when charge transfer is followed by a spatial reorientation of chromophoric units within a molecule is often referred to as a twisted intramolecular charge transfer (TICT) state, and its existence is often revealed through an exceptionally large Stokes-shifted absorption band that is formed in addition to the normal Stokes-shifted band associated with the lowest excited (LE) state. Upon photoexcitation, charge is transferred from the donor to the acceptor part of the molecule. However, the transfer of charge depends on the ability of the bond connecting the donor and acceptor moieties to twist, usually from an all-planar geometry to a 90-degree twisted geometry. The solvent polarity has been reported to be the most important parameter. In fact, it has been demonstrated that with an increase in the polarity of the media, the energy barrier for the TICT process decreases, causing an increase in the TICT (ICT) rate. Thus, the large class of TICT molecules have proven to be a fluorescence probe of solvation dynamics.

Fig. 4-1 is the summary of the above energy profile for the photodynamic behavior of DCM. There are two major relaxation channels for the optically excited electronic state: a radiative decay pathway with rate constant k_3, and a radiationless decay through internal conversion. The other channel consists of two processes: a barrier crossing on the excited-state potential surface to the TICT with forward k_1 and reverse k_2 rate constants; a fast radiative transition to the ground-state potential surface followed by a horizontal transition back to the original state, k_4. The relaxation scheme can be represented as a three-level system with the following rate equations describing time-dependent population changes for the energy levels

$$\frac{dN_0}{dt} = k_3 N_1 + k_4 N_2 \tag{1}$$

$$\frac{dN_1}{dt} = -(k_1 + k_3) N_1 + k_2 N_2 \tag{2}$$

$$\frac{dN_2}{dt} = k_1 N_1 - (k_2 + k_4) N_2 \tag{3}$$

where N_0, N_1, and N_2 are populations of the ground state, the initially populated level, and the TICT state, respectively.[5]

Molecules in which part of the molecule acts as an electron acceptor and another part acts as an electron donor may exhibit TICT states. A widely investigated molecule in regards to TICT transformations is 4-(dicyanomethylene)-2-methyl-6-(*p*-dimethylaminostyryl)-4H-pyran (DCM; see Fig. 4-2), a well known

laser dye that has high fluorescence efficiency and is photochemically stable.[6] It has been deduced that for DCM in its electronic excited state, an electron is intramolecularly transferred (i.e., an ICT occurs) from a so-called donor group to an acceptor group (both within the same molecule). In addition to ICT, DCM also undergoes either a twisting about an ethylenic double bond or about the bond joining the dimethylamino group and the aromatic ring, resulting in a twisted intramolecular charge-transfer (TICT) state.[7,8] As a result of interest in deciphering and quantifying rates for the several ultrafast processes that possibly exist, there have been several attempts to detail the primary photophysical processes for DCM. In general, it has been found that when polar solvents are used an emitting TICT state is formed, but the elementary steps coupled to the ICT process are extremely fast and not quantifiable even with ultrafast instrumentation.[9-12]

In recent years, however, temporal dynamics of DCM in many organized assemblies, such as protein, DNA, cyclodextrin, microemulsions, micelles, lipid vesicles, sol-gel matrix and polymer cavities, have been analyzed.[13-21] In these organized and constricting media, the local polarity and viscosity differ from solution values and substantially influence the photophysics and chemical dynamics of photoreactions. In general, it has been found that the rate of the TICT process is considerably reduced in constricted environments, by several orders of magnitude, and it is possible to observe dual emissions. However, dual emissions from DCM have not been observed because the TICT transformation occurs too rapidly even using ultrafast laser spectroscopy. We report in this chapter the room temperature

observation of dual emissions of DCM encapsulated in mesoporous MCM-41, resulting from reduced rates associated with photophysical relaxation processes.

4.2 Experimental Section

Synthesis of Modified Al Containing MCM-41

Polycrystalline powders of the mesostructural aluminosilicate MCM-41 were prepared by using cetyltrimethylammonium bromide (CTAB) as the template. Briefly, Na_2SiO_3 (Aldrich, ~27% SiO_2) solution and a calculated amount of $NaAlO_2$ (Alfa) solution were added to CTAB (Aldrich) solution according to the molar composition ratio $5SiO_2$:xAl_2O_3:CTAB:$610H_2O$ (x=0.03-0.125). The pH was lowered to 11 with 2 M H_2SO_4 and the mixture was stirred for more than 3 h at about 318 K. Then the temperature was raised to 373 K and the reaction allowed for 72 h in a Teflon-lined autoclave. The resulting precipitate was filtered, washed thoroughly with distilled water, and calcined in air at 773 K to obtain the final product, MCM-41 (see discussion below for XRD patterns).

To stabilize the synthesized MCM-41 and allow DCM incorporation, it is necessary to modify the interior structure of MCM-41 through use of a silylation reagent (specifically, (aminopropyl)triethoxysilane, i.e., NH_2-$(CH_2)_3$-Si-$(C_2H_5O)_3$ (APTES)), thus linking oxygen atoms on the aluminosilicate surface and rigidifying the mesoporous framework, as well as satisfying guest-host intermolecular and/or electrostatic interactions. For our studies, the modified MCM-41 was prepared according to reference 22. Briefly, about 1.5 g of the calcined MCM-41 was mixed with a chloroform solution of APTES (100 ml, 0.2 M) and stirred overnight at room

temperature. The precipitate was filtered and washed with chloroform and dichloromethane.

Formation of DCM/MCM-41 composites

DCM/MCM-41 composite was prepared by forming a mixture of 200 mg of modified MCM-41 with 10 ml of 1 g/l DCM in DMSO solution. The mixture was stirred at room temperature for more than 24 h, with the pH held at about 5.0 using 2 M H_2SO_4. The suspension was then centrifuged. The residue was washed at least twice with DMSO to remove the DCM from the external surface, then dried at about 80 °C.

Formation of DCM/Y-Zeolite composites

Zeolite NH_3-Y (Alfa) was used as received. The zeolite sample was initially calcined at 450 °C. DCM/zeolite composite was prepared by stirring a mixture of 200 mg Y-zeolite in 10 ml of 1g/l DCM in DMSO solution. The pH of the resultant suspension was near 5. The suspension was then stirred at room temperature for more than 24 h and then centrifuged. The residue was washed at least twice with DMSO to remove the DCM from the external surface and then dried at 80 °C.

Instrumentation

Absorption spectra were recorded using a Perkin-Elmer, Lambda 18, UV-Vis-NIR spectrometer. Steady-state fluorescence spectra were acquired using a SPEX Fluorolog-ι2 spectrofluorometer. The X-ray diffraction (XRD) instrument used was a Rigaku diffractometer using Cu $K_{\alpha 1}$ (0.154nm) X-rays: typically run at a

voltage of 40 kV and current of 30mA. For fluorescence decay measurements, the sample was excited at 480 nm with pulses of ca. 1 ps duration at a repetition rate of 1 KHz, provided by an all-solid state Spectra-Physics laser system, consisting of a Spectra Physics OPA 800 pumped by a Spitfire regenerative amplifier, which in turn was pumped by Merlin and seeded by a Millennia pumped Tsunami laser. The emission was detected by a Hamamatsu streak camera, model C4334. The temporal dynamics of the emission was analyzed using fluorescence lifetime software (HPD-TA 32) provided by Hamamatsu.

4.3 Results and Discussion

XRD patterns of pristine, uncalcined MCM-41, modified MCM-41, and the DCM/MCM-41 composite are shown in Fig. 4-3. Using Bragg's equation and comparison with reference studies, the pore size of uncalcined MCM-41 is estimated to be ca. 33 Å. Additionally, we find, upon attachment of the (putative) monolayer of silylation product to the internal channels of the calcined MCM-41, the peak at index (100) shifts to higher angle, with the pore size estimated to be ca. 25 Å. This latter size is sufficiently large to allow DCM, of approximate dimensions (8 × 16) $Å^2$, to be incorporated into the modified MCM-41. The XRD pattern of DCM/MCM-41 shows a strong (100) peak, suggesting framework stability is maintained for the modified MCM-41 when DCM is incorporated.

Y zeolite has a tridirectional geometry encompassing almost spherical cavities (of ca. 13 Å diameter) interconnected through four tetrahedrally arranged portals of ca. 8 Å diameter.[23] Although DCM can be accommodated inside the cavities of Y zeolite, the shape and the orientation of DCM are expected to be severely restricted.

Such confinement will tend to decrease photophysical relaxation rates for the dye in the host,[24] since ultrafast ICT reactions are facilitated when the configuration of the excited structure promotes an orbital interaction between donor and acceptor, as occurs, generally, when the excited state leads to molecular planarity.

Diffuse reflectance (DR) UV-vis spectra of DCM/MCM-41 and DCM/Y-zeolite samples are shown in Fig. 4-4. Also included in this figure, for comparison, is the transmission UV-vis spectrum of DCM in highly polar DMSO solution. For DCM/MCM-41 composites with different Si/Al ratio, the absorption spectrum does not change much. For the DCM/MCM-41 composite, DCM exhibits a broad absorption spectrum that is suggestive that at least three peaks exists (located at 365, 411 and 472 nm) instead of a single peak at 480 nm found for the dye dissolved in DMSO. The broad absorption is attributed to "site specific effects",[25] resulting from ground state DCM molecules being distributed within the channels of MCM-41 and experiencing, as a result, a range of perturbations. The interactions that are most likely of major influence in determining the blue shifted, broad absorption structure derive from the molecular resonance structures of DCM (see Fig. 4-2), where one finds that a greater density of electrons is expected to occur at the cyano group, and this charge is expected to result in stronger interactions between the cyano groups and the interior wall of the modified MCM-41, helping to anchor DCM within the pore, moreover, the positive charge on the dimethylamino group would be expected to result in neighboring DCM molecules in the cavity repelling one another, favoring a twisted structural character for DCM, which would militate ICT processes again. The diffuse reflectance spectrum of Y zeolite

(in Fig. 4-4), on the other hand, reveals only a small amount of blue-shifting (from the absorption maximum in DMSO) and a minor change in band width. We attribute this to the spatial dimensions of the Y zeolite supercages, which allow only a single DCM molecule to be encapsulated, resulting in an absence of a "site specific effect." Additionally, the small blue-shift that is evidenced can be attributed to the presence of twisted single DCM molecules within the supercages.

Also, fluorescence spectra for solution phase and composite samples were acquired with the all-solid state Spectra Physics picosecond laser and the Hamamatsu streak camera systems described earlier. We studied the polarity effect of the MCM-41 environment by changing the Si/Al ratio, which is shown in Fig. 4-5. By increasing the Si/Al ratio, the polarity of MCM-41 is decreased, thus the emission bands blue shift. Also with the decrease of the polarity of the cavity environment, a new band at around 555nm becomes obvious, which suggests the polarity as well as the restricted space of MCM-41 tunes the active energy between the LE state and the TICT state. When Si/Al ratio gets to 83, the larger active energy level of DCM from LE state to TICT state dramatically slows the ICT process so that results in the appearance of dual emission at that ratio.

Fig. 4-6 presents our principal fluorescence findings for the DCM system. As shown, for excitation using 480 nm radiation, the composite system DCM/MCM-41 shows an emission that possesses peaks at 555 and 585 nm (c), while the DCM/Y-zeolite composite evinces one band with peak position almost coincident with the 585 nm peak of DCM/MCM-41 (b). We assign this latter peak to emission from an emitting TICT state for the following reasons. Firstly, it is well known that the

photophysics of trapped molecules in matrices may depend on several parameters, and for the system examined here, the spatial constriction of the cavity would be expected to result in motional restriction for excited DCM guest molecules, which would trigger fast internal conversion relaxation processes and impart some ICT character to the resultant state for DCM in both MCM-41 and Y zeolite. Secondly, environmental polarity can dramatically affect optical properties of a confined dye, and an increase in polarity often leads to the formation of a red shifted TICT excited state and a resulting thermally driven enhanced TICT emission.[17,26-28,31] For our system, the polarity of MCM-41 lies between those of dichloromethane and 2-propanol, while Y-zeolite has a greater polarity than acetonitrile.[28,29] These relative values indicate that the polarity of Y-zeolite is greater than that of MCM-41, which rationalizes the red shift in the emission that is shown in Fig. 4-6 when the host changes from MCM-41 to Y-zeolite. Moreover, DMSO has a greater polarity than both of the solid hosts, and, accordingly, the red shift is even larger in this solvent. It is also to be noted, for comparison with the literature, that MCM-41 has a greater polarity than n-heptane, which has been used in ICT studies involving DCM,[16] and it is not unreasonable that the emission intensity of DCM might be higher for our system involving MCM-41 (given the greater environmental polarity) than that observed for the n-heptane system.

As regards the difference between the shapes of the emission from the MCM-41 and Y-zeolite systems, it is to be noted that the Y zeolite cavity is significantly more polar than that of MCM-41,[28,29] resulting in a lower activation energy between the LE and ICT states than expected in the case of MCM-41.

Consequently, a faster ICT process for the Y-zeolite composite may result in a decrease in the number of emitting states—in the present case to a single emission as compared to what happens for MCM-41 (see Fig. 4-6, spectrum c). Hence, the emission band at 585 nm is attributed to the emission from the excited ICT state resulting from relaxation of the initial formed LE state, while the emission band at 555 nm is attributable to a transition from the locally excited (LE) state.

Fluorescence spectra of the DCM/MCM-41 composite at three excitation wavelengths were acquired. The aim in this case was to determine whether the broad absorption spectrum in Fig. 4-7 pertains to absorption by the same species, albeit distributed amongst different sites within MCM-41. Fig. 4-7 shows spectra resulting from excitation at 360, 440, and 480 nm that fall near three peak absorption regions evidenced in Fig. 4-4. The resulting emissions are all quite similar, and are suggestive of the existence of two overlapping emission bands (see below). Hence, we can conclude that the emissions derive from a common species. For DCM in Y-zeolite and dissolved in DMSO, we also acquired emission spectra using different excitation wavelengths. In both cases, only one emission band occurred.

Fluorescence decay curves, using 480 and 514 nm excitations, were also measured for DCM in various environments, as shown in Fig. 4-9 for 480 nm exciting radiation. For DCM in DMSO, the emission decay in Fig. 4-9 fits a single exponential function with time constant of 2.0 ± 0.1 ns, where the ± error was assessed by changing the spectral window used by the Hamamatsu streak-camera software? in selecting and fitting data to exponential decays? and determining the

ranges of the calculated decays that results from varying the spectral window; this same approach was used for all indicated error assignments. For DCM in Y zeolite, the decay also is monoexponential, but of shorter lifetime, 1.3 ± 0.1 ns. The shortening of the lifetime for the DCM/Y-zeolite system, of course, can be attributed to interactions of DCM and Y-zeolite, which open nonradiative deactivation channels for decay. In particular, as a result of ionic bonding at the internal surface, energy transfer between the DCM molecules and Y-zeolite can occur, which introduces an additional pathway for depopulating the ICT state;[30] also electronic confinement, which leads to mixing of the HOMO and LUMO, can occur, with resultant enhanced nonradiative relaxations rates.[31] The emission decay for DCM in MCM-41 (see Fig. 4-9), while being shortened, however appears biexponential, independent of whether the fluorescence dynamics is monitored at 555 or 585 nm. The biexponential character is attributed to the capturing of photons from the overlapping wings of the two unresolved bands. Hence, both bands, as expected, have essentially the same values for the two relaxation times, although with possibly different amplitude factors. For the 555 nm peak the fast component is found to have a decay lifetime (Fig. 4-9) (percent contribution) of ca. 0.6 ns (57%), while the slower component has a decay lifetime (percent contribution) of ca. 1.8 ns (43%), resulting in an average decay time ($<\tau>=a_1\tau_1+a_2\tau_2$) of ca. 1.1 ns; the 585 nm peak gives the same decay constants and only slightly different amplitude factors. It is to be noted that the relative percentage for the contributions also are in agreement with the relative intensity of the two deconvoluted bands as found from the steady state emission spectrum (Fig.

4-8). Additionally, the use of 514 nm radiation to excite the fluorescence results in essentially the same decay constants and amplitude factors (Fig. 4-10).

We attribute the slow component to emission from a stabilized TICT state and the faster component to normal emission from the LE state. The relative amplitude of TICT emission is determined by the polarity of the MCM-41. Since the difference between the electronic energy levels of LE and TICT states is not large, the two states may co-exist in environments of moderate polarity.[32] For the DMSO solution system, where a twisting motion is expected to result in the formation of a TICT state, we observed only one decay component (with lifetime of 2.0 ± 0.1 ns), consistent with the existence of an ultrafast relaxation from the LE state to a TICT state.[10]

4.4 Conclusion

The present work shows that DCM can be successfully occluded within the pores of MCM-41 and Y-zeolite. From UV-Vis absorption and fluorescence measurements, DCM is found to exhibit different photophysics for MCM-41 and Y-zeolite mesoporous materials. For the composite consisting of DCM and MCM-41, ICT processes are found to be sufficiently reduced that a dual emission (attributed to emissions from the LE and ICT states) is observed. In this case, the optical decay leads to the assignment of lifetimes of 0.6 ± 0.1 ns for the LE state and 1.9 ± 0.1 ns for the TICT state. In the case of the Y-zeolite composite, only one emission (of decay lifetime 1.3 ± 0.1 ns) is found, which is rationalized in terms of the dimension of the supercages and the high polarity of the materials surface.

4.5 Bibliography

1 Verhoeven, J. W. *Pure Appl. Chem.* **1990**, *63*, 1585.

2 Khundkar, L. R.; Stiegman, A. E.; Perry, J. W. *J. Phys. Chem.* **1990**, *94*, 1224.

3 Lueck, H.; Windsor, M.; Rettig, W. *J. Phys. Chem.* **1990**, *94*, 4550.

4 Launay, J. P.; Sowinska, M.; Leydier, L.; Gourdon, A.; Amouyal, E.; Boillot, M. L.; Heisel F.; Miehé, J. A. *Chem. Phys. Lett.* **1989**, *160*, 89.

5 Spange, S.; Zimmermann, Y.; Graeser, A. *Chem. Mater.* **1999**, *11*, 3245.1.

6 Yoshizawa, M.; Kubo, M.; Kurosawa, M. *J. Lumin.* **2000**, *87-89*, 739.

7 Bingermann, D.; Ernsting, N. P. *J. Chem. Phys.* **1995**, *102*, 2691.

8 Moulik, S. P.; Pal, B. K. *Adv. Coll. Int. Sci.* **1998**, *78*, 99.

9 Easter, D. C.; Baronavski, A. P. *Chem. Phys. Lett.* **1993**, *201*, 153.

10 Van der Meulen, P.; Zhang, H.; Jonkman A. M.; Glasbeek, M. *J. Phys. Chem.* **1996**, *100*,5367.

11 Gustavsson, T.; Baldacchino, G.; Mialocq J. -C.; Pommeret, S. *Chem. Phys. Lett.* **1995**, *236*, 587.

12 Maciejewski, A.; Naskrecki, R.; Lorenc, M.; Ziolek, M.; Karolczak, J.; Kubicki, J.; Matysiak, M.; Szymanski, M. *J. Mol. Struct.* **2000**,*555*,1.

13 Pal, S. K.; Sukul, D.; Mandal, D.; Bhattacharyya, K. *J. Phys. Chem. B* **2000**, *104*, 4529.

14 Pal, S. K.; Sukul, D.; Mandal, D.; Sen, S.; Bhattacharyya, K. *Chem. Phys. Lett.* **2000**, *327*, 91.

15 Pal, S. K.; Mandal, D.; Sukul, D.; Sen, S.; Bhattacharyya, K. *J. Phys. Chem. B* **2001**, *105*, 1438.

16 Pal, S. K.; Sukul, D.; Mandal, D.; Sen, S.; Bhattacharyya, K. *Tetrahedron* **2000**, *56*, 6999.

17 Pal, S. K.; Mandal, D.; Sukul, D.; Bhattacharyya, K. *Chem. Phys. Lett.* **1999**, *312*, 178.

18 Martin, M. M.; Plaza, P.; Meyer, Y. H. *Chem. Phys.* **1995**, *192*, 367.

19 Zhou, Y.; Liu, Y.; Zhao, X.; Jiang, M. *J. Mol. Struct.* **2001**, *545*, 61.

20 Mandal, D.; Sen, S.; Bhattacharyya K.; Tahara, T. *Chem. Phys. Lett.* **2002** *359*, 77.

21 Wu, D.; Wang, L.; Liu, Y.; Ning, Y.; Zhao, J.; Liu, X.; Wu, S.; He, X.; Lin, J.; Wang, L.; Ma, D.; Wang, D.; Jing, X.; Wang, F. *Synth. Metals.* **2000**, *111-112*, 563.

22 Liu, C. J.; Li, S. G.; Pang, W. Q.; Che, C. M. *Chem. Commun.* **1997**, *65*, 78.

23 Galletero, M. S.; García, H.; Bourdelande, J. L. *Chem. Phys. Lett.* **2003**, *370*, 829.

24 Fayed, T. A.; Organero, J. A; Garcia-Ochoa, I.; Tormo, L.; Douhal, A. *Chem. Phys. Lett.* **2002**, *364*, 108.

25 (a) Xu, W.; Guo, H.; Akins, D. L. *J. Phys. Chem. B* **2001**, *105*, 1543; (b) Xu, W.; Guo, H.; Akins, D. L. *J. Phys. Chem. B* **2001**, *105*, 7686.

26 Wery, E. In *Effects of Molecular Environment on flourescence and Phosphorescence*; Marcel Dekker, Ed.; New York, **1990**.

27 Sarkar, N.; Das, K.; Nararyan Nath, D.; Bhattacharyya, K. *Langmuir* **1994** *10*, 326.

28 Datta, A.; Mandal D.; Kumar Pal, S.; Bhattacharyya, K. *J. Phys. Chem. B.* **1997**, *101*, 10221.

29 Kim, Y.; Lee, B. I.; Yoon, M. *Chem. Phys. Lett.* **1998**, *286*, 466.

30 Gu, G.; Ong P. P.; Li, Q. *J. Phys. D: Appl. Phys.* **1999**, *32*, 2287.

31 Márquez, F.; Garcia, H.; Palomares, E.; Fernández, L.; Corma, A *J. Am. Chem. Soc.* **2000**, *122*, 6520.

32 Yang, J.; He, Q.; Lin, H.; Fan, J.; Bai, F. *Macromol. Rapid Commun.* **2001**, *22*, 1152.

33 Kubelka, P. *J. Opt. Soc. Am.* **1948**, *38*, 448.

4.6 Figure Captions:

Fig. 4-1 Schematic energy profile for the photodynamic behavior of DCM.

Fig. 4-2 The resonance structures of DCM.

Fig. 4-3 XRD patterns of pristine (a) uncalcined MCM-41, (b) modified MCM-41 and (c) the DCM/MCM-41 composite.

Fig. 4-4 UV-vis spectrum of (a) 5×10^{-5} M DCM dissolved in DMSO; Diffuse UV-vis spectrum of (b) DCM/ MCM-41 and (c) DCM/Y-zeolite. $F(R)$, the label on the right-hand side, refers to the so-called remission function (a linear function of the concentration of homogeneous absorbers) for diffuse reflection measurements and is calculated from $F(R) = (1 - R)^2/2R$. In this expression R is the diffuse reflectance, given by $R = J_0/I_0$, where I_0 is the incident intensity at the surface and J_0 is the intensity of the reflected light .

Fig. 4-5 Fluorescence spectra of (a) DCM/ MCM-41 (Si/Al=20), (b) DCM/ MCM-41 (Si/Al=40) and (c) DCM/ MCM-41 (Si/Al=83).

Fig. 4-6 Fluorescence spectra of (a) 5×10^{-5} M DCM dissolved in DMSO, (b) DCM/ MCM-41 and (c) DCM/Y-zeolite.

Fig. 4-7 Fluorescence of DCM/MCM-41 composite, using a SPEX Fluorolog-τ2 spectrofluorometer. Excitation wavelength (a) 360 nm, (b) 440 nm, and (c) 480 nm.

Fig. 4-8 Deconvolution of the emission bands.

Fig. 4-9 Lifetime decay curves of (a) 5×10^{-5} M DCM dissolved in DMSO; (b) DCM/MCM-41 and (c) DCM/Y-zeolite.(λex=480nm)

Fig. 4-10 Lifetime decay curves of (a) 5×10^{-5} M DCM dissolved in DMSO; (b) DCM/MCM-41 and (c) DCM/Y-zeolite.(λex=514nm)

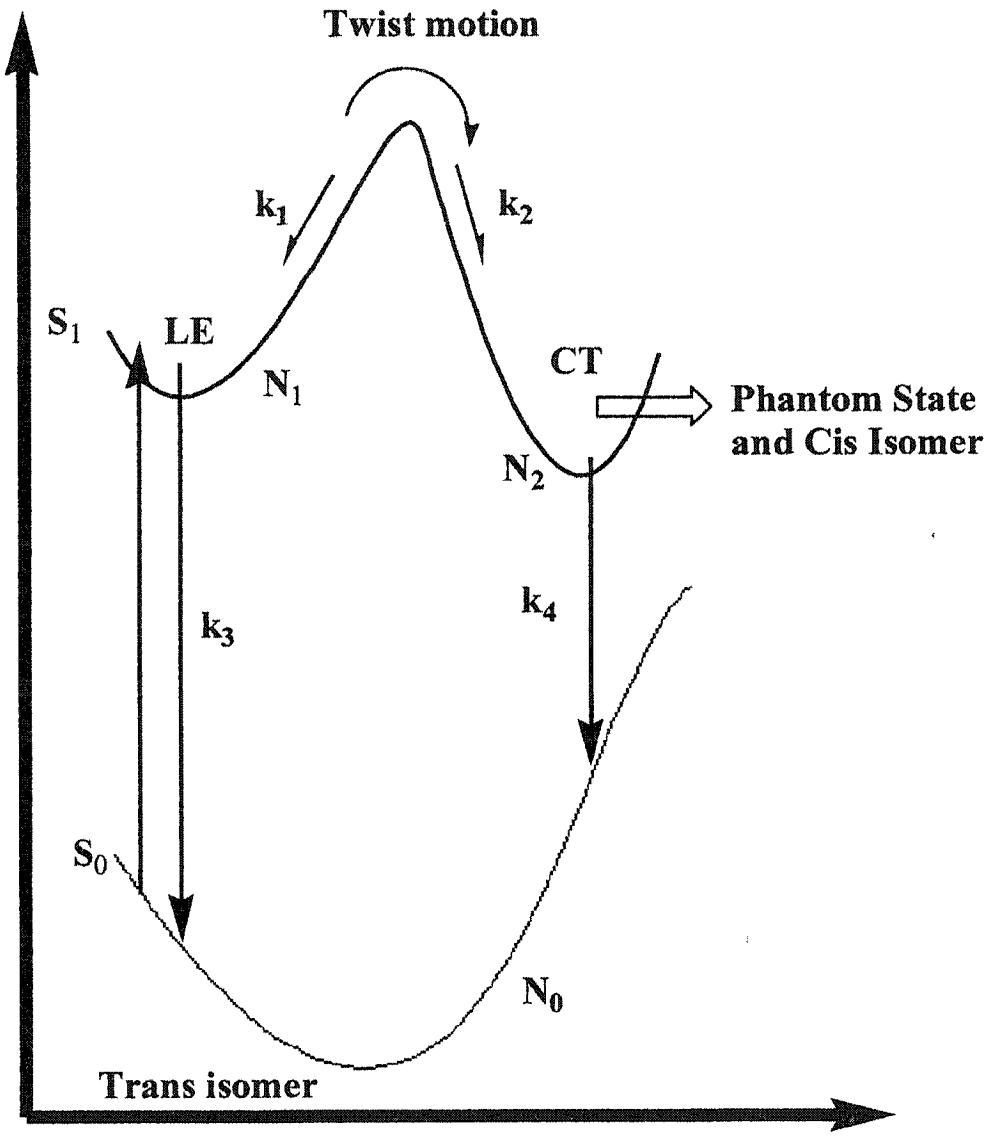

Fig. 4-1

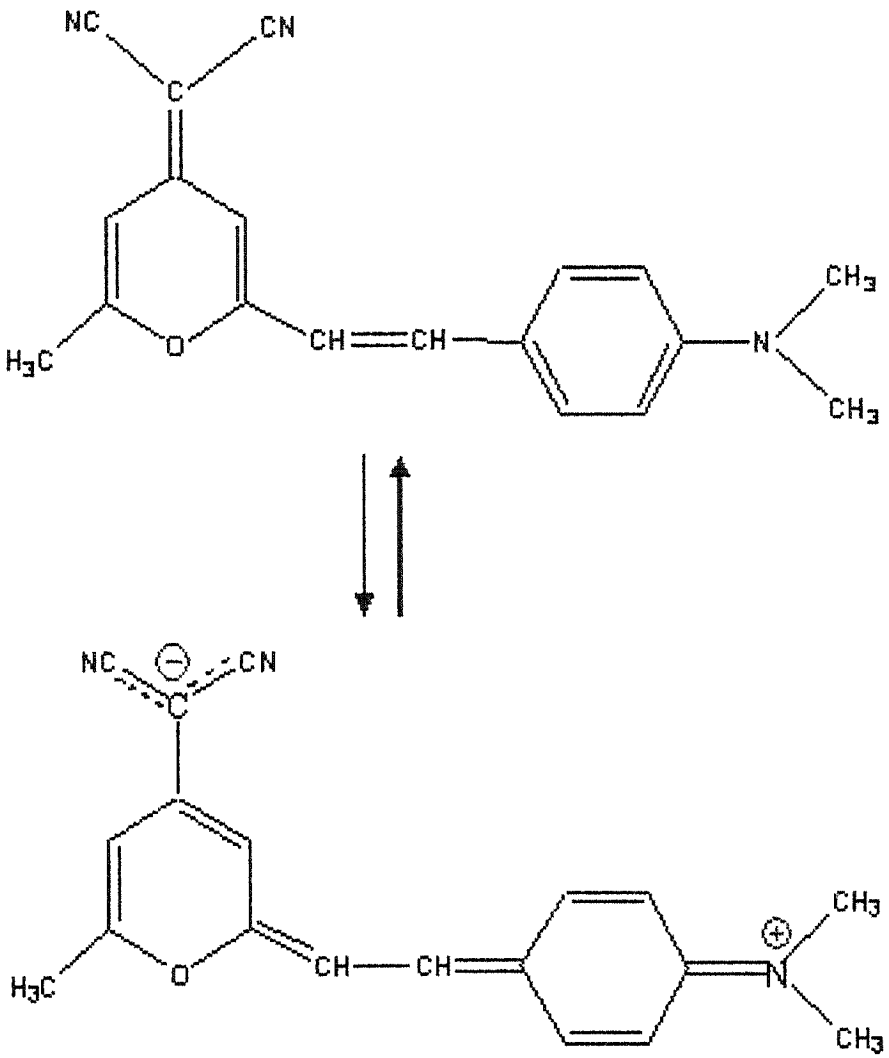

Fig. 4-2.

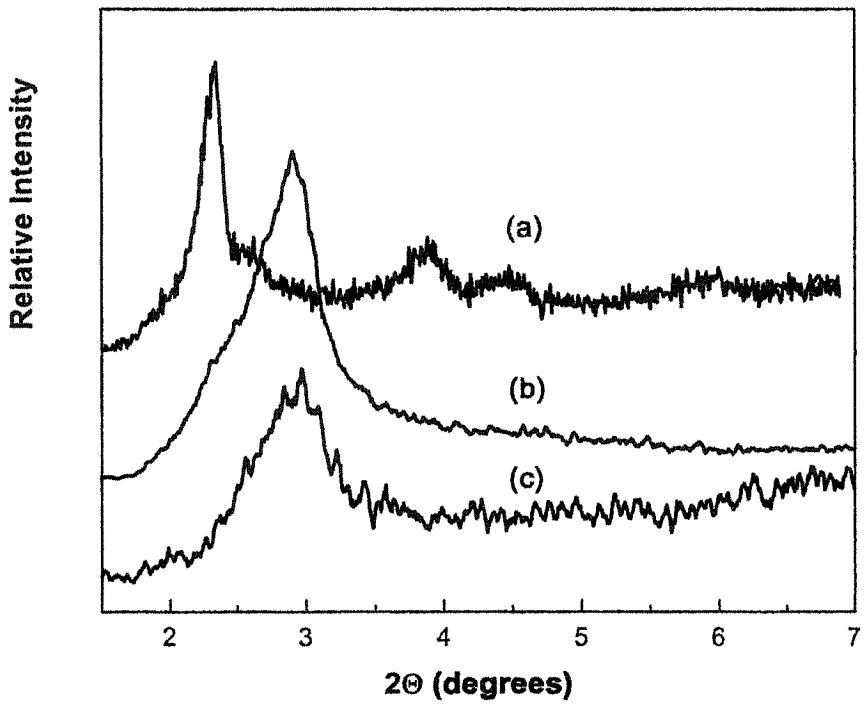

Fig .4-3

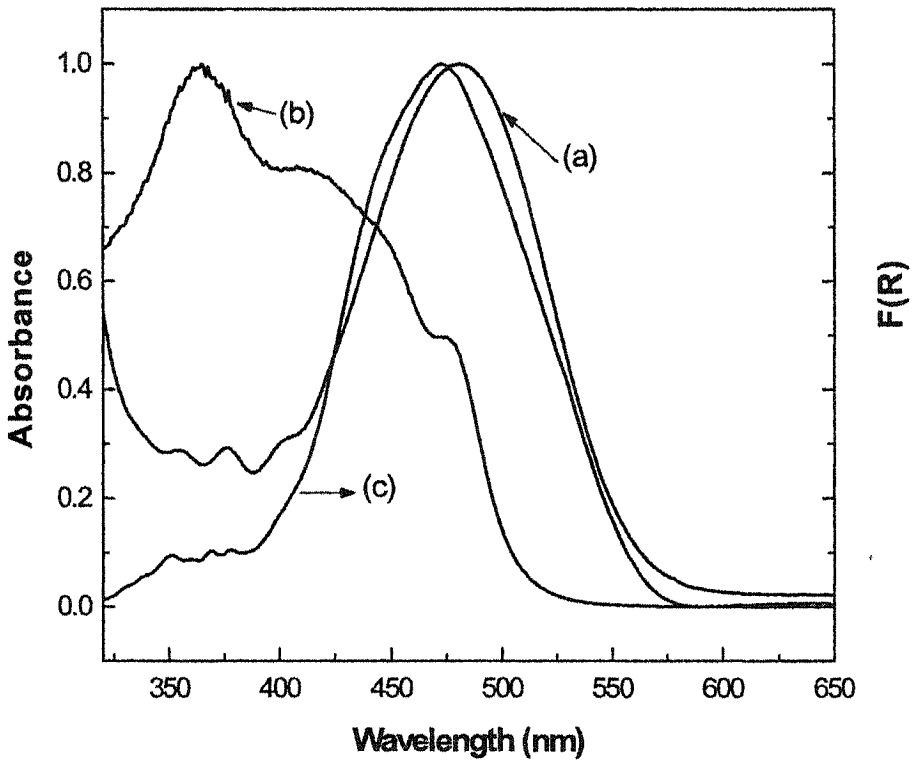

Fig. 4-4

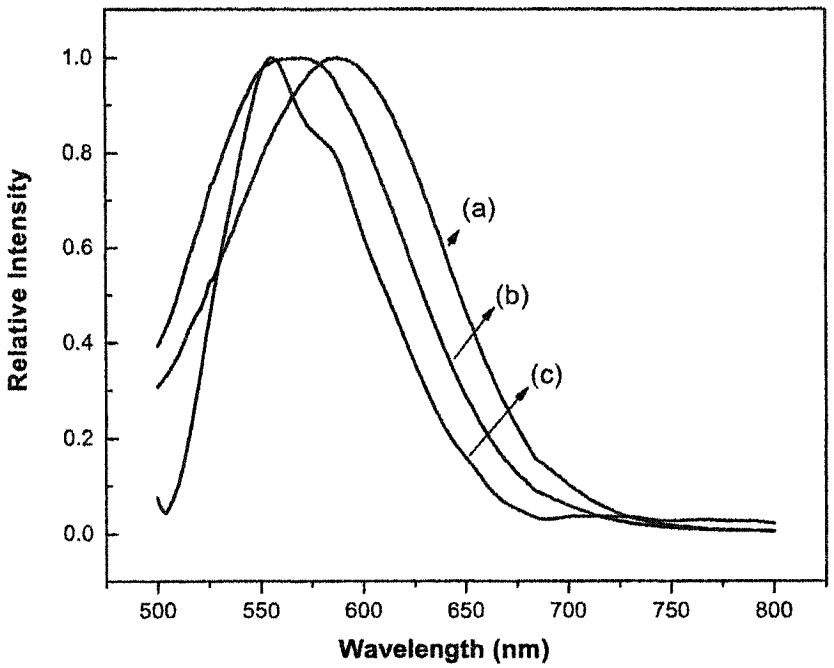

Fig. 4-5

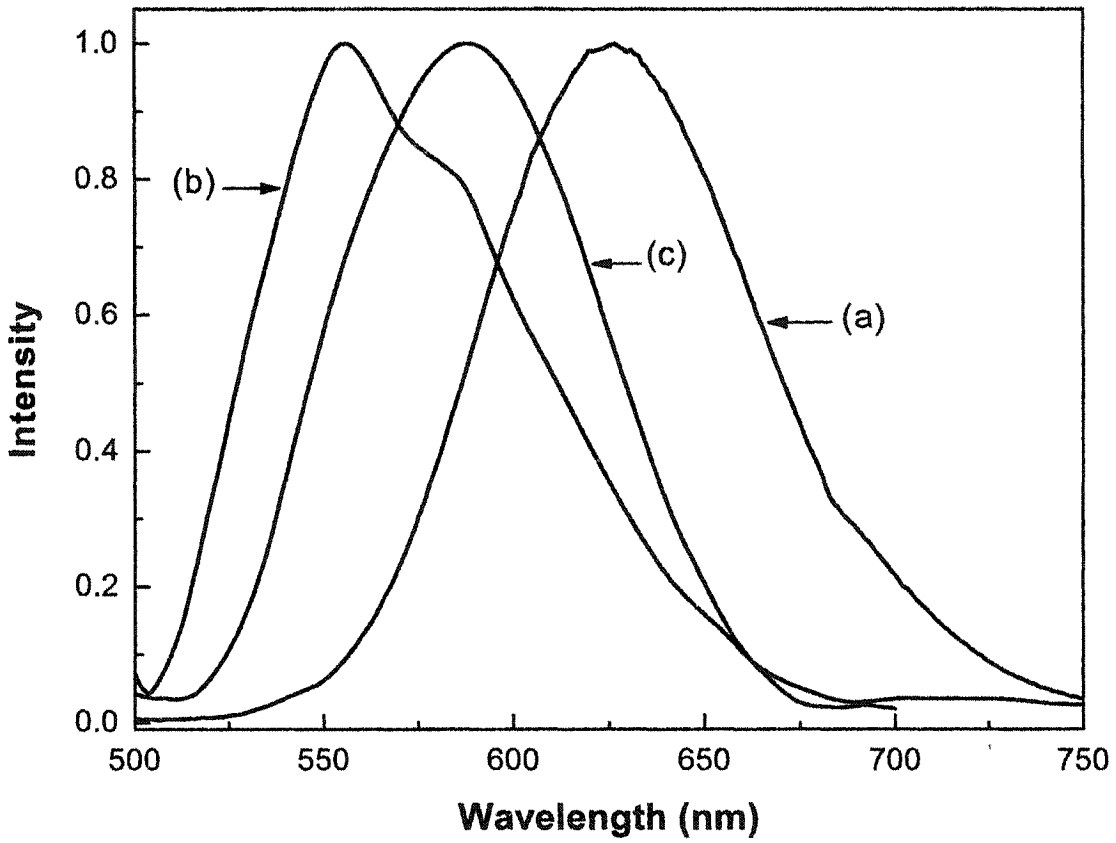

Fig. 4-6

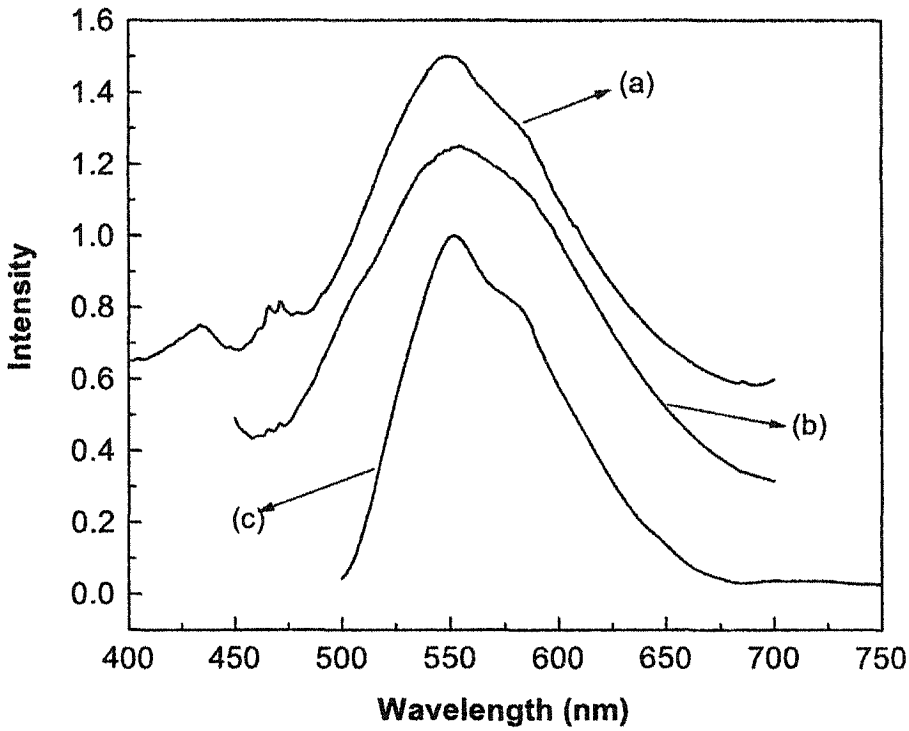

Fig. 4-7

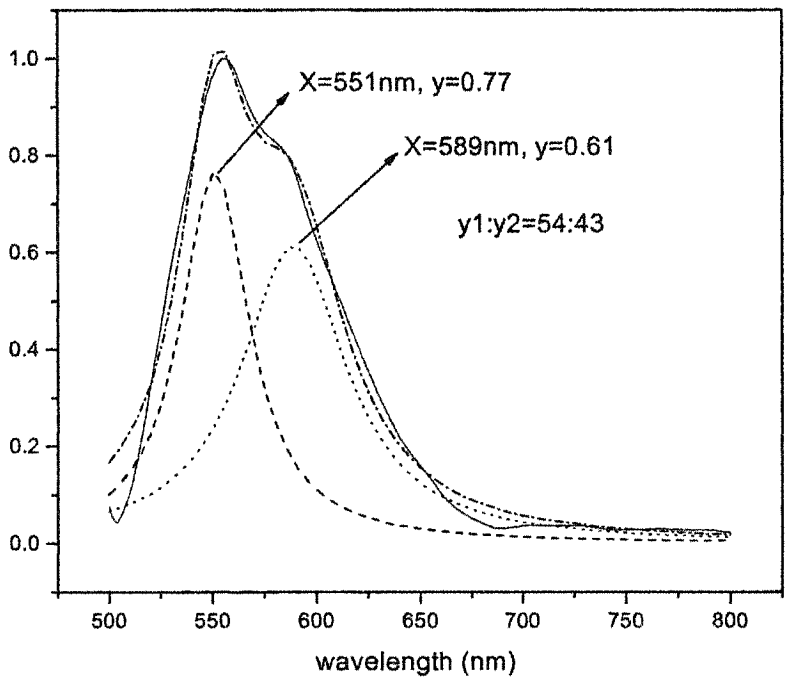

Fig. 4-8

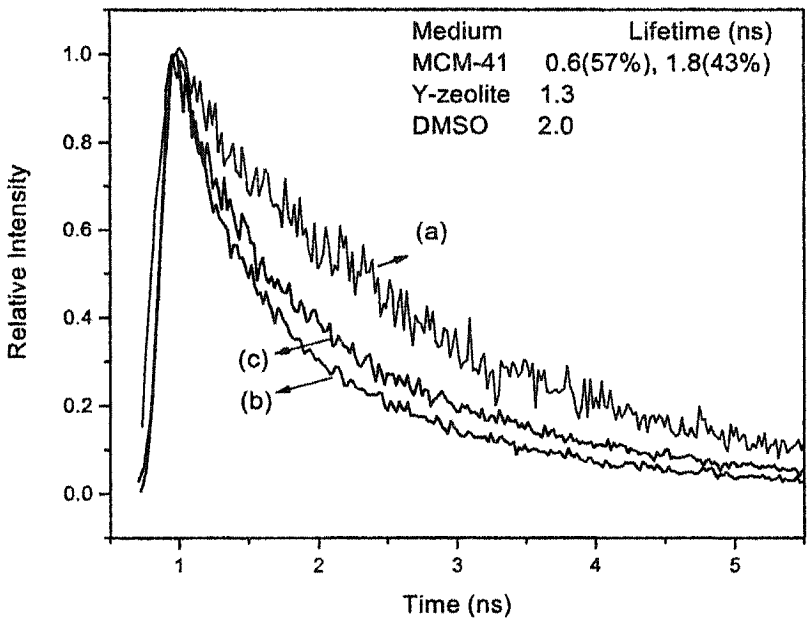

Fig. 4-9

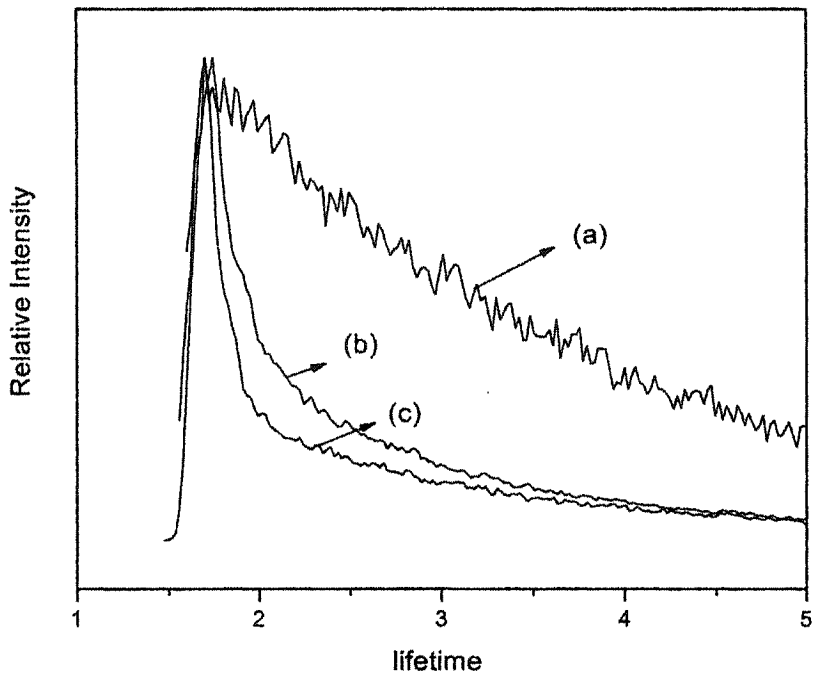

Fig. 4-10

Chapter 5: A New Microwave Absoption Material—Encapsulation of Fe_2O_3 within Mesoporous Materials

5.1 Introduction to Microwave and Magnetic Materials

5.1.1 Microwave and Magnetic Materials

Microwave is a kind of electromagnetic radiation with wavelengths that range from 1mm to 1m, which corresponds to a frequency ranged of 300 GHz to 30 GHz. It can be transmitted, absorbed or reflected depending on the type of materials the microwave interacts.[1] Microwave absorbing materials is the subject of intense research work due to the fact that it can widely used in the engineering of antennas, radar, stealth and electromagnetic shielding.

Magnetic materials can be a good absorber of microwave. Depending on whether the dipole moment of the material is permanent, magnetic materials can be classified into paramagnetic, diamagnetic or ferromagnetic. Diamagnetic materials with no unpaired electrons exhibit a weak induced magnetization in the opposite direction to an applied magnetic field. Atoms or ions containing unpaired electrons have a permanent magnetic moment. The moments are randomly oriented in the absence of an applied magnetic field or any ordering influence of neighboring moments (exchange interaction). When a magnetic field is applied on this kind of material, the magnetic moment is aligned. This kind of material is called paramagnetic. Ferromagnetism exhibit spontaneous magnetization caused by interactions between neighboring spins inside the materials. This term covers four magnetism phenomena: ferromagnetism, anti-ferromagnetism, ferrimagnetism,

canted antiferromagnetism, illustrated in Fig. 5-1. Above a critical temperature, Curie temperature in ferro/ferromagnetic material and Néel temperature in antiferromagnetic material, paramagnetic behaviour is observed.[2]

When a material is in a magnetic field,

$$B=\mu H=\mu_0(H+M) \quad (1)$$

where B is the flux density, H is the magnetic field, M is the magnetization, μ_0 is the permeability of free space. The efficiency of magnetodielectric absorbers is proportional to the loss of dielectric (e= e' -i e'') and magnetic permeabilities ($\mu=\mu'$-i μ'').

Fig. 5-2 is the scheme of the microwave absorption detection instrument. A microwave is generated by microwave generator (1) and adjusted to a certain frequency by frequency controller (2). The microwave goes through a sample holder (2), normally a slit, in which the microwave is transmitted, absorbed or reflected by the materials detected, then it is changed into voltage signal by voltage generators (4 and 5), and detected by the voltage meters parallel or perpendicular to the way microwave transmitted. The voltages are described in following:

$$V_{abs}=Vs-V_0 \quad (2)$$

where V_{abs} is the voltage change after the microwave through the sample. V_0 is the voltage without sample, Vs is the voltage measured after the microwave through the sample.

$$V_{abs}/V_0 \propto \text{tans} \quad (3)$$

where tans can be considered as the losses of the microwave through the materials.

$$\text{tans} \propto e''\mu'' \quad (4)$$

From the plot using frequency and V_{abs}/V_0 as the x and y axis respectively, the frequency range at which the microwave was absorbed can be roughly known.

Another way to characterize microwave absorption is to measure the Q factor by EPR instrument. Q indicates how efficiently the cavity stores microwave energy, which is defined as

$$Q = \frac{2\pi(\text{energy stored})}{\text{energy dissipated percycle}} \quad (5)$$

or it can be expressed as

$$Q=\nu_{cavity}/\Delta\nu_{cavity} \quad (6)$$

where ν_{cavity} is the resonance frequency of the cavity.[3]

5.1.2 Magnetic Ordering due to Dipolar Interaction[4]

As discussed before, ordering of neighboring moments (exchange interaction) which is mainly caused by dipolar interaction can influence the magnetic moment of the materials. The dipolar interaction may play an important role in the magnetic ordering in the case of ferromagnetism materials, which consist with a large intra-chain exchange coupling. This dipole-dipole interaction may be more remarkable

in the low dimensional magnetic materials, such as 0D, 1D and 2D objects. The energy associated with the dipolar interaction of the moment pair (μ_i, $\mu_j$can be expressed as :

$$E_{dip} = -\left\{\frac{\mu_0}{4\pi}\right\}\frac{\mu_i \cdot \mu_j}{r^3}\left[3\cos^2\theta - 1\right] \qquad (7)$$

where r is the length of the bond between the moments and θ is the angle between the moment orientation and the bonding vector between the moments. The dipole-dipole interaction can be realized in an assembly of 1D or 2D arrays of single-domain ferromagnetism dots or arrays of magnetic nanowires. A model system is magnetic spherical particles or nanowires arranged orderly in a suitable diamagnetic matrix, like ordered meosporous materials described in this chapter.

5.2 Background

Magnetic nanoparticles currently catch scientists' attention because their novel properties could have promising applications in technology. The properties of these materials depend strongly on the particle size, the particle-matrix interactions, and the degree of dispersion of the nanoparticles in the matrix.[5-6] Among those magnetic materials, Fe_2O_3 is a technologically important substance with wide utility in the semiconductor, pigment, magnetic storage, nonlinear optics, catalyst and gas-sensor arenas.[7-9] Enhanced interest, of late, has centered on nanostructural Fe_2O_3, whose electronic and optoelectronic properties—as a result of both quantum confinement and the greater influence of surface states—may differ substantially from those of the bulk material.[10]

Synthetic approaches for nanostructural Fe_2O_3 have been varied. Multifarious compositions and morphologies have been obtained by oxyhydrogen flame pyrolysis, electrochemical synthesis, sol-gel processes, chemical oxidation in micellar media or in polymer or mineral matrix.[11] Several years ago, research efforts aimed to encapsulate Fe_2O_3 within a new family of mesoporous materials, MCM-41 and SBA-15, which were developed by using liquid crystal templates. These silica-based mesoporous materials have a regular hexagonal array of uniform pores and the diameters of the channels can be controlled by using different chain length surfactants.[10] Because of their well-defined, well organized and one-dimensional structures, MCM-41 and SBA-15 are widely used in host matrices as chemically and spatially confined environments for the growth of inorganic clusters, particles and nanowires.[12-17] Ferric oxide incorporated in these kinds of matrces is a novel functional material with potential applications in "green" catalyst and semiconductor nanoparticles.[10, 16-17]

In this chapter, we describe how we adjusted the loading amount of ferric oxide within the mesoporous material MCM-41, and developed a new functional nanocomposite material, MCM-41 loaded with Fe_2O_3 at high level, whose functionality involves an enhanced absorption of microwave energy, even in the absence of an applied magnetic field.[18-20] Such a property was previously unobserved and has various potential applications in the fields of airplane, automotive, radar systems and stealth technology.

Also, we discuss the effect of the pore size of the mesoporous materials in dictating the position of the band edge for the occluded ferric oxide as well its microwave

absorption abilities. Three mesoporous hosts have been synthesized and characterized. The three hosts are labeled as C8-MCM-41, C16-MCM-41 and SBA-15; the first two corresponding to MCM-41, formed using surfactants with chain lengths involving 8 and 16 carbons atoms, respectively, the latter is the well known mesoporous material with hexagonally arranged hexagonal pores. EPR and Q factor measurements for the nanocomposites indicate that the three samples, when sufficiently loaded with ferric oxide exhibit significant microwave absorption strengths as well as microwave absorption at zero field strength. We have found that the microwave absorption ability increases with decrease of the pore size.

5.3 Experimental

Synthesis of mesoporous materials A series of silicate mesoporous materials with different pore size were prepared.

C8-MCM-41 was synthesized by using octyltrimethyl ammonium bromide as a template.[21] 5.3g of octyltrimethyl ammonium bromide (OTAB) was dissolved in 36.5 ml H_2O. 1.8 ml 5M NaOH solution was added to the OTAB solution. After stirring for 30 min, 5 ml tetramethyl orthosilicate (TMOS) was added. The mixture was stirred for one hour and then heated in a teflon-lined autoclave at 373 K for five days. The resultant precipitate was filtered and washed thoroughly with distilled water.

For C16-MCM-41, as a substitute, cetyltrimethyl ammonium bromide (CTAB) was chosen as a template. C16-MCM-41 was prepared according to the molar composition ratio SiO_2: 0.085 Na_2O: 0.16 CTAB: 63 H_2O.[22] 2.4 g CTAB was

dissolved in 40 ml distilled water, and mixed with 6.5 ml 1.1 M NaOH. After stirring for 30 min, 6.3 ml TMOS was added into the mixture solution. The mixture was stirred for one hour and then heated in a teflon-lined autoclave at 373 K for 24 hours. The precipitate was filtered and washed thoroughly with distilled water.

SBA-15 was prepared by using a triblock copolymer as the template. Specifically, 4 g of poly-(ethylene oxide)-poly (propylene oxide)-poly (ethylene oxide), i.e., $EO_{20}PO_{70}EO_{20}$, also referred to as Pluronic 123 (Aldrich), was mixed with 9 ml TEOS and 120 ml of 2 M HCl. The mixture was stirred for two hours, then allowed to react at 308 K for 20 hours, followed by heating the mixture at 373 K for two days. The product was then filtered and washed using distilled water.[23]

Modification of mesoporous materials[24-26] In a typical process, 1 g of as-prepared samples were modified by 2 ml $C_6H_5Si(OCH_3)_3$ in 25 ml chloroform solution for 6-12 h at room temperature. After extracting the organic template by using ethanol, the internal surface of the residual sample was modified by 5 ml 3-(2-aminoethylamino) propyltrimethoxy-silane in 50 ml toluene. The final modified mesoporous materials were filtered after 12 hours heating for the next step.

Formation of ferric oxide inside mesoporous materials 0.25 g as prepared modified mesoporous materials were mixed with certain amount of 0.1 M ethanolic $Fe(NO_3)_3 \cdot 9H_2O$. The mixtures were vigorously stirred and evaporated to remove ethanol at 80 °C. The dark brownish sample was then washed and heated at 180 °C for 24 h. The net effect is to enhance the amount of Fe_2O_3 formed within the channels of MCM-41.

Instruments Absorption spectra were recorded using a Perkin-Elmer, Lambda 18, UV-Vis-NIR spectrometer. The X-ray diffraction (XRD) instrument was a Rigaku diffractometer using Cu $K_{\alpha 1}$ (0.154 nm) X-rays: typically run at a voltage of 40 kV and current of 30 mA. Nitrogen isotherm was measured using an ASAP 2010 (Micromeritics) at 77K. Before the experiment the sample was heated at 573K and then outgassed at this temperature under a vacuum of 10-5 torr to constant pressure. The isotherm was used to calculate the surface area, pore size distribution and pore volume. The IR spectra were taken on a Thermo Nicolet Auntar 360 FTIR. The EPR spectra were recorded on a Bruker ESO380E spectrometer operating at X-band equipped with a HIP 5361 frequency counter. EPR spectra at room temperature were obtained under the following parameters: microwave power ~0.7 mW, modulation amplitude 10.45 G, modulation frequency 100 KHz, time constant 1.28 ms, sweep time up to 168 s, sweep width 7000 G and the X axis resolution 4 K. Transmission electron microscopy (TEM) images were acquired using powdered samples that were dry loaded onto Cu grids with holey carbon films, and utilized a Tecnai F 20 TEM operated at 200KV for bright field images; also the stability of MCM 41 samples was checked by both a JEOL 4000 EX microscope operated at 400 KV and a Topcon 002B microscope operated at 200KV. Transmission electron microscopy JEOL 100cx, acc. operated at 100 kV were used to observe the topography of the Fe_2O_3.

5.4 Results and Discussion

5.4.1 Concentration adjustation

Small angle XRD patterns of uncalcined, functionalized and Fe_2O_3 loaded C-16-MCM-41 are listed in Fig. 5-3. It indicates that after passivation, the external surface and internally modified structures of the molecular sieve materials maintained their organizations. However, after encapsulation of Fe_2O_3, the (100) peak intensities of the MCM-41 matrices decreased significantly, which is attributable to distortion of the mesoporous channels caused by the increasing loading of Fe_2O_3. From the longer angle XRD pattern of the composites with 39 wt% and 56 wt% Fe_2O_3 (Fig. 5-4 A and B), the guest inside MCM-41 can be identified as being α-Fe_2O_3. When the loading amount is lower than 12 wt%, composites do not support a large angle XRD spectrum, which is consistent with the idea that the nanoparticles formed are of extremely small diameters.[10]

Diffuse reflectance UV-vis of the composites are displayed in Fig. 5-5. For the 3 wt% Fe_2O_3 nanoparticle, the absorption spectrum mimics that of the ferric nitrate solution, and has an absorption near 350 nm. With the increase of the content of Fe_2O_3, red shift can be observed corresponding to the increment of the particle size. All of the composite samples exhibit blue shifted absorption bands caused by the quantum confinement effect when compared to the bulk Fe_2O_3 at ca. 560 nm.[17]

The Infrared spectra of functionalized C16-MCM-41 and C16-MCM-41/Fe_2O_3 are listed in Fig. 5-6. The IR spectra of C8-MCM-41, SBA-15 and their corresponding composites are similar to C16-MCM-41 and C16-MCM-41/Fe_2O_3, respectively. Comparing the curves before (a) and after loading Fe_2O_3 (b) (c), we

find that IR bands at 1630, 1378, 790, 560, and 460 cm^{-1}, are essentially unchanged upon occlusion of Fe_2O_3. These bands likely are associated with the external passivating agent and surface vibration of the mesoporous lattice. Some other bands are observed to shift, eg., 1074 cm^{-1} to 1090 cm^{-1}, attributable to the Si-O-Si vibration, and 976 cm^{-1} to 959 cm^{-1}, attributed to the Si-OH group. Still other bands exhibit lowered intensity upon formation of the composite, i.e., the 2854- and 2918-cm^{-1} bands; while other bands, at 1569, 1484, 1316, 1225, 698, and 666 cm^{-1} in Fig. 4-6A vanish. These latter bands are attributable to the stretching vibrations of C-H, Si-C, C-N, and the bending vibration for $-NH_2$. These IR measurements are interpreted as indicating that with the treatments discussed, Fe_2O_3 is incorporated inside the mesoporous channels of MCM-41, resulting in constricted motion associated with the limit space.

TEM images of the as-prepared composites with different Fe_2O_3 loading level are shown in Fig. 5-7. When the amount is around 3 wt%, (Fig. 5-7A) the structure of MCM-41 is maintained with a highly uniform hexagonal honeycomb structure and the pore size is around 4.2 nm. In the TEM image of the nanocomposite with 12 wt% Fe_2O_3 (Fig. 5-7B), the regular arrays are still kept regardless of observed parallel or perpendicular to the channels. We ascertain that most of Fe_2O_3 filled inside the channels of the matrix and some dispersed on the surface of MCM-41. When loading level rises to 39 wt%, it is already hard to observe the matrix from the direction along the channels due to the filling of Fe_2O_3 inside the channel so the image looks much darker (left corner of Fig. 5-7C). However, seen from perpendicular to the channel, the matrix is still maintained, which is in agreement

with XRD. For the highest load sample with 56 wt% Fe_2O_3, we find the matrix is destroyed, while the particle size is quite uniform. The particle with the matrix is around 4-5 nm. Considering the pore size of the MCM-41 array previously noted (Fig. 5-7 A), the particle size of Fe_2O_3 is successfully controlled.

To study the magnetic properties of the nanocomposites, EPR experiments are performed (Fig. 5-8). Very broad EPR signals of g value ~2.09 were observed for Fe_2O_3 nanocomposites, which is the resonance line coming from the Fe^{3+} coupling pair in the cage. Beside the g value of 2.09, some Fe_2O_3 nanocomposites exhibit a small but distinct signal at g ~4.3 corresponding either to a strongly distorted rhombic site located on the surface of the particle or to isolated iron (III) ions dispersed in the pore.[24, 28] It is interesting to note that for high loaded Fe_2O_3 composites (more than 12 wt%), the nanocomposites show strong absorption at magnetic field of ~99 G or even extrapolated to zero. This non-zero absorption is neither found in the functionalized silicate mesoporous material nor in ferric oxide prepared by the same route but without the use of the mesoporous matrix material. This indicates that the non-zero absorption likely results from some intrinsic level of alignment of the magnetic dipole moments within the pores. This intrinsic alignment most probably derives from strong dipole-dipole interactions associated with the restricted size of the pores and densly packing of a large quantity of Fe_2O_3 within pores.

This prediction is consistent with our observation of the temperature dependence of reciprocal of integrated intensity of EPR signals, as shown in Fig. 5-9. Generally the EPR signal amplitude is inversely proportional to the absolute

temperature according to Curie-Weiss's law, which was observed for Fe_2O_3 in MCM-41 matrices at low levels (3 wt% and 12 wt%). Therefore the samples consist of noninteraction or very weak interaction between nanoparticles. However, unusual temperature dependence was found in the high-loaded Fe_2O_3 nanocomposites (39 wt%, 56 wt%), in which the EPR signals were intensified with increasing measuring temperature. This suggests that there exists much stronger interparticle interaction among the magnetic nanoparticles. As a result, the EPR signal will increase with temperature as more and more particles orient their magnetic moments parallel to the field.[29-30]

To study the ability of microwave absorption for each sample, quality factor (Q) was measured at 99 G (Table 1). The smaller Q factor indicates the stronger microwave absorption abilities of the material. The Q factors of samples with different loading Fe_2O_3 are listed in Table 1. The Q factor for 56 wt% Fe_2O_3/MCM-41 is found to be 2500, nearly 30% lower than that of the blank tube. The trend is that Q factor increases as the loading amount decreases, indicating that as a result of strong dipole-dipole interaction, the magnetic moments for Fe_2O_3 nanostructures in the 56 wt% Fe_2O_3 nanocomposite are significantly aligned, resulting in enhanced microwave absorption ability.

For Fe_2O_3 at 39wt%, we measure the change of Q factors with different weight of C16-MCM-41/Fe_2O_3 composite, which is shown in Table 2. The Q factor decreases with the increase of the weight of the sample.

We have also undertaken preliminary investigation of the microwave spectrum on the sample with loading amount at 56wt% (Fig. 5-10) that gives rise to the

measured absorption. Generally, the efficiency of magnetodielectric absorbers is proportional to the loss of dielectric (e= e' -i e'') and magnetic permeabilities (μ=μ'-i μ''). And as discussed in equations (2)-(4), the maximum absorption frequency can be achieved by plotting the frequency and Vabs/V_0 as the x and y axis respectively. These latter studies have indicated that peak absorption occurs in the 30 GHz region, which is shown in Fig. 5-10. From Fig. 5-11, we see at that region, the energy lost by reflection is not much. With the microwave frequency increasing, the energy was dramatically reflected by the composite.

5.4.2 Pore Size Control

X-ray diffraction patterns for uncalcined, functionalized and Fe_2O_3 loaded for each C8-MCM-41, C16-MCM-41, and SBA-15 are shown in Fig. 5-12. Due to the low-molecular-weight surfactants are difficult to self-organize and hence, provide the least ordered materials, the sample C8-MCM-41, only one peak (100) is clearly visible and much wider than those of the other two samples. For the samples C16-MCM-41 and SBA-15, at least three peaks (100), (110) and (200) can be observed. All these indicate that C16-MCM-41 and SBA-15 have higher regular structures.

For all three samples, after functionalization, the structures of the mesoporous materials are still maintained. By using the Bragg Equation, the d spacing of the main peaks of each material was calculated. The d_{100} spacing of functionalized C8-MCM-41 is around 28 Å. For functionalized C16-MCM-41, the d_{100} spacing is close to 33 Å. Functionalized SBA-15 has the largest d_{100} spacing, which is 82 Å.

Determined by N_2 adsorption/desorption, shown in Fig. 5-13, after modification, the pore size of each material are 14 Å, 24 Å, and 78 Å respectively.

However, after encapsulation of Fe_2O_3 inside the channels, the (100) peak intensities of those three mesoporous materials decreased significantly, especially for C8-MCM-41 and C16-MCM-41, which resulted from the mesoporous channel distortion caused by the high-load of Fe_2O_3. Identified by the long angle X-ray diffraction (insets of Fig. 5-12), α phase Fe_2O_3 was observed in all those three composites. By comparing XRD patterns of Fe_2O_3 in different matrices, we found that when the pore size decreased from SBA-15 to C8-MCM-41, the peak at 35.5° becomes broader, which indicates that the average particle size of Fe_2O_3 in the matrix decreases with the reduction of the capacity of the mesoporous material. Thus the particle size can be controlled by the cavities of the silicate mesoporous materials by using the method.

Fig. 5-14 is the diffuse reflectance DRUV-vis spectra of the final products. The peak positions for Fe_2O_3 nanocomposites with C8-MCM-41, C16-MCM-41, and SBA-15 are at 341 nm, 392 nm and 403 nm, respectively. All of the composite samples exhibit blue shift when compared to the bulk Fe_2O_3, which has a absorption maxima at ca. 560 nm.[17] The large blue shifts referenced to the absorption maxima of bulk Fe_2O_3 are associated with the formation of nanodimensioned entities within the mesoporous materials. Because the growth of Fe_2O_3 is constrained inside the limited space, such confinement will tend to control particle size for the Fe_2O_3 in the host and affect the absorption spectra of the nanocomposites. With the decrease of the pore size from SBA-15 to C8-MCM-41,

the ferric oxide particles forming inside the channels are smaller, and thus a bigger blue shift can be observed from DR-UV-vis absorption spectra. The result is also consistent with the prediction from the XRD patterns. It is also worth noting that the SBA-15/Fe_2O_3 possesses a more obvious band at ca. 530 nm (shoulder) that likely indicates the presence of elongated structures.[27] This will also be discussed later in TEM results.

Transmission electron microscopy (TEM) provides further insight into the morphology and microstructural details of the Fe_2O_3 nanocomposites (Fig. 5-15). TEM images of Fe_2O_3 nanocomposites show that Fe_2O_3 particles are densely distributed and packed within the channels of mesoporous materials. As a result of the high loading level of Fe_2O_3 nanoparticles, various sites in the matrix are found to be distorted or even destroyed. These finding are consistent with our deductions based on the XRD patterns.

Because the channels of each mesoporous materials are distorted, it is hard to observe the matrix from a point perpendicular to the channel. After removal of the silica template of SBA-15 by hot NaOH solution, unsupported nanorodlike structure Fe_2O_3 with width ~12nm and length up to ~75 nm could be obtained, shown in Figure 5-14D, which is consistant with the prediction from UV-vis spectrum. We can conclude that the pore structures of the mesoporous materials can control the size and structure of iron oxide.

The HRTEM of those three samples are listed in Fig. 5-16. From Fig. 5-16, one can conclude that a large number of nanocrystals are present throughout the

sample. The average sizes of Fe_2O_3 particles with matrice are about 1-2 nm in C8-MCM-41, 4-5 nm in C16-MCM-41, and 8-9 nm in SBA-15, respectively. These relative values are consistent to the corresponded diameter of the channels of the mesoporous materials. Thus the particle size appears to be regulated by the mesoporous host pore diameter.

Digital diffractogram (fast Fourier transform, FFT) of the area is enclosed in the square marked in the image. The lattice spacing is measured, which is around 0.27 nm and the angles are 60°. Also from the EELS result, we see the O-k, Fe-L edge.

As regard to the magnetic behavior of the as-prepared Fe_2O_3 nanocomposites, we carried out electron paramagnetic resonance (EPR) studies. Fig. 5-17 is the first derivative EPR spectra of those three samples taken at room temperature. Very broad EPR signals with g values of ca. 2.1 were observed for the three Fe_2O_3 nanocomposites. Moreover, the composite in which Fe_2O_3 is encapsulated within SBA-15 exhibits a small but distinct signal at g ~4.3, corresponding either to a strongly distorted rhombic site located on the surface of the encapsulated particle or to isolated iron (III) ions dispersed within the pores.[24, 28] It is interesting to note that Fe_2O_3 encapsulated in these tubes has strong absorption at magnetic field of ~99 G or even extrapolated to zero. This non-zero absorption is neither found for the functionalized silicate mesoporous material nor for ferric oxide prepared by the same route but without the use of the mesoporous matrix material, indicating that the non-zero absorption likely results from some intrinsic level of alignment of the magnetic dipole moments within the pores. This intrinsic alignment most probably

derives from strong dipole-dipole interactions (which vary inversely with particle size and shape) associated with the restricted size of the pores and dense packing of a large quantity of Fe_2O_3 within pores. The result is that the magnetic moments of Fe_2O_3 are not randomly oriented even no significant external magnetic field is applied. Therefore, they may be partly aligned even in the absence of an external magnetic field, leading to positive susceptibility at zero applied fields. The origin of the zero-field absorption can be attributed to the high local field due to this alignment. This conclusion is consistent with our observation of an increase in the *g* value of the absorption (near $g \sim 2.1$) with decrease in temperature, shown in Fig. 5-18, an increase in the local field due to a higher order of alignment at a lower level of thermal randomization.

Generally, the EPR signal amplitude is inversely proportional to the absolute temperature, according to Curie's law, which was observed for Fe_2O_3 encapsulated in MCM-41 at a low level by using wet impregnation method.[11] Unusual temperature dependence was found for these three high-loaded Fe_2O_3 nanocomposites, as shown in Fig. 5-19, in which the EPR signals were intensified with the increasing measuring temperature. The contrary signal amplitude with the temperature among these samples can be contributed to the amount of Fe_2O_3 loaded in the channels. As the temperature increases, some of the immobilized Fe_2O_3 in the pore of C8-MCM-41, C16-MCM-41 and SBA-15 tend to move freely in the absence of an external magnetic field. As the external field is applied to the sample, because of the closed packed particles, the dipoles in the freed Fe_2O_3 will tend to align themselves parallel to the applied filed, resulting in increased EPR

signal amplitude at higher temperature. And in the lower temperature range, exchange interaction (antiferro) becomes more important, which decreases the intensity of the EPR signals. Therefore this opposite behavior can be attributed to the vast α-Fe_2O_3 nanoparticles within narrow channels.

To study the ability of microwave absorption for each sample, quality factor (Q) was measured at 99 G (Table 3). Q represents the efficiency of the cavity for storage of microwave energy. Upon comparing two materials, the one with the smaller Q factor generally absorbs microwave absorption more strongly. As shown in Table 3, the Q factors of Fe_2O_3 in the three composites are substantially lower than that for a blank tube, indicating that the Fe_2O_3 nanocomposites have strong microwave absorption capacities. We note that, based on Q factor, the composite Fe_2O_3/C8-MCM-41 has the strongest microwave absorption ability among the three samples. The Q factor for Fe_2O_3/C8-MCM-41 is found to be 1800, nearly 50% lower than that of the blank tube. The trend is that Q factor increases as the pore size decreases, indicating that as a result of strong dipole-dipole interaction, the magnetic moment for distributed sites within the Fe_2O_3 nanostructures within C8-MCM-41 are significantly aligned, resulting in enhanced microwave absorption ability.

5.4.3 Conclusion

The present work shows that Fe_2O_3 can be successfully occluded within the pores of the mesoporous materials C8-MCM-41, C16-MCM-41 and SBA-15, each having a one-dimensional structure, with size increasing in the order presented. Composite

samples were characterized by UV-vis, IR, TEM, EPR and X-ray diffraction. We ascertained that the pore sizes of the three mesoporous materials and the loading level significantly affect the spectral properties of encapsulated ferric oxide. From UV-vis absorption, ferric oxide is found to exhibit different blue-shifts relative to that for bulk ferric oxide; the lower level of the Fe_2O_3 and the smaller the pore size, the larger the blue shift observed. Most profoundly, EPR measurements indicate that for sufficient loading with Fe_2O_3, the composite material exhibits nonzero absorption at zero applied magnetic fields and has a substantial microwave absorption capability at moderate applied fields. The absorption ability, in fact, is found to increase decrease in pore size of the mesoporous material in which the Fe_2O_3 is formed.

5.5 Bibliography

1 Petrov, V. M.; Gagulin, V. V. *Inorganic Materials* **2001** *37*, 135.

2 Standley, K. J. In *Oxide Magnetic Materials*, Oxford, Clarendon Press, **1972**.

3 Boca Raton, Fla., In *EPR and Advanced EPR Studies of Biological Systems*; Dalton, L. R., Ed.; CRC- Press, **1985**.

4 Panissod P.; Drillon A. In *Magnetism: Molecules to Materials IV*; Miller, J. S., Drillon, M., Ed.; Wiley-VCH, **2002**.

5 Moreno, E. M.; Zayat, M.; Morales, M. P.; Serna, C. J.; Roig, A.; Levy, D. *Langmuir* **2002**, *18*, 4972.

6 Tannenbaum, R.; Reich, S.; Flenniken, C. L.; Goldberg, E. P. *Adv. Mater.* **2002**, *14*, 1402.

7 Huo, L.; Li, W.; Lu, L.; Cui, H.; Xi, S.; Wang, J.; Zhao, B.; Shen, Y.; Lu, Z. *Chem. Mater.* **2000**, *12*, 790.

8 Bourlinos, A.; Simopoulos, A.; Petridis, D.; Okumura, H.; Hadjipanayis, G. *Adv. Mater.* **2001**, *13*, 289.

9 Weckhuysen, B. M.; Wang, D.; Rosynek, M. P.; Lunsford, J. H. *Angew. Chem. Int. Ed. Engl.* **1997**, *36*, 2374.

10 Iwamoto, M.; Abe, T.; Tachibana, Y. *J. Mol. Cata A: Chemical.* **2000**, *155*, 143.

11 Pascal, C.; Pascal, J. L.; Favier, F.; Elidrissi Moubtassim, M. L.; Payen, C. *Chem. Mater.* **1999**, *11*, 141.

12 Xu, W.; Liao, Y.; Akins, D. L. *J. Phys. Chem. B* **2002**, *106*, 11127.

13 Tian, B.; Liu, X.; Yang, H.; Xie, S.; Yu, C.; Tu, B.; Zhao, D. *Adv. Mater.* **2003**, *15*, 1370.

14 Shi, J.-l.; Hua, Z.-l.; Zhang, L.-x. *J. Mater. Chem.* **2004**, *14,* 795.

15 MacLachlan, M. J.; Aroca, P.; Coombs, N.; Manners, I.; Ozin, G. A. *Adv. Mater.* **1998**, *10*, 144.

16 Abe,T.; Tachibana,Y.; Uemastu, T.; Iwamoto, M. *Chem. Commun.* **1995**, 1617.

17 Zhang, L.; Papaefthymiou, G. C.; Ying, J. Y. *J. Phys. Chem. B* **2001**, *105*, 7414.

18 Guo, H.; Xu,W.; Cui, M.; Yang, N. –L.; Akins, D. L. *Chem. Commun.* **2003**, 1432.

19 Guo, H.; Cui. M.; Zhang, X.; Xu, W.; Sharma, R.; Yang, N.-L.; Akins, D. L. (submitted).

20 Guo, H.; Zhang, X.; Chi, N.; Xu, W.; Sharma, R.; Yang, N.-L.; Akins, D. L. (to be submitted).

21 Choma, J.; Burakiewicz-Mortka, W.; Jaroniec, M. *Colloid Surface A* **2002**, *203*, 97.

22 Sayari, A.; Danumah, C.; Moudrakovski, I. L. *Chem. Mater.* **1995**, *7*, 813; Sayari, A.; Moudrakovski, I. L.; Danumah, C.; Ratcliffe, C. I.; Ripmeester, J. A.; Preston, K. F. *J. Phys. Chem.* **1995**, *99*, 16373.

23 Zhao, D.; Feng, J.; Huo, Q.; Melosh, N.; Fredrickson, G. H.; Chmelka, B. F.; Stucky, G. D. *Science* **1998**, *279*, 548.

24 Zhang, Z.; Dai, S.; Fan, X.; Blom, D. A.; Pennycook, S. J.; Wei, Y. *J. Phys. Chem. B* **2001**, *105*, 6755.

25 Bourlinos, A. B.; Simopoulos, A.; Boukos, N.; Petridis, D. *J. Phys. Chem. B* **2001**, *105*, 7432.

26 Diaz, J. F.; Balkus, K. J., Jr.; Bedioui, F.; Kurshev, V.; Kevan, L. *Chem. Mater.* **1997**, *9*, 61.

27 Jiao, F.; Yue, B.; Zhu, K.; Zhao, D.; He, H. *Chem. Lett.* **2003**, *32*, 770

28 Cannas, C.; Gatteschi, D.; Musinu, A.; Piccaluga, G.; Sangregorio, C. *J. Phys. Chem. B* **1998**, *102*, 7721.

29 Testa, A. M.; Foglia, S.; Suber, L.; Fiorani, D.; Casas, L.; Roig, A.; Molins, E.; Greneche, J. M.; Tejada, J. *J Appl. Phys.* **2001**, *90*.

30 Barco, E. d.; Asenjo, J.; Zhang, X. X.; Pieczynski, R.; Julia, A.; Tejada, J.; Ziolo, R. F. *Chem. Mater.* **2001**, *13*, 1487.

5.6 Figure Captions

Fig. 5-1 Exchange coupled spin structures and the net spontaneous magnetism.

Fig. 5-2 Scheme of microwave detection instrument: (1) microwave generator, (2) frequency adjustor, (3) sample holder, (4) Voltage generator for absorption detection, (5) Voltage meter for absorption detection, (6) Voltage generator for reflective detection and (7) Voltage meter for reflective detection.

Fig. 5-3 Small angle XRD of (A) uncalcined C16-MCM-41, (B) functionalized C16-MCM-41, (C) composite Fe_2O_3/MCM-41 with 3wt% Fe_2O_3, (D) composite Fe_2O_3/MCM-41 with 12wt% Fe_2O_3, (E) composite Fe_2O_3/MCM-41 with 39wt% Fe_2O_3 and (E) composite Fe_2O_3/MCM-41 with 56wt% Fe_2O_3.

Fig. 5-4 Longer angle XRD of (A) composite Fe_2O_3/MCM-41 with 39wt% Fe_2O_3 and (B) composite Fe_2O_3/MCM-41 with 56wt% Fe_2O_3.

Fig. 5-5 UV-Vis of (A) $Fe(NO_3)_3$ ethanolic solution, DRUV-Vis of (B) C16-MCM-41/Fe_2O_3 with 3wt% Fe_2O_3, (C) C16-MCM-41/Fe_2O_3 with 12wt% Fe_2O_3, (D) C16-MCM-41/Fe_2O_3 with 39wt% Fe_2O_3 and (E) C16-MCM-41/Fe_2O_3 with 56wt% Fe_2O_3,

Fig. 5-6 IR spectrum of (A) functionalized MCM-41, (B) MCM-41/Fe_2O_3 with 3wt% Fe_2O_3 and (C) MCM-41/Fe_2O_3 with 56wt% Fe_2O_3.

Fig. 5-7 TEM of (A) C16-MCM-41/Fe_2O_3 with 3wt% Fe_2O_3, (B) C16-MCM-41/Fe_2O_3 with 12wt% Fe_2O_3, inset is the TEM of perpendicular to the channel, (C) C16-MCM-41/Fe_2O_3 with 39wt% Fe_2O_3, inset is the

5.7 Table Captions

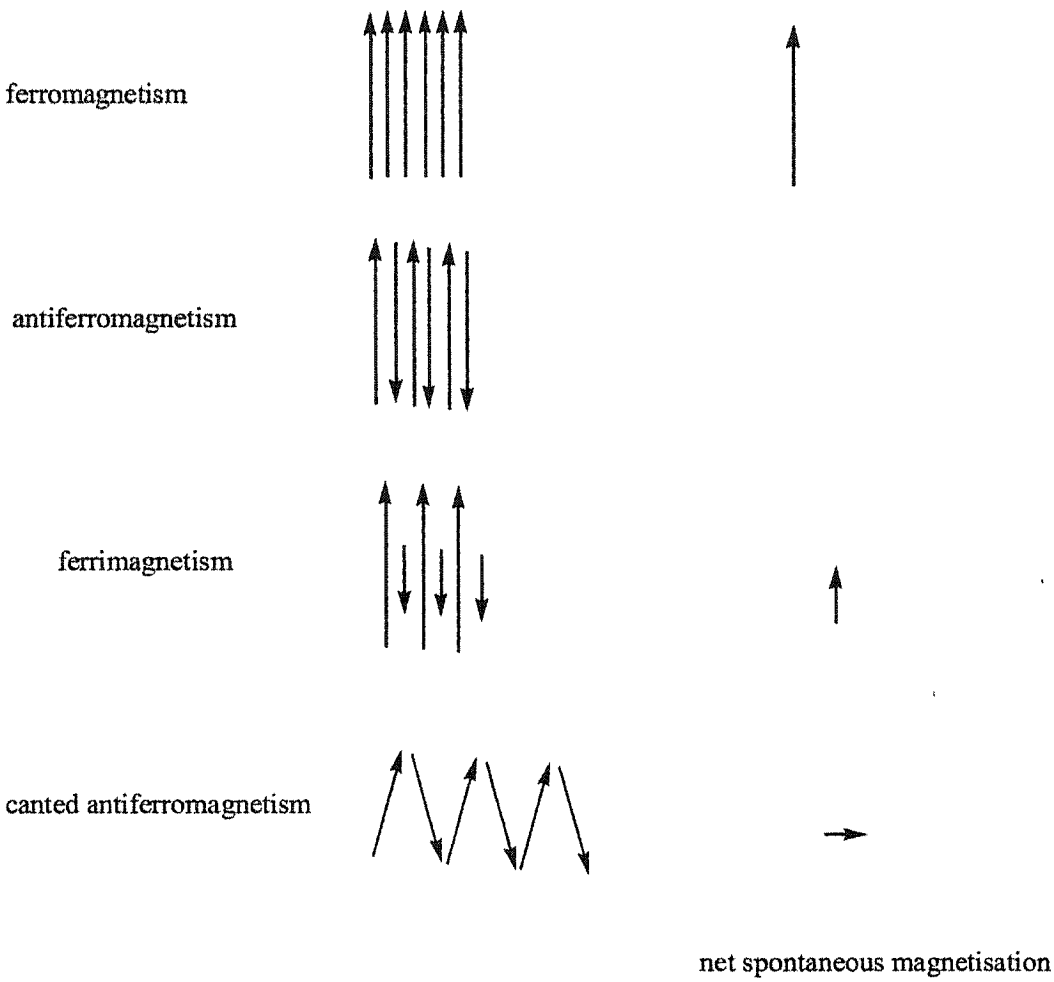

Fig. 5-1

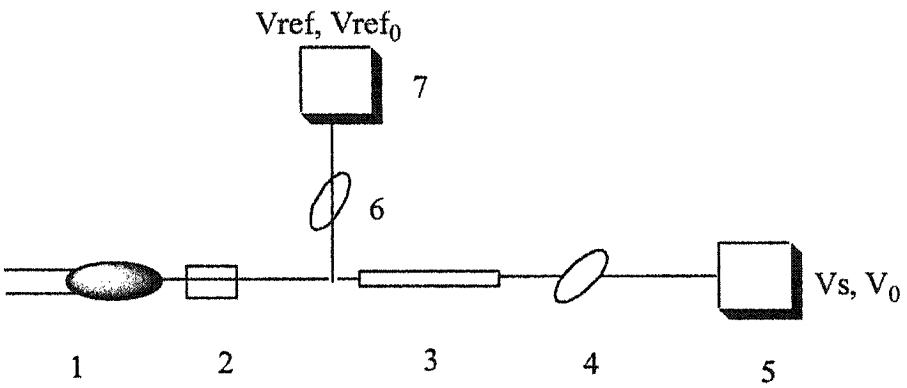

Fig. 5-2

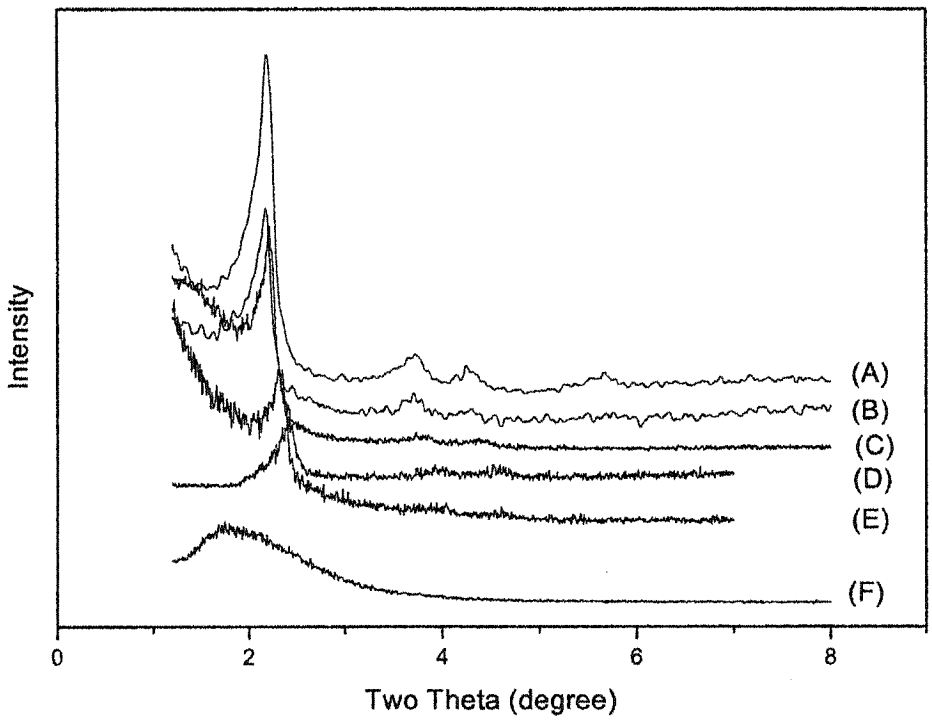

Fig. 5-3

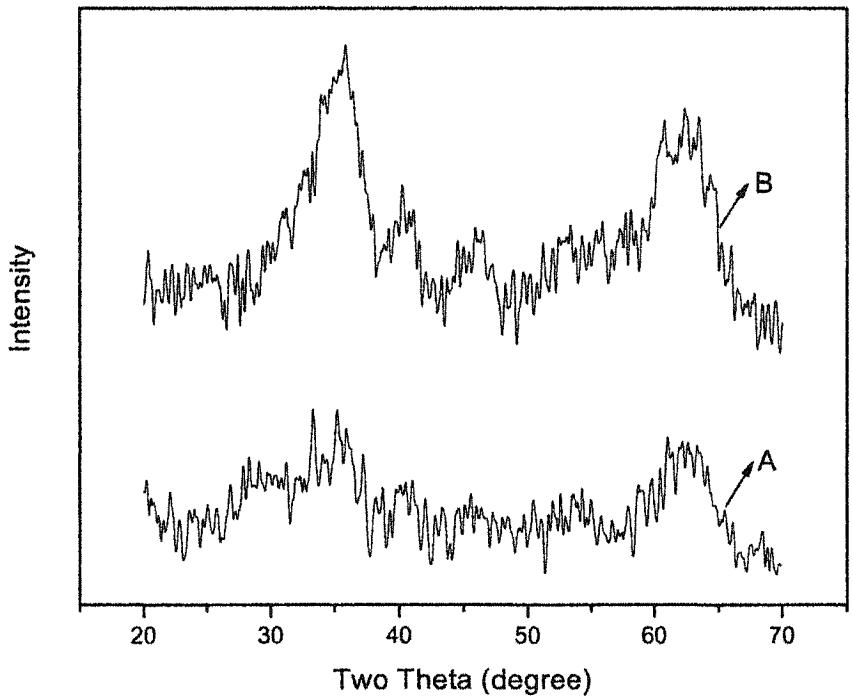

Fig. 5-4

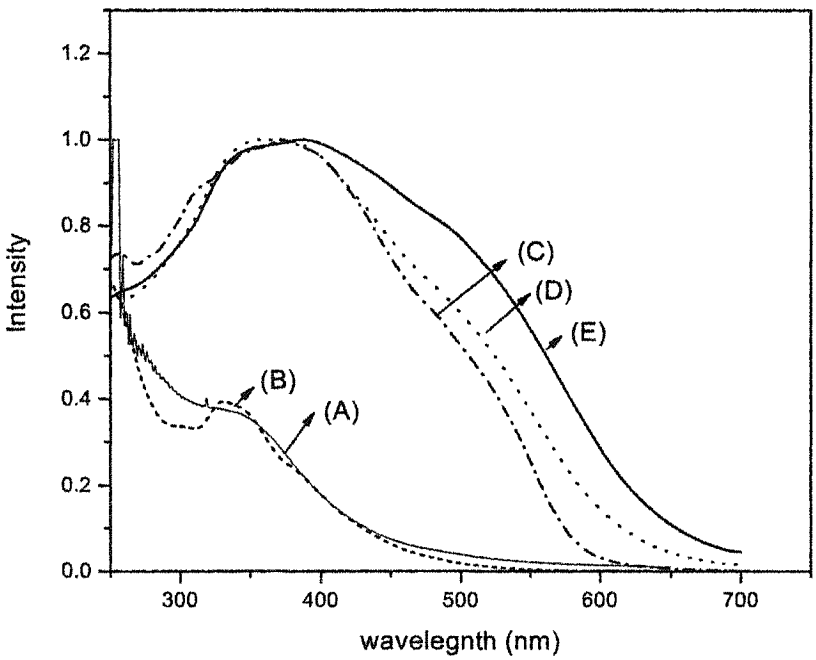

Fig. 5-5

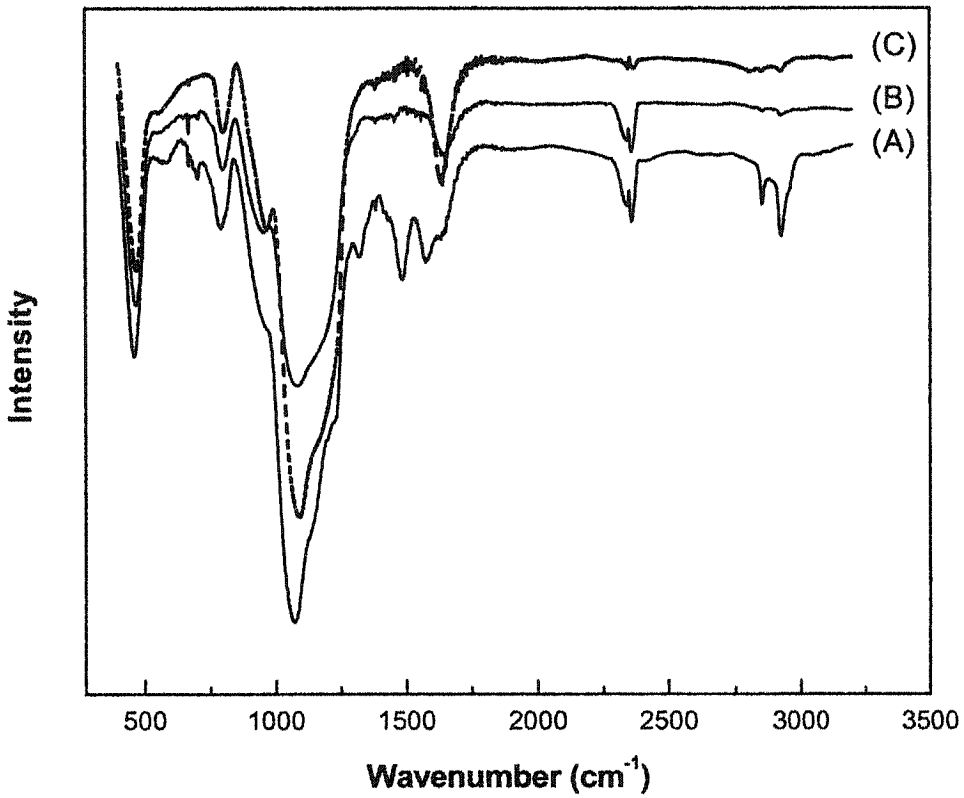

Fig. 5-6

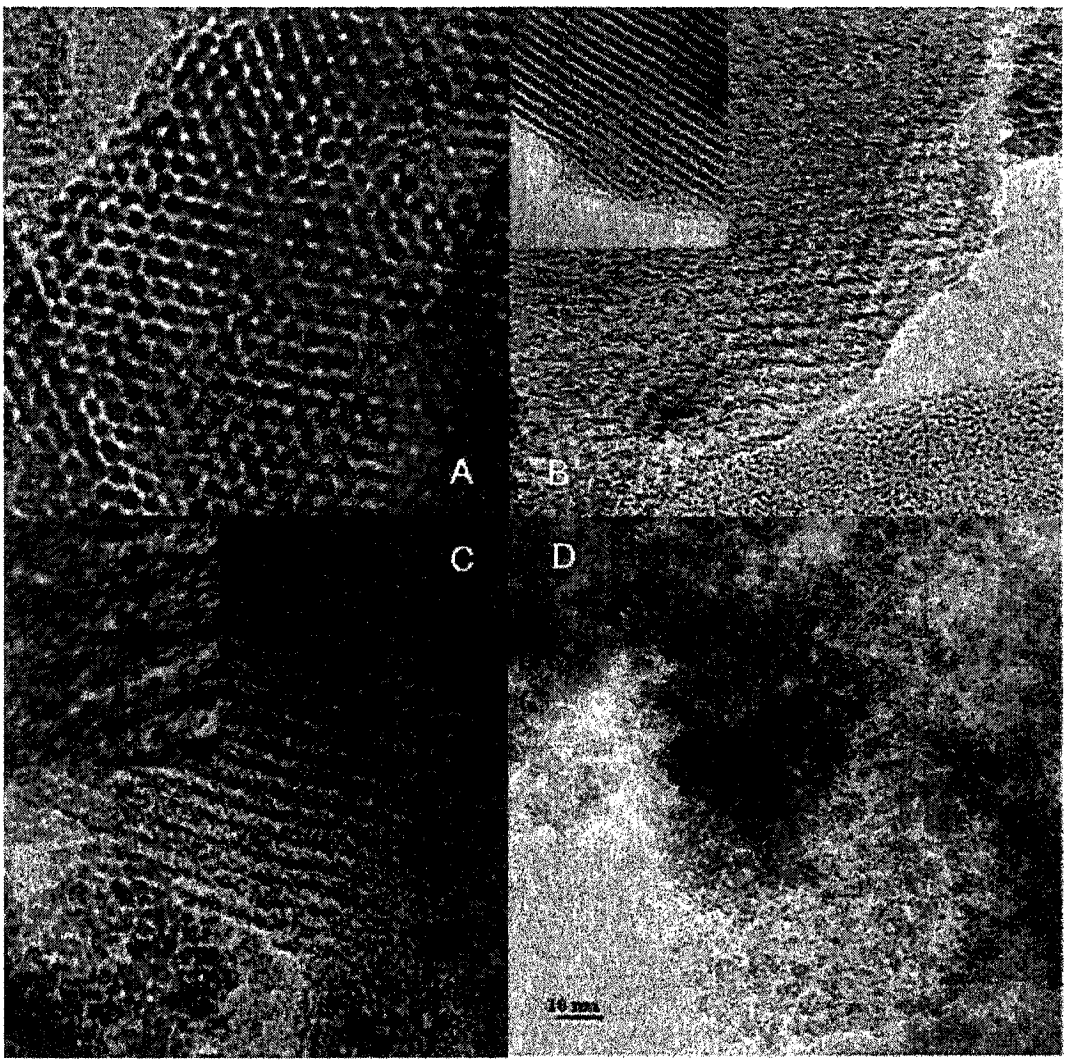

Fig. 5-7

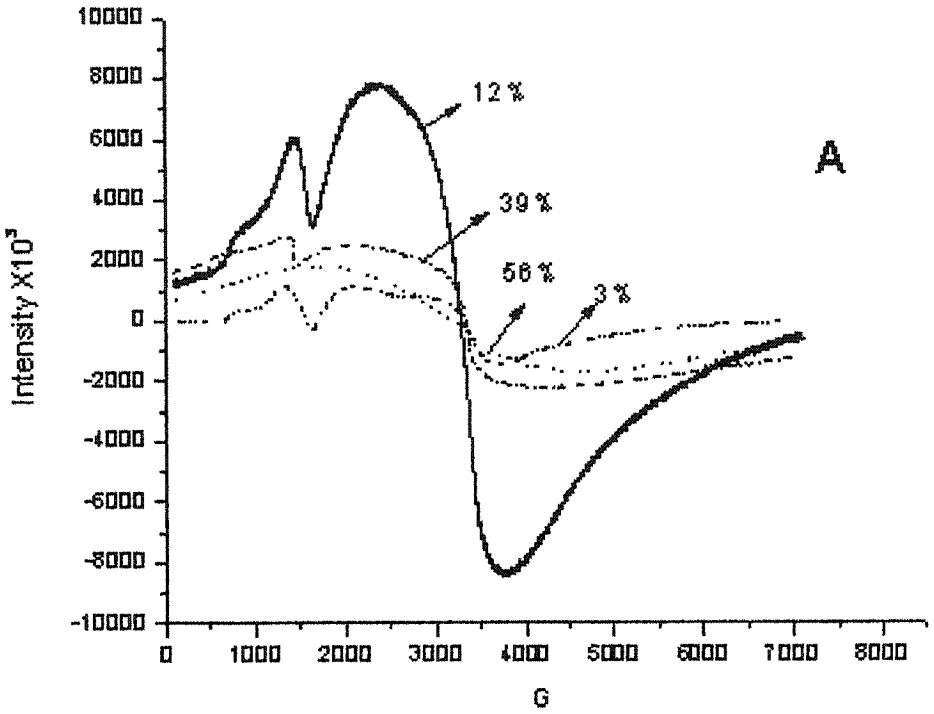

Fig. 5-8

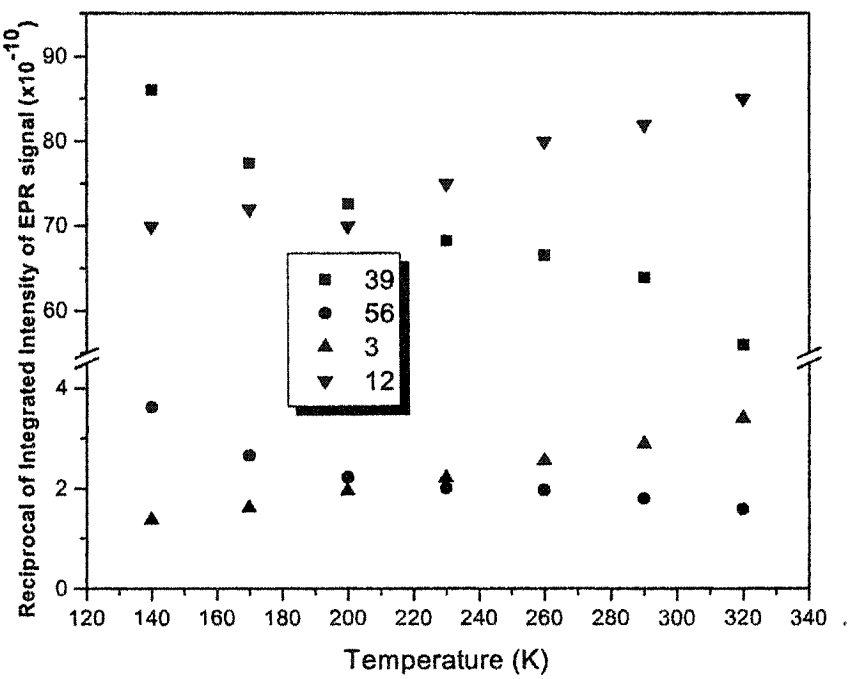

Fig. 5-9

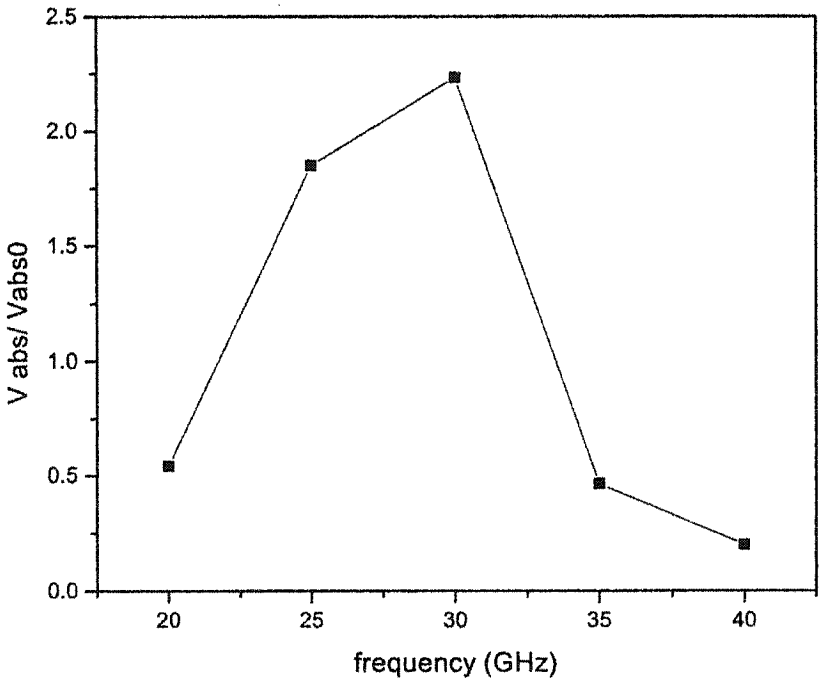

Fig. 5-10

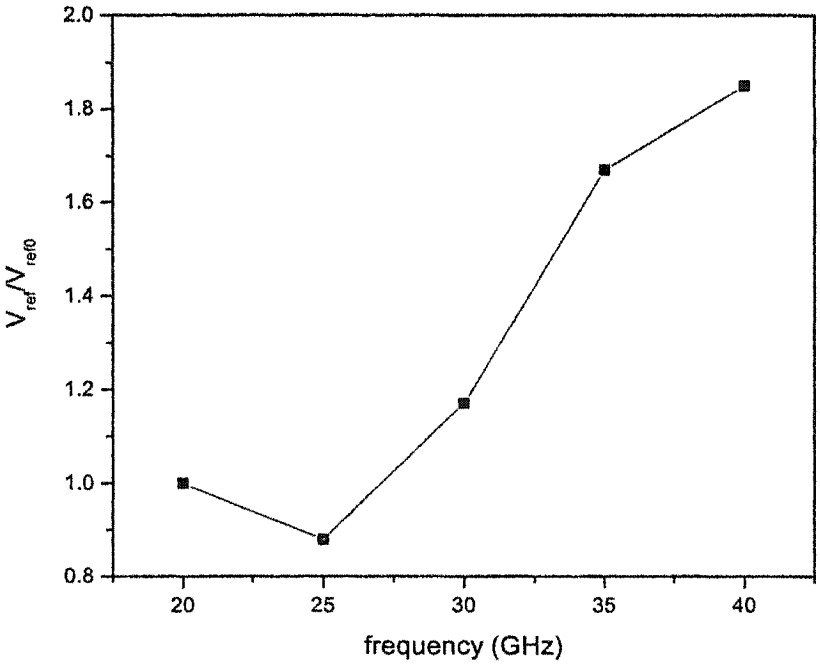

Fig. 5-11

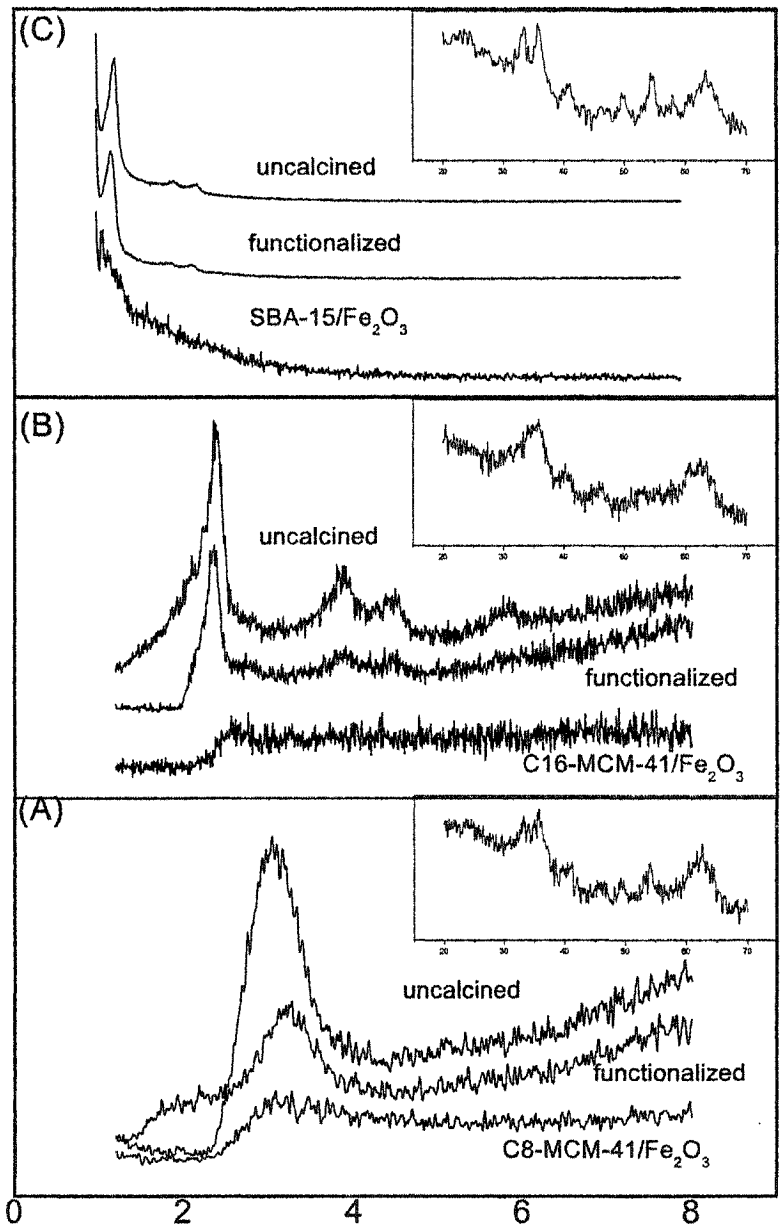

Fig. 5-12

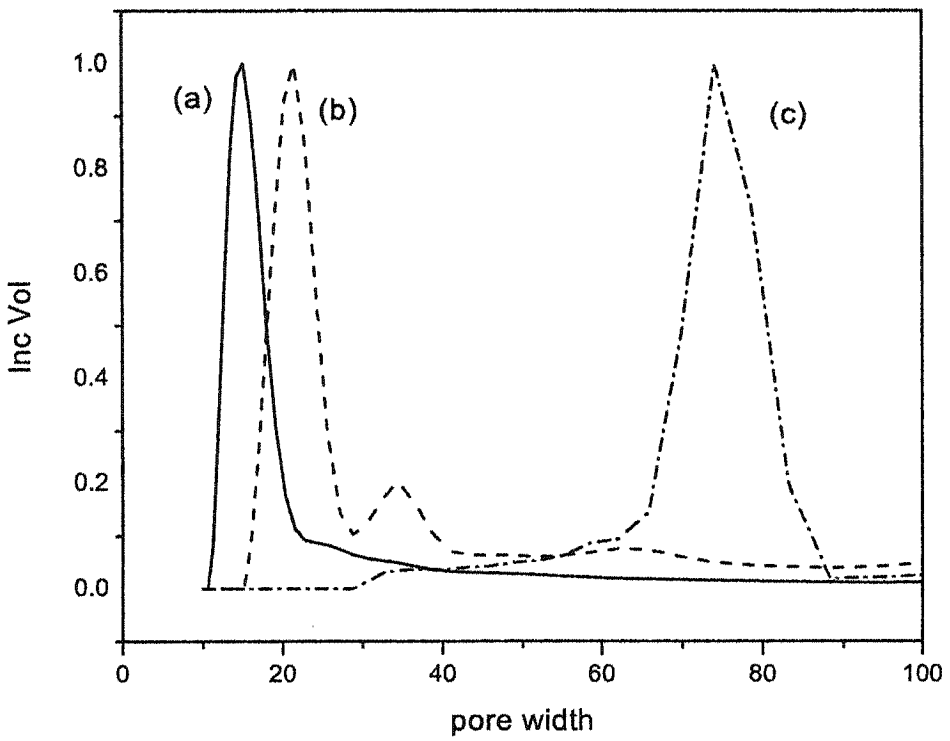

Fig. 5-13

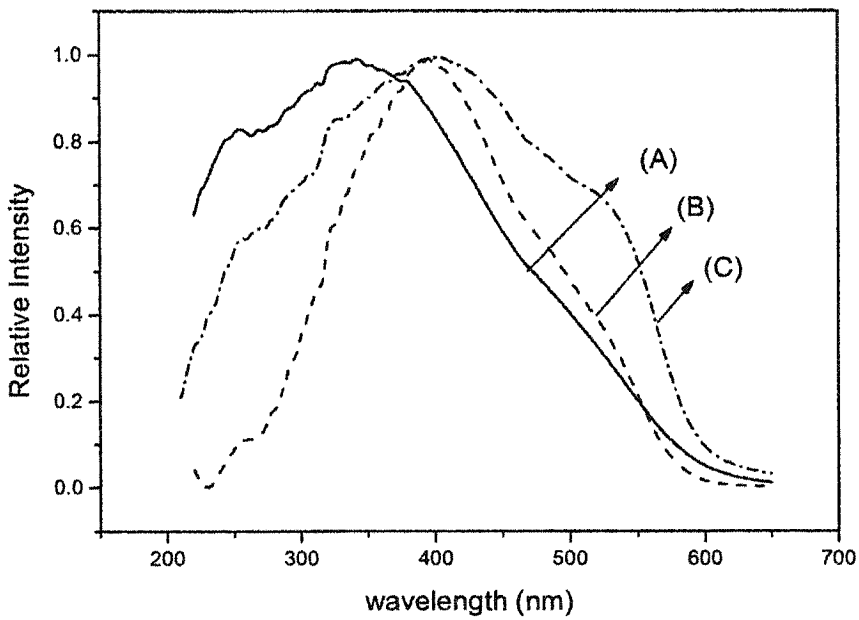

Fig. 5-14

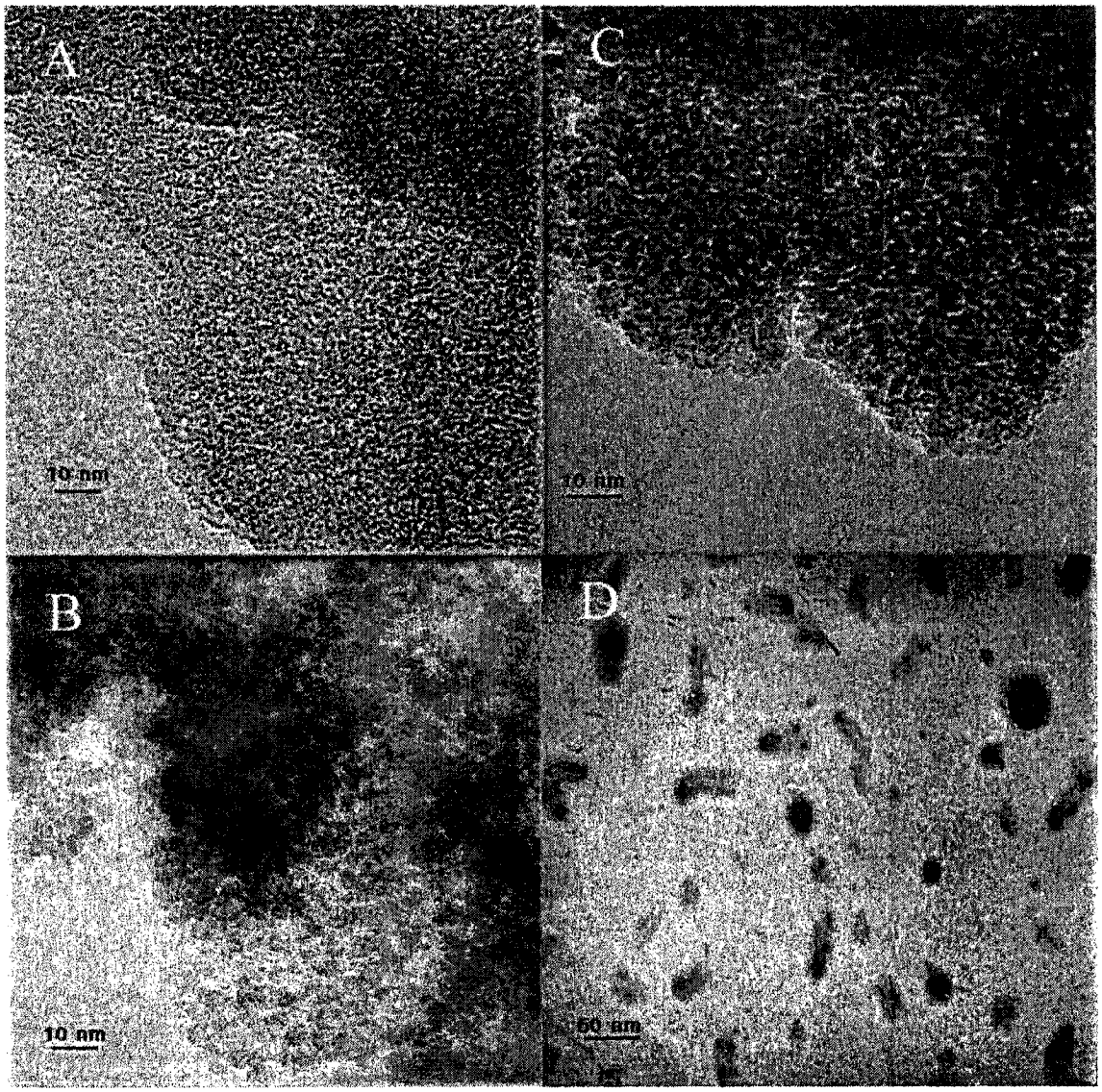

Fig. 5-15

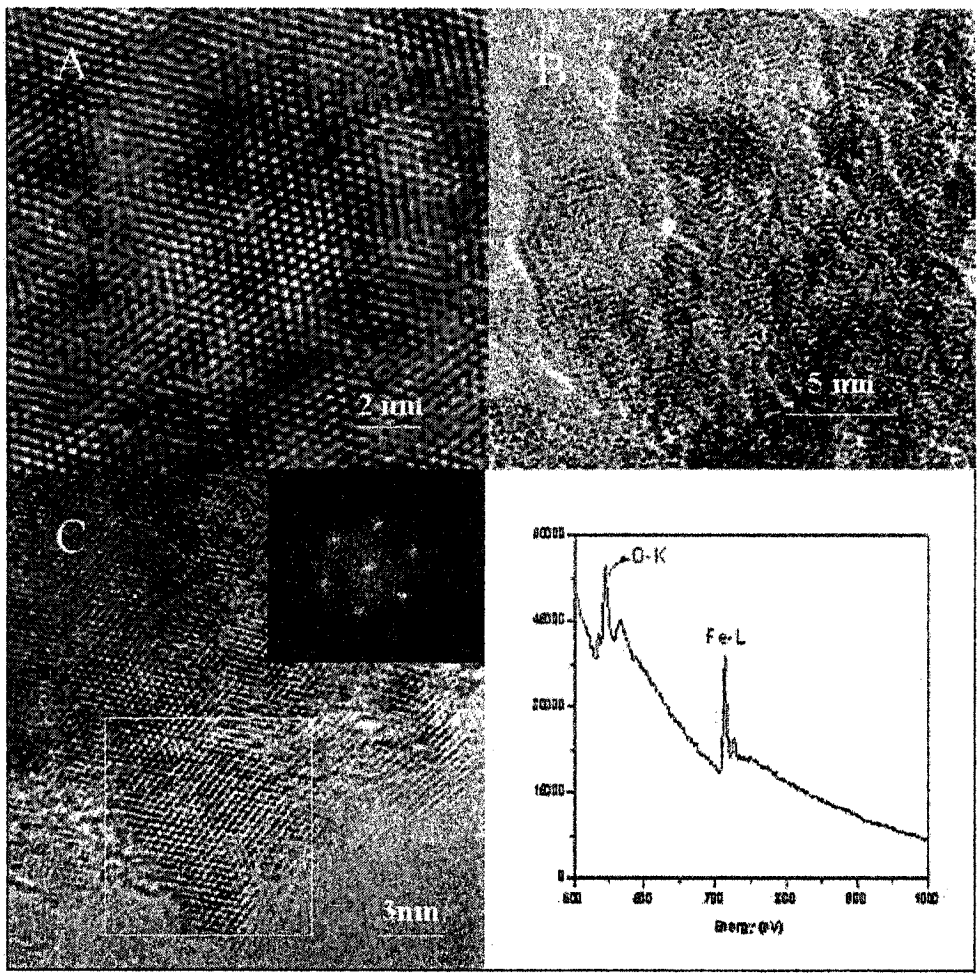

Fig. 5-16

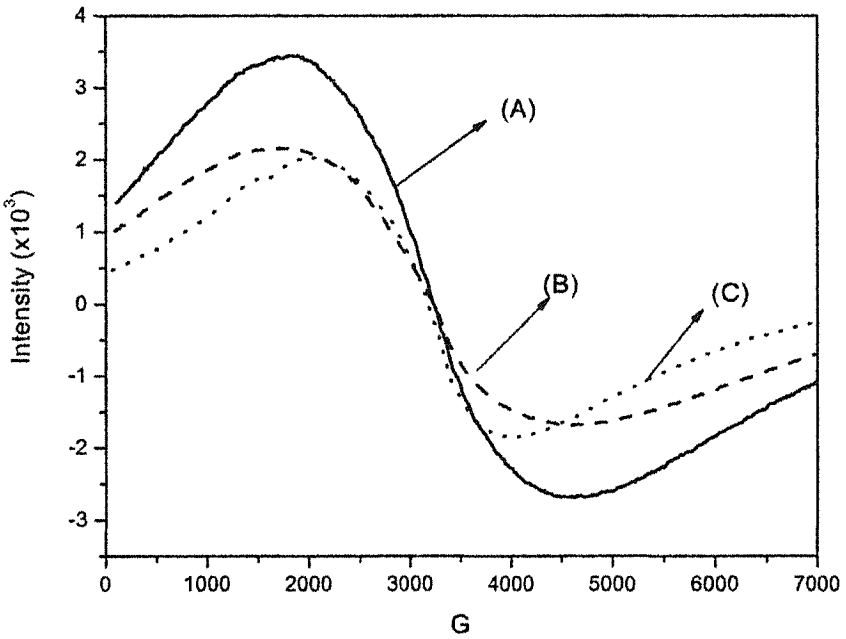

Fig. 5-17

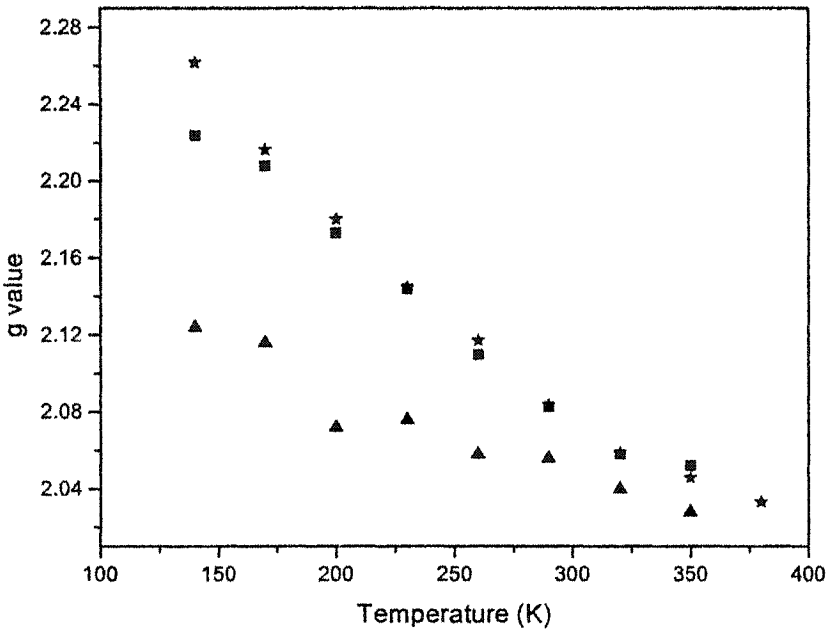

Fig. 5-18

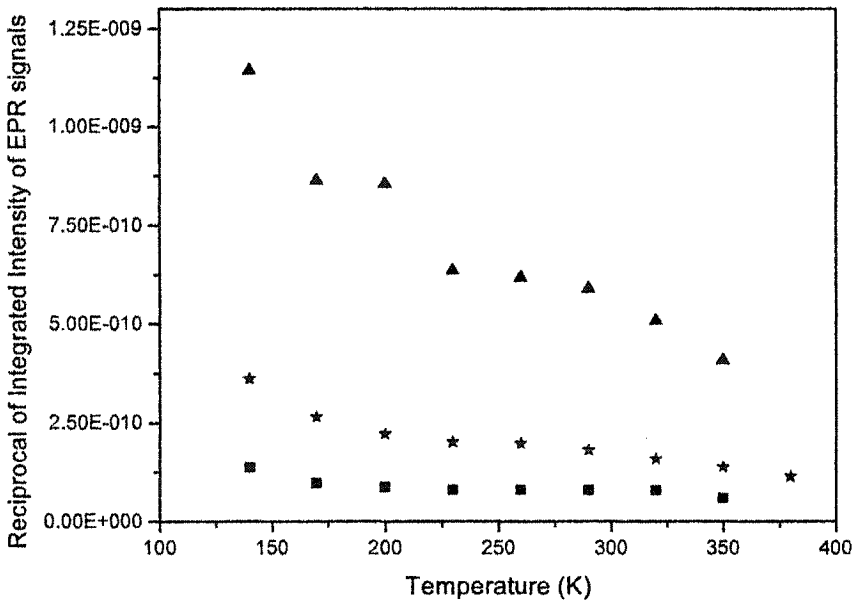

Fig. 5-19

Table 1 Relationship of *Q* factor* and Fe_2O_3 loading amount of sample /C16-MCM-41.

Weight (mg)	20	23.1	20	40
Loading amount	3%	12%	39%	56%
Q factor	3300	3250	3100	2500

Table 2 Relationship of *Q* factor* and weight of sample Fe_2O_3 /C16-MCM-41 with W_{Fe2O3} 39%

Weight (mg)	20	38	60	100
Q factor	3100	2750	2800	2500

**Q* factor was read at 0 G of magnetic field and under no microwave power

Table 3. Quality factor (Q) of microwave cavity with different sample inside

*P = 0.7 mW, MA = 10.5 G, f = 9.49 GHz, in 5 mm quartz tube, 99 G

	Blank tube	C8-MCM-41/Fe_2O_3 0.09(g)	C16-MCM-41/Fe_2O_3 (0.08g)	SBA-15/Fe_2O_3 (0.08g)
Q	3500	1800	2800	3000

Chapter 6: Summary

The investigation of host-guest systems using ordered mesoporous materials as host that is presented in this dissertation gives an indication of the prospects for conducting chemistry in nanodimensioned structures. The mesoporous materials described in above chapters consist of zeolite-Y containing mesoporous pores, aluminosilicate MCM-41, silicate MCM-41 with different pore opening sizes and SBA-15. The mesoporous hosts have been modified by two methods for the purpose of rigidifying the synthesized MCM-41 or SBA-15 and allowing the inclusion of the guest dye molecules or Fe_2O_3 nanoparticles. One method is a one step functionalization by covalently anchoring functional groups APTES to the channel wall and adjusting the pH value to a certain level. The other method is a two step functionalization processes involving passivation of the external surface by $C_6H_5Si(OCH_3)_3$ while the surfactant template filled in the channels then the removal the surfactant washed by methanol and modification the internal wall of the mesoporous materials by 3-(2-aminoethylamino) propyltrimethoxy-silane.

In chapters 2 and 3, the combination of XRD, UV-vis absorption and fluorescence measurements of the dyes TSPP and TTBC in solution and post-formation addition to an aluminosilicate MCM-41 indicates that we are able to form both monomeric and aggregated dyes occluded in the core. The composites consisting of J-aggregated TSPP or TTBC and the modified MCM-41 represent new nanomaterials that have new properties arise from exciton energies and dynamics that result from quantum confinement. The quantum confinement is associated with both the restricted growth region available to the spontaneously

self-assembled molecular aggregate, which forms when dyes (TSPP or TTBC) are exposed to a sufficiently basic microenvironment, and the intrinsic confinement of the exciton's movement among a subset of coherently responding molecules within the physical aggregate.

In chapter 4, we found out that DCM can be successfully occluded within the pores of MCM-41 and Y-zeolite. From UV-Vis absorption and fluorescence measurements, DCM is found to exhibit different photophysics for MCM-41 and Y-zeolite mesoporous materials. For the composite consisting of DCM and MCM-41, ICT processes are found to be sufficiently reduced so that a dual emission (attributed to emissions from the LE and ICT states) is observed. In this case, the optical decay leads to the assignment of lifetimes of 0.6 ± 0.1 ns for the LE state and 1.9 ± 0.1 ns for the TICT state. In the case of the Y-zeolite composite, only one emission (of decay lifetime 1.3 ± 0.1 ns) is found, which is rationalized in terms of the dimension of the supercages and the high polarity of the materials surface.

In chapter 5, it was found that Fe_2O_3 could be successfully incorporated within the pores of the mesoporous materials C8-MCM-41, C16-MCM-41 and SBA-15, each having a one-dimensional structure, with size increasing in the order presented. Composite samples were characterized by UV-vis, IR, TEM, EPR and X-ray diffraction. We ascertained that the loading level and the pore sizes of the three mesoporous materials significantly affect the spectral properties of encapsulated ferric oxide. From UV-vis absorption, ferric oxide is found to exhibit different blue-shifts relative to that for bulk ferric oxide; the lower level of the Fe_2O_3 and the

smaller the pore size, the larger the blue shift observed. Most profoundly, EPR measurements indicate that for sufficient loading with Fe_2O_3, the composite material exhibits nonzero absorption at zero applied magnetic fields and has a substantial microwave absorption capability at moderate applied fields. The absorption ability, in fact, is found to increase decrease in pore size of the mesoporous material in which the Fe_2O_3 is formed.

Bibliography

Bibliography of Chapter 1

1. Cundy, C. S.; Cox, P. A. *Chem. Rev.; (Review)* **2003,** *103*; 663.
2. Kaduk, J. A.; Faber, J. *The Rigaku Journal* **1995**, *12*, 14.
3. Crorma, A. *Chem. Rev.* **1997,** *97*, 2373.
4. Selvam, P.; Bhatia, S. K.; Sonwane, C. G. *Ind. Eng. Chem. Res.* **2001**, *40*, 3237.
5. Scott, B. J.; Wirnsberger, G.; Stucky, G. D. *Chem. Mater.* **2001**, *13*, 3140.
6. Zhao, X. S.; Lu, G. Q.; Millar, G. J. *Ind. Eng. Chem. Res.* **1996**, *35*, 2075.
7. Moller, K.; Bein, T. *Chem. Mater.* **1998**, *10*, 2950.
8. Zhang, W. H.; Lu, J. Q.; Han, B.; Li, M. J.; Xiu, J. H.; Ying, P. L.; Li, C. *Chem. Mater.* **2002**, *14*, 3413.
9. Zhao, D.; Feng, J.; Huo, Q.; Melosh, N.; Fredrichson, G. H.; Chmelka, B. F.; Stucky, G. D. *Science* **1998**, *279*, 548.

Bibliography of Chapter 2

1. Mishra, A.; Behera, R. K.; Behera, P. K.; Mishra B. K.; Behera G. B. *Chem. Rev.* **2000**, *100*, 1973.
2. Akins, D. L. *J. Phys. Chem.* **1986**, *90*, 1530.
3. Koti, A. S. R.; Taneja, J.; Periasamy, N. *Chem. Phys. Lett.* **2003**, *375*, 171.
4. Okamura, M. Y.; Feher, G.; Nelson, N. In *Photosynthesis*; Govindjee, Ed.; Academic Press: New York, **1982**; pp 195-272.

5. Pearlstein, R. M. In *Photosynthesis*; Amesz, J., Ed.; Elsevier: Amsterdam, **1987**; pp 299-317.

6. O'Neil, M. P.; Niemcyzk, M. P.; Svec, W. A.; Gosztola, D.; Gaines, G. L., III; Wasielewski, M. R. *Science* **1992**, *257*, 63.

7. Wagner, R. W.; Lindsey, J. S.; Seth, J.; Palaniappan, V.; Bocian, D. F. *J. Am. Chem. Soc.* **1996**, *118*, 3996.

8. Akins, D. L.; Zhu, H.-R.; Guo, C. *J. Phys. Chem.* **1994**, *98*, 3612.

9. Akins, D. L.; Zhu, H.-R.; Guo, C. *J. Phys. Chem.* **1996**, *100*, 5420.

10. Akins, D. L. In *J-Aggregate*; Kobayashi, T., Ed.; World Scientific: Singapore, **1996**; pp 67-94.

11. Guo, C.; Ren, B.; Akins, D. L. *J. Phys. Chem. B* **1998**, *102*, 8751.

12. Guo, C.; Ren, B.; Akins, D. L. *J. Phys. Chem.* In revision.

13. Grad, J.; Hernandez, G.; Mukamel, S. *Phys. Rev. A* **1988**, *37*, 3835.

14. Spano, F. C.; Mukamel, S. *J. Chem. Phys.* **1989**, *91*, 683.

15. Spano, F. C.; Kuklinski, J. R.; Mukamel, S. *J. Chem. Phys.* **1991**, *94*, 7534.

16. Kresge, C. T.; Leonowicz, M. E.; Roth, W. J.; Vartuli, J. C.; Beck, J. S. *Nature* **1992**, *359*, 710.

17. Beck, J. S.; Vartuli, J. C.; Roth, W. J.; Leonowicz, M. E.; Kresge, C. T.; Schmitt, K. D.; Chu, C. T.-W.; Olsen, D. H.; Sheppard, E. W.; McCullen, B.; Higgins, J. B.; Schlenker, J. L. *J. Am. Chem. Soc.* **1992**, *114*, 10834.

18. Liu, C.-J.; Li, S.-G.; Pang, W.-Q.; Che, C.-M. *Chem. Commun.* **1997**, *65*, 78.

19. Mercier, L.; Pinnavaia, T. J. *Adv. Mater.* **1997**, *9*, 500.

20. (a) Feng, X.; Fryxell, G. E.; Wang, L. Q.; Kim, A. Y.; Liu, J.; Kemner, K. M. *Science* **1997**, *276,* 923. (b) Liu, J.; Feng, X.; Fryxell, G. E.; Wang, L. Q.; Kim, A. Y.; Gong, M. *Adv. Mater.* **1998**, *10*, 161.

21. (a) Cauvel, A.; Renard, G.; Brunel, D. *J. Org. Chem.* **1997**, *62,* 749. (b) Brunel, D.; Cauvel, A.; Fajula, F.; DiRenzo, F. *Stud. Surf. Sci. Catal.* **1995**, *97,* 173.

22. Sutra, P.; Brunel, D. *Chem. Commun.* **1996,** 2485.

23. Bellocq, N.; Brunel, D.; Lasperas, M.; Moreau, P. *Stud. Surf. Sci. Catal.* **1997**, *108*, 485.

24. Subba Rao, Y. V.; De Vos, D. E.; Bein, T.; Jacobs, P. A. *Chem. Commun.* **1997**, 355. (b) Subba Rao, Y. V.; De Vos, D. E.; Jacobs, P. A. *Angew. Chem., Int. Ed. Engl.* **1997**, *36*, 2661.

25. Diaz, J. F.; Balkus, K. J., Jr.; Bedioui, F.; Kurshev, V.; Kevan, L. *Chem. Mater.* **1997**, *9,* 61.

26. Sung-Suh, Hyung Mi; Luan, Z.; Kevan, L. *J. Phys. Chem. B* **1997**, *101*, 10455.

27. Stucky, G. D.; Monnier, A.; Schuth, F.; Huo, Q.; Margolese, D.; Kumar, D.; Kridhnamurty, M.; Petroff, P.; Firouzi, A.; Janicke, M.; Chmelka, B. F. *Mol. Cryst. Liq. Cryst.* **1994**, *240*, 187.

28. Sindorf, D. W.; Macier, G. E. *J Am. Chem.Soc.* **1983**, *105*, 3769.

29. Subba Rao, Y. V.; De Vos, D. E.; Jacobs, P. A. *Angew. Chem., Int. Ed. Engl.* **1997**, *36*, 2661.

30. Feng, X.; Fryxell, G. E.; Wang, L. Q.; Kim, A. Y.; Liu, J.; Kemner, K. M. *Science* **1997**, *276*, 923.

31. Akins, D. L.; Özcelik, S.; Zhu, H.-R.; Guo, C. *J. Phys. Chem.* **1996**, *100*, 14396.

32. Ohno, O.; Kaizu, Y.; Kobayashi, H. *J. Chem. Phys.* **1993**, *99*, 4128.

33. Akins, D. L. *J. Phys. Chem.* **1986**, *90*, 1530.

34. Akins, D. L.; Akpabli, C. K.; Li, X. *J. Phys. Chem.* **1989**, *93*, 1977.

35. Kasha, M. *Radiat. Res.* **1963**, *20*, 55.

36. Kubelka, P. *J. Opt. Soc. Am.* **1948**, *38*, 448.

Bibliography of Chapter 3

1. Akins, D. L.; Özcelik, S.; Zhu, H.-R.; Guo, C. *J. Phys. Chem. A* **1997**, *101*, 3251.

2. Özcelik, S.; Akins, D. L. *J. Phys. Chem. B* **1999**, *103*, 8926.

3. Akins, D. L. *J. Phys. Chem.* **1986**, *90*, 1530.

4. Akins, D. L. *J. Colloid Interface Sci.* **1982**, *90*, 373.

5. Li, X.; Gu, B.; Akins, D. L. *Chem. Phys. Lett.* **1984**, *105*, 263.

6. Gu, B.; Akins, D. L. *Chem. Phys. Lett.* **1985**, *113*, 558.

7. Akins, D. L.; Akpabli, C.; Li, X. *J. Phys. Chem.* **1989**, *93*, 1977.

8. Akins, D. L.; Macklin, J. W. *J. Phys. Chem.* **1989**, *93*, 5999.

9. Akins, D. L.; Macklin, J. W.; Parker, L.; Zhu, H.-R. *Chem. Phys. Lett.* **1990**, *169*, 564.

10. Akins, D. L.; Macklin, J. W.; Zhu, H.-R. *J. Phys. Chem.* **1990**, *95*, 793.

11. Akins, D. L.; Zhu, H.-R. *Langmuir* **1992**, *8*, 546.

12. Akins, D. L.; Macklin, J. W.; Zhu, H.-R. *J. Phys. Chem.* **1992**, *96*, 4515.

13. Akins, D. L.; Zhuang, Y. H.; Zhu, H.-R.; Li, J. Q. *J. Phys. Chem.* **1993**, *98*, 1068.

14. Akins, D. L. In *J-Aggregate*; Kobayashi, T., Ed.; World Scientific: Singapore, **1996**; pp 67-94.

15. Plyuto, Y.; Berquier, J.; Jacquiod, C.; Ricolleau, C. *Chem. Commun.* **1999**, 1653.

16. Wu, C.; Bein, T. *Science* **1994**, *264*, 1757.

17. Kageyama, K.; J. Tamazawa, J.; Aida, T. *Science* **1999**, *285*, 2113.

18. Moller, K.; Bein, T. *Chem. Mater.* **1998**, *10*, 2950.

19. Holland, B. T.; Walkup, C.; Stein, A. *J. Phys. Chem. B* **1998**, *102*, 4301.

20. Sung-Suh, H,; Luan, Z.; Kevan, L. *J. Phys. Chem. B* **1997**, *101*, 10455.

21. Stucky, G. D.; MacDougall, J. E. *Science* **1990**, *247*, 669.

22. Moller, K.; Bein, T. *Chem. Mater.* **1998**, *10*, 2950.

23. Feng, X.; Fryxell, G. E.; Wang, L. Q.; Kim, A. Y.; Liu, J.; Kemner, K. M. *Science* **1997**, *276*, 923.

24. Chakraborty, P. *J. Mater. Sci.* **1998**, *33*, 2235.

25. Yang, P.; Wirnsberger, G.; Huang, H. C.; Cordero, S. R.; McGehee, M. D.; Scott, B.; Deng, T.; Whitesides, G. M.; Chmelka, B. F.; Buratto, S. K.; Stucky, G. D. *Science* **2000**, *287*, 465.

26. Özcelik, S.; Akins, D. L. *Appl. Phys. Lett.* **1997**, *71*, 1.

27. Özcelik, S.; Akins, D. L. *Appl. Phys. Lett.* **1998**, *73*, 1949.

28. Xu, W.; Guo, H.; Akins, D. L. *J. Phys. Chem. B*, **2001**, *105*, 1543.

29. Kresge, C. T.; Leonowicz, M. E.; Roth, W. J.; Vartuli, J. C.; Beck, J. S. *Nature* **1992**, *359*, 710.

30. Beck, J. S.; Vartuli, J. C.; Roth, W. J.; Leonowicz, M. E.; Kresge, C. T.; Schmitt, K. D.; Chu, C. T.-W.; Olson, D. H.; Sheppard, E. W.; McCullen, B.; Higgins, J. B.; Schlenker, J. L. *J. Am. Chem. Soc.* **1992**, *114*, 10 834.

31. Liu, C.-J.; Li, S.-G.; Pang, W.-Q.; Che, C.-M. *Chem. Commun.*, **1997**, *65*, 78.

32. Mercier, L.; Pinnavaia, T. J. *Adv. Mater.* **1997**, *9*, 500.

33. Stucky, G. D.; Monnier, A.; Schuth, F.; Huo, Q.; Margolese, D.; Kumar, D.; Kridhnamurty, M.; Petroff, P.; Firouzi, A.; Janicke, M.; Chmelka, B. F. *Mol. Cryst. Liq. Cryst.* **1994**, *240*, 187.

34. Akins, D. L.; Zhu, H.-R.; Guo, C. *J. Phys. Chem.* **1996**, *100*, 5420.

35. Grad, J.; Hernandez, G.; Mukamel, S. *Phys. Rev. A* **1988**, *37*, 3835.

36. Spano, F. C.; Mukamel, S. *J. Chem. Phys.* **1989**, *91*, 683.

37. Spano, F. C.; Kuklinski, J. R.; Mukamel, S. *J. Chem. Phys.* **1991**, *94*, 7534.

38. Kubelka, P. *J. Opt. Soc. Am.* **1948**, *38*, 448.

Bibliography of Chapter 4

1 Verhoeven, J. W. *Pure Appl. Chem.* **1990**, *63*, 1585.

2 Khundkar, L. R.; Stiegman, A. E.; Perry, J. W. *J. Phys. Chem.* **1990**, *94*, 1224.

3 Lueck, H.; Windsor, M.; Rettig, W. *J. Phys. Chem.* **1990**, *94*, 4550.

4 Launay, J. P.; Sowinska, M.; Leydier, L.; Gourdon, A.; Amouyal, E.; Boillot, M. L.; Heisel F.; Miehé, J. A. *Chem. Phys. Lett.* **1989**, *160*, 89.

5 Spange, S.; Zimmermann, Y.; Graeser, A. *Chem. Mater.* **1999**, *11*, 3245.1.

6 Yoshizawa, M.; Kubo, M.; Kurosawa, M. *J. Lumin.* **2000**, *87-89*, 739.

7 Bingermann, D.; Ernsting, N. P. *J. Chem. Phys.* **1995**, *102*, 2691.

8 Moulik, S. P.; Pal, B. K. *Adv. Coll. Int. Sci.* **1998**, *78*, 99.

9 Easter, D. C.; Baronavski, A. P. *Chem. Phys. Lett.* **1993**, *201*, 153.

10 Van der Meulen, P.; Zhang, H.; Jonkman A. M.; Glasbeek, M. *J. Phys. Chem.* **1996**, *100*,5367.

11 Gustavsson, T.; Baldacchino, G.; Mialocq J. -C.; Pommeret, S. *Chem. Phys. Lett.* **1995**, *236*, 587.

12 Maciejewski, A.; Naskrecki, R.; Lorenc, M.; Ziolek, M.; Karolczak, J.; Kubicki, J.; Matysiak, M.; Szymanski, M. *J. Mol. Struct.* **2000**,*555*,1.

13 Pal, S. K.; Sukul, D.; Mandal, D.; Bhattacharyya, K. *J. Phys. Chem. B* **2000**, *104*, 4529.

14 Pal, S. K.; Sukul, D.; Mandal, D.; Sen, S.; Bhattacharyya, K. *Chem. Phys. Lett.* **2000**, *327*, 91.

15 Pal, S. K.; Mandal, D.; Sukul, D.; Sen, S.; Bhattacharyya, K. *J. Phys. Chem. B* **2001**, *105*, 1438.

16 Pal, S. K.; Sukul, D.; Mandal, D.; Sen, S.; Bhattacharyya, K. *Tetrahedron* **2000**, *56*, 6999.

17 Pal, S. K.; Mandal, D.; Sukul, D.; Bhattacharyya, K. *Chem. Phys. Lett.* **1999**, *312*, 178.

18 Martin, M. M.; Plaza, P.; Meyer, Y. H. *Chem. Phys.* **1995**, *192*, 367.

19 Zhou, Y.; Liu, Y.; Zhao, X.; Jiang, M. *J. Mol. Struct.* **2001**, *545*, 61.

20 Mandal, D.; Sen, S.; Bhattacharyya K.; Tahara, T. *Chem. Phys. Lett.* **2002** *359*, 77.

21 Wu, D.; Wang, L.; Liu, Y.; Ning, Y.; Zhao, J.; Liu, X.; Wu, S.; He, X.; Lin, J.; Wang, L.; Ma, D.; Wang, D.; Jing, X.; Wang, F. *Synth. Metals.* **2000**, *111-112*, 563.

22 Liu, C. J.; Li, S. G.; Pang, W. Q.; Che, C. M. *Chem. Commun.* **1997**, *65*, 78.

23 Galletero, M. S.; García, H.; Bourdelande, J. L. *Chem. Phys. Lett.* **2003**, *370*, 829.

24 Fayed, T. A.; Organero, J. A; Garcia-Ochoa, I.; Tormo, L.; Douhal, A. *Chem. Phys. Lett.* **2002**, *364*, 108.

25 (a) Xu, W.; Guo, H.; Akins, D. L. *J. Phys. Chem. B* **2001**, *105*, 1543; (b) Xu, W.; Guo, H.; Akins, D. L. *J. Phys. Chem. B* **2001**, *105*, 7686.

26 Wery, E. In *Effects of Molecular Environment on flourescence and Phosphorescence*; Marcel Dekker, Ed.; New York, **1990**.

27 Sarkar, N.; Das, K.; Nararyan Nath, D.; Bhattacharyya, K. *Langmuir* **1994** *10*, 326.

28 Datta, A.; Mandal D.; Kumar Pal, S.; Bhattacharyya, K. *J. Phys. Chem. B.* **1997**, *101*, 10221.

29 Kim, Y.; Lee, B. I.; Yoon, M. *Chem. Phys. Lett.* **1998**, *286*, 466.

30 Gu, G.; Ong P. P.; Li, Q. *J. Phys. D: Appl. Phys.* **1999**, *32*, 2287.

31 Márquez, F.; Garcia, H.; Palomares, E.; Fernández, L.; Corma, A *J. Am. Chem. Soc.* **2000**, *122*, 6520.

34 Yang, J.; He, Q.; Lin, H.; Fan, J.; Bai, F. *Macromol. Rapid Commun.* **2001**, *22*, 1152.

35 Kubelka, P. *J. Opt. Soc. Am.* **1948**, *38*, 448.

Bibliography of Chapter 5

1 Petrov, V. M.; Gagulin, V. V. *Inorganic Materials* **2001** *37*, 135.

2 Standley, K. J. In *Oxide Magnetic Materials*, Oxford, Clarendon Press, **1972**.

3 Boca Raton, Fla., In *EPR and Advanced EPR Studies of Biological Systems*; Dalton, L. R., Ed.; CRC- Press, **1985**.

4 Panissod P.; Drillon A. In *Magnetism: Molecules to Materials IV*; Miller, J. S., Drillon, M., Ed.; Wiley-VCH, **2002**.

5 Moreno, E. M.; Zayat, M.; Morales, M. P.; Serna, C. J.; Roig, A.; Levy, D. *Langmuir* **2002**, *18*, 4972.

6 Tannenbaum, R.; Reich, S.; Flenniken, C. L.; Goldberg, E. P. *Adv. Mater.* **2002**, *14*, 1402.

7 Huo, L.; Li, W.; Lu, L.; Cui, H.; Xi, S.; Wang, J.; Zhao, B.; Shen, Y.; Lu, Z. *Chem. Mater.* **2000**, *12*, 790.

8 Bourlinos, A.; Simopoulos, A.; Petridis, D.; Okumura, H.; Hadjipanayis, G. *Adv. Mater.* **2001**, *13*, 289.

9 Weckhuysen, B. M.; Wang, D.; Rosynek, M. P.; Lunsford, J. H. *Angew. Chem. Int. Ed. Engl.* **1997**, *36*, 2374.

10 Iwamoto, M.; Abe, T.; Tachibana, Y. *J. Mol. Cata A: Chemical.* **2000**, *155*, 143.

11 Pascal, C.; Pascal, J. L.; Favier, F.; Elidrissi Moubtassim, M. L.; Payen, C. *Chem. Mater.* **1999**, *11*, 141.

12 Xu, W.; Liao, Y.; Akins, D. L. *J. Phys. Chem. B* **2002**, *106*, 11127.

13 Tian, B.; Liu, X.; Yang, H.; Xie, S.; Yu, C.; Tu, B.; Zhao, D. *Adv. Mater.* **2003**, *15*, 1370.

14 Shi, J.-l.; Hua, Z.-l.; Zhang, L.-x. *J. Mater. Chem.* **2004**, *14*, 795.

15 MacLachlan, M. J.; Aroca, P.; Coombs, N.; Manners, I.; Ozin, G. A. *Adv. Mater.* **1998**, *10*, 144.

16 Abe,T.; Tachibana,Y.; Uemastu, T.; Iwamoto, M. *Chem. Commun.* **1995**, 1617.

17 Zhang, L.; Papaefthymiou, G. C.; Ying, J. Y. *J. Phys. Chem. B* **2001**, *105*, 7414.

18 Guo, H.; Xu,W.; Cui, M.; Yang, N. –L.; Akins, D. L. *Chem. Commun.* **2003**, 1432.

21 Guo, H.; Cui. M.; Zhang, X.; Xu, W.; Sharma, R.; Yang, N.-L.; Akins, D. L. (submitted).

22 Guo, H.; Zhang, X.; Chi, N.; Xu, W.; Sharma, R.; Yang, N.-L.; Akins, D. L. (to be submitted).

21 Choma, J.; Burakiewicz-Mortka, W.; Jaroniec, M. *Colloid Surface A* **2002**, *203*, 97.

22 Sayari, A.; Danumah, C.; Moudrakovski, I. L. *Chem. Mater.* **1995**, *7*, 813; Sayari, A.; Moudrakovski, I. L.; Danumah, C.; Ratcliffe, C. I.; Ripmeester, J. A.; Preston, K. F. *J. Phys. Chem.* **1995**, *99*, 16373.

23 Zhao, D.; Feng, J.; Huo, Q.; Melosh, N.; Fredrickson, G. H.; Chmelka, B. F.; Stucky, G. D. *Science* **1998**, *279*, 548.

24 Zhang, Z.; Dai, S.; Fan, X.; Blom, D. A.; Pennycook, S. J.; Wei, Y. *J. Phys. Chem. B* **2001**, *105*, 6755.

25 Bourlinos, A. B.; Simopoulos, A.; Boukos, N.; Petridis, D. *J. Phys. Chem. B* **2001**, *105*, 7432.

26 Diaz, J. F.; Balkus, K. J., Jr.; Bedioui, F.; Kurshev, V.; Kevan, L. *Chem. Mater.* **1997**, *9*, 61.

27 Jiao, F.; Yue, B.; Zhu, K.; Zhao, D.; He, H. *Chem. Lett.* **2003**, *32*, 770

28 Cannas, C.; Gatteschi, D.; Musinu, A.; Piccaluga, G.; Sangregorio, C. *J. Phys. Chem. B* **1998**, *102*, 7721.

29 Testa, A. M.; Foglia, S.; Suber, L.; Fiorani, D.; Casas, L.; Roig, A.; Molins, E.; Greneche, J. M.; Tejada, J. *J Appl. Phys.* **2001**, *90*.

30 Barco, E. d.; Asenjo, J.; Zhang, X. X.; Pieczynski, R.; Julia, A.; Tejada, J.; Ziolo, R. F. *Chem. Mater.* **2001**, *13*, 1487.